Measurement of ϕ-meson photoproduction near production threshold with linearly polarized photons

Tsutomu Mibe

Measurement of ϕ-meson photoproduction near production threshold with linearly polarized photons

Tsutomu Mibe

A thesis submitted to the department of physics
in partial fulfillment of
the requirements for the degree of

Doctor of Philosophy in Physics

Osaka University

Research Center for Nuclear Physics
10-1 Mihogaoka, Ibaraki, Osaka, Japan

2004

The members of committee approved this thesis defended on February 3rd, 2004 :

Professor Takashi Nakano,	Research Center for Nuclear Physics, Osaka university
Professor Hiroshi Toki,	Research Center for Nuclear Physics, Osaka university
Professor Mamoru Fujiwara,	Research Center for Nuclear Physics, Osaka university
Professor Masaharu Nomachi,	Department of physics, Osaka university
Professor Tadafumi Kishimoto,	Department of physics, Osaka university

Abstract

We present a measurement of photoproduction of ϕ mesons on protons using linearly-polarized photons beam in the energy range from the production threshold to $E_\gamma = 2.4$ GeV. The experiment was performed at the SPring-8 LEPS facility. The differential cross section as a function of the beam energy has a local maximum around $E_\gamma = 2$ GeV which can not explained by using the Pomeron and pseudo scalar exchanges processes. The spin density matrix elements of ϕ photoproduction are extracted from the decay angular distribution of ϕ mesons at forward angles. It is found that the helicity conserving amplitudes are dominant. The angular correlation between the azimuthal angle of K^+ and the polarization vector of the photon showed that the contribution from natural-parity exchanges are greater than that from the unnatural-parity exchanges.

Acknowledgements

I have spent four years to complete this Ph.D project. During this period, I have received many helps and encouragements from a lot of people. Among them, my thesis adviser, Prof. Takashi Nakano played a special role. His advises and encouragements were always valuable. His enthusiastic supervisions made this work possible. I would like to gratefully acknowledge Prof. Mamoru Fujiwara who provided me many helps in writing up the thesis and taught me a style of scientific work, and he gave me opportunities to work at SPring-8 site as a JAERI student fellow. I would like to express my gratitude to Prof. H. Toki as one of the first person who discussed the physics potential of ϕ meson photoproduction. I would like to thank Prof. H. Ejiri and Prof. H. Kamitsubo for their great supports to construct the LEPS facility at SPring-8.

I thank Dr. T. Hotta who taught me a lot of experimental technique, especially in the development of the tagging counter and the silicon strip detector. He also gave me valuable advises in my analysis work. I thank Dr. Y. Sugaya for his assistance in preparation of the experiment and developing the online/offline software. I learned the basis of the experimental technique and handling of the experimental data from him. I appreciate Prof. Wen-Chen Chang who taught me a lot of technique for analyzing the present experimental data. As a co-worker of the data analysis with him, there is no doubt that this work would not be completed without outcomes from his helps and discussions with him. I thank Prof. A. I. Titov and A. Hosaka who greatly deepen my theoretical basis of this subject by his enthusiastic personal lectures.

I would like to acknowledge Dr. Y. Ohashi for his great helps of construction and maintenance of the beamline and detectors. I thank Dr. S. Date for his analysis and tuning of the electron beam which were very important to make an intense and stable photon beam. I would like to thank Prof. J-K. Ahn, Dr. N. Muramatsu, Dr. M. Sumihama, Mr. T. Ishikawa, Dr. D.S. Oshuev and Dr. R.G.T. Zegers for good collaboration in the analysis works to develop the standard offline analysis software and Monte Carlo simulator.

I thank Prof. H. Akimune, Dr. M. Yosoi, Dr. T. Yorita, Dr. Y. Asano, Dr. H. Kohri, Dr. N. Matsuoka, Prof. T. Iwata, Dr. A. Wakai, Prof. M. Nomachi, Prof. H. Shimizu Dr. K. Kino, Dr. S.C. Wang, Dr. K. Yonehara, Dr. H. Fujimura, Prof. H. Kawai, Prof. S.Makino, Dr. H. Toyokawa, Dr. N. Kumagai, Dr. H. Ookuma, Prof. K. Imai, Prof. H. Hicks, Prof. C. Rangacharyulu, Dr. P. Shagin, Prof. C.W. Wang, Dr. K. Hirota and Dr. S. Hasegawa who have made great contributions for constructing the LEPS facility. They collaborated in developing and operating the hardware and software of the laser system and the LEPS spectrometer. Their efforts made this work successful.

I would like to thank Mr. T. Matsumura, Mr. T. Ooba, Mr. Y. Shiino, Mr. M. Morita,

Mr. T. Sasaki, Mr. M. Miyabe, Mr. M. Niiyama, Mr. Z. Y. Kim, Ms. D. S. Ahn, Mr. T. Miwa, Mr. Y. Toi and Mr. A. Shimizu for fruitful discussions. It was my great experience to work with students from many institutes.

I have stayed for three years in Advanced Science Research Center (ASRC) of JAERI. I thank Dr. M. Date and Dr. H. Yasuoka of ASRC for their encouragement of this work. I appreciate great hospitality of director Dr. O. Shimomura and JAERI staff. I thank many supports from JAERI researchers.

I appreciate intensive encouragements and continuous supports from my family, Yoshiharu Mibe, Tomiko Mibe, Ryota Mibe and Rika Mibe during my long course of studies and researches in RCNP.

Finally, I would like to thank my thesis committee members who spend a lot of time for reviewing my thesis.

Contents

Chapter 1

Physics Motivation

In this chapter, the photoproduction of $\phi(1020)$ meson is discussed on the basis of the previous theoretical and experimental backgrounds. The vector meson photoproduction and its relation to the Regge phenomenology are explained. New physics to be studied via the ϕ photoproduction near threshold is discussed. The importance of measurement of polarization observables is explained.

1.1 Introduction

Photoproduction of vector meson has an aspect similar to hadron-hadron collision [1]. The total photoproduction cross section of vector meson photoproduction increases slowly with increasing the photon energy. The energy dependence of the cross sections of vector meson photoproduction is similar to that of hadron-hadron cross section. Differential cross section of the vector meson photoproduction has diffractive features, i.e. a strong forward peak which has been observed in hadron-hadron collision.

These features are understood by the photon-hadron analogy: Quantum mechanics allows a conversion of photon into a quark and a anti-quark pair ($q\bar{q}$) with a photon quantum number ($J^{PC} = 1^{--}$). Neutral vector mesons (ρ, ω, ϕ etc..) have the same quantum numbers as those of photon. It has been discussed that at forward angles, photon behaves as a vector meson and the interaction of vector meson with nucleon occurs when a fluctuation time is long enough, i.e. energy is large (Vector meson dominance [2]).

The weak energy dependence and the exponential decrease of differential cross sections of hadron-hadron scattering as a function of momentum transfer t at high energies are well interpreted as the Pomeron exchange process in the Regge theory. The Regge theory [3, 4] describes high energy hadron-hadron scattering by exchanges of a family of particles in t-channel. These particles belong to a linear trajectory which is called the Regge trajectory.

The Pomeron has been studied in many reaction channels in hadron-hadron scattering, photon-hadron and virtual photon-hadron scattering [5]. Among them, photoproduction of ϕ-meson is a particularly interesting channel. Since the OZI rule strongly suppresses conventional meson exchanges in the t-channel, ϕ-meson photoproduction provides an opportunity to study the Pomeron exchange process and the other non-conventional production mechanisms at low energies. Such a study is difficult in ρ and ω photoproduction since contributions from the

Pomeron exchange process and other non-conventional mechanisms are hidden by the large contribution from meson exchange processes near the threshold. Figure 1.1 shows the total cross sections of ϕ and ρ photoproduction as a function of the center-of-mass energy W. The solid curves are the predictions from the the Pomeron exchange and the dashed curves represent the predictions from meson-exchange [6]. At high energies where the Pomeron exchange is a dominant process, both ϕ and ρ photoproductions behave similarly, i.e. the cross section slowly increases with increasing energy. Contrary to this universal trend at high energies, the cross section increases near threshold in ρ photoproduction, which is an evidence for dominant meson-exchange contribution, while no strong enhancement is seen in ϕ photoproduction due to the suppression of contributions from meson exchange. The small contributions from meson exchange enables us to search for possible non-conventional mechanisms in ϕ photoproduction.

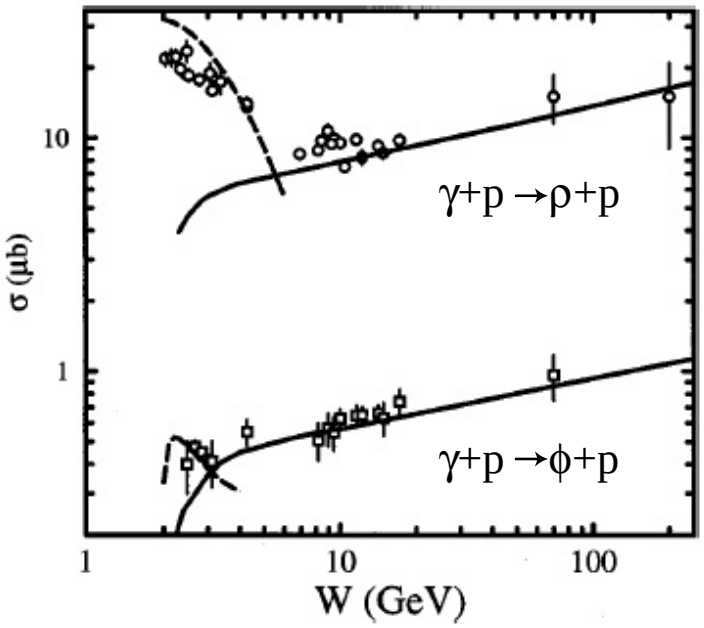

Figure 1.1: Total cross section of ϕ photoproduction and ρ photoproduction as a function of the center-of-mass energy. The solid curves are the prediction from the Pomeron exchange. The dashed curves are the prediction from meson exchange[6]. This figure is taken from Ref. [6]. Data are taken from Ref. [7, 8, 9, 10, 11, 12, 13, 14, 15].

It has been discussed that not only the Pomeron exchange, but also the scalar-glueball exchange (0^+ glueball) [16, 17, 18], tensor-meson exchange (f_2')[19] and $s\bar{s}$ knockout [20] can play important roles in ϕ-meson photoproduction near the threshold. Contributions from these exotic channels are dominant at forward production angles and decrease rapidly as the incident photon energy increases. In contrast, the Regge theory predicts that the contribution from the Pomeron exchange does not depend strongly on photon energy. Therefore, ϕ-meson photoproduction near the production threshold provides an unique way of studying the presence of new mechanisms which might not be seen at high energies or in the other reaction channels. Note that the branching ratio of the non-strange $\phi \to \rho\pi$ decay is 13%. It implies the suppression of meson exchange by the OZI rule is not perfect due to either a small non-strange component in

the ϕ meson wave function or the two-step OZI allowed interactions such as the $\rho\pi \rightarrow K\bar{K} \rightarrow \phi$ process [21].

As we discussed the example of manifestation of the meson exchange in ρ photoproduction, the same argument can be applied to ϕ photoproduction near the threshold although the reliability of the measurement of ϕ-meson photoproduction cross sections is still not enough. Increase of forward angle cross section in ϕ photoproduction reaction near the threshold would imply the presence of a new mechanism different from the standard Pomeron exchange. However, the conventional meson exchanges due to OZI evading mechanisms would also increase the cross section near the threshold. A question is whether the increase of cross section comes from new mechanism or not. Measurements of the cross section alone can not answer this question since the differential cross sections for four different production mechanisms (the Pomeron exchange, pseudo scalar exchange, f_2' exchange and glueball exchange) are expected to behave similarly as shown in Fig. 1.2 [18]. It is difficult to distinguish between new mechanism and conventional mechanisms. However, the decay angular distribution of ϕ meson provides more information to answer this question.

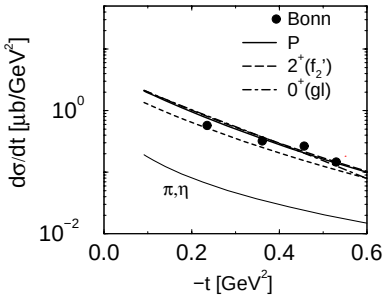

Figure 1.2: Differential cross sections of ϕ photoproduction at $E_\gamma = 2.2$ GeV. The solid, dashed and don-dashed curves indicate the predictions from (P) Pomeron exchange + pseudo scalar exchange, (2^+) f_2' exchange + pseudo scalar exchange and (0^+) glueball exchange + pseudo scalar exchange (0^+), respectively. All the theoretical curves are given in Ref. [18]. The experimental data are taken from Ref. [22].

1.2 Decay angular distribution

The decay angular distribution of ϕ meson contains rich information on the reaction mechanism. The ϕ-meson rest frame is commonly used in the analysis of the decay angular distributions. There are several ways of defining the quantization axis (z-axis) in the frame. We choose a direction of the incoming photon as a z-axis. This choice of z-axis is so-called the Gottfried Jackson (GJ) frame. The GJ frame is the most suitable frame for analyzing the t-channel exchange mechanisms since some of the t-channel exchange amplitudes have a simple helicity-conserving form which is independent of the momentum transfer [17]. In the GJ frame, production plane is defined as a plane on which momentum vectors of the incoming photon and produced ϕ-meson lie. Some papers use another choice of z-axis which is equal to a opposite to outgoing proton in the ϕ meson rest frame (helicity frame). Difference between the GJ frame and the helicity frame is small at very forward ϕ-meson production angles where

the ϕ mesons go to the direction of the incident photon beam (therefore opposite to outgoing proton). The y-axis is defined as a direction normal to the production plane, the x-axis is defined as a direction of outer product $\hat{y} \times \hat{z}$.

We define the following angles ; ϕ, Φ, and θ. θ is the polar angle between the K^+ meson and the ϕ-meson production plane in the ϕ-meson rest frame. ϕ is an azimuthal angle between the K^+ meson and the ϕ-meson production plane in the ϕ-meson rest frame. Φ is an azimuthal angle between the photon polarization vector and the ϕ-meson production plane in the overall center-of-mass frame. The definitions of these angles are shown in Fig.1.3.

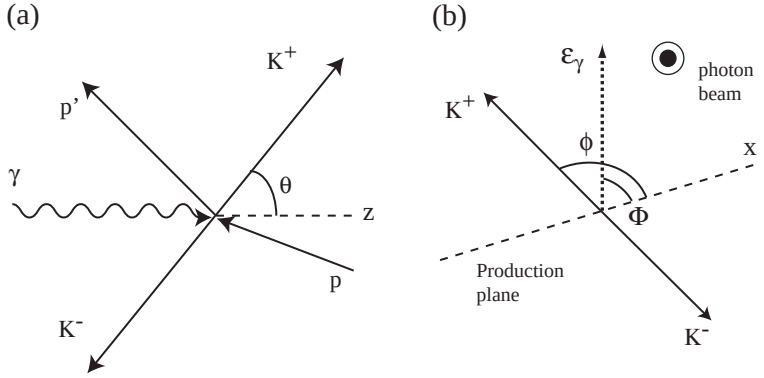

Figure 1.3: Decay angles (Gottfried-Jackson frame) for the reaction $\gamma + p \rightarrow \phi + p \rightarrow K^+K^-p$. (a) diagrammatic representation of the system viewed from the x-axis, (b) the system viewed from the z-axis, where the arrow with $p(p\prime)$ stands for direction of the incident (outgoing) proton, and ϵ_γ represents the direction of the photon polarization.

The decay angular distribution $W(\phi, \theta, \Phi)$ for ϕ photoproduction by linearly-polarized photons are expressed using nine spin-density matrix elements ρ^0,ρ^1,ρ^2 and the polarization degree of the photon beam P_γ [23]:

$$W(\phi, \theta, \Phi) = (W^0 - P_\gamma \cos(2\Phi) W^1 - P_\gamma \sin(2\Phi) W^2) \tag{1.1}$$

$$\tag{1.2}$$

where, W^0 is the polarization-independent part and W^1 and W^2 are polarization-dependent parts. W^0, W^1 and W^2 are represented in following form:

$$\begin{aligned}
W^0 &= \frac{3}{4\pi}\left(\frac{1}{2}(1-\rho^0_{00}) + (3\rho^0_{00}-1)\cos^2\theta \right. \\
&\quad \left. -\sqrt{2}Re(\rho^0_{10})\sin(2\theta)\cos\phi - \rho^0_{1-1}\sin^2\theta\cos(2\phi)\right), \\
W^1 &= \frac{3}{4\pi}(\rho^1_{11}\sin^2\theta + \rho^1_{00}\cos^2\theta \\
&\quad -\sqrt{2}Re(\rho^1_{10})\sin(2\theta)\cos\phi - \rho^1_{1-1}\sin^2\theta\cos(2\phi)), \\
W^2 &= \frac{3}{4\pi}(\sqrt{2}Im(\rho^2_{10})\sin(2\theta)\sin(\phi) + Im(\rho^2_{1-1})\sin^2\theta\sin(2\phi))
\end{aligned} \tag{1.3}$$

The three-dimensional angular distribution Eq. 1.1 can be reduced to one-dimensional distribution for a particular angular variable after integrating over the other remaining angles

:

$$
\begin{aligned}
W(\cos\theta) &= \frac{3}{2}(\frac{1}{2}(1-\rho^0_{00})\sin^2\theta + \rho^0_{00}\cos^2\theta)) && (1.4)\\
W(\phi) &= \frac{1}{2\pi}(1 - 2\mathrm{Re}\rho^0_{1-1}\cos 2\phi) && (1.5)\\
W(\phi-\Phi) &= \frac{1}{2\pi}(1 + P_\gamma(\rho^1_{1-1} - \mathrm{Im}\rho^2_{1-1})\cos 2(\phi-\Phi)) && (1.6)\\
W(\phi+\Phi) &= \frac{1}{2\pi}(1 + P_\gamma(\rho^1_{1-1} + \mathrm{Im}\rho^2_{1-1})\cos 2(\phi+\Phi)) && (1.7)\\
W(\Phi) &= \frac{1}{2\pi}(1 - P_\gamma(2\rho^1_{11} + \rho^1_{00})\cos 2\Phi) && (1.8)
\end{aligned}
$$

The spin-density matrix elements (ρ^0, ρ^1, ρ^2) are bilinear combinations of scattering amplitude. We follow the standard definition given in Ref. [18]:

$$
\begin{aligned}
\rho^0_{\lambda\lambda'} &= \frac{1}{N}\sum_{\alpha,\lambda_\gamma} I_{\alpha;\lambda,\lambda_\gamma}\, I^\dagger_{\alpha;\lambda',\lambda_\gamma},\\
\rho^1_{\lambda\lambda'} &= \frac{1}{N}\sum_{\alpha,\lambda_\gamma} I_{\alpha;\lambda,-\lambda_\gamma}\, I^\dagger_{\alpha;\lambda',\lambda_\gamma},\\
\rho^2_{\lambda\lambda'} &= \frac{i}{N}\sum_{\alpha,\lambda_\gamma} \lambda_\gamma I_{\alpha;\lambda,-\lambda_\gamma}\, I^\dagger_{\alpha;\lambda',\lambda_\gamma}, && (1.9)
\end{aligned}
$$

where λ_γ, λ ($\lambda\prime$) are helicity of the incoming photon, helicity of outgoing ϕ meson, respectively. I represents the scattering amplitude, and N is a normalization factor. α is a set of the other quantum numbers including the polarization of the incoming and outgoing proton. The scattering amplitude I consists of helicity conserving amplitude ($\equiv I_{\lambda,\lambda}$) and helicity non-conserving amplitude ($\equiv I_{\lambda,\lambda'}$ with $\lambda \neq \lambda'$). As shown in Eq. 1.9, the spin-density matrix elements are the product of these two types of amplitudes. When only helicity-conserving amplitudes are present in the process, the elements ρ^1_{1-1} and $\mathrm{Im}\rho^2_{1-1}$,which contain products of helicity-conserving amplitudes, are possible to have non-zero values. All the other elements, in which all terms contain helicity non-conserving amplitudes, are 0 ; i.e. Eq. 1.9 leads :

$$
\begin{aligned}
\rho^1_{1-1} &= \frac{1}{N}\sum_{\alpha,\lambda_\gamma} I_{1,-\lambda_\gamma}\, I^\dagger_{-1,\lambda_\gamma}\\
&= \frac{1}{N}\sum_{\alpha} I_{1,-1}\, I^\dagger_{-1,1} + I_{1,1}\, I^\dagger_{-1,-1}\\
&= \frac{1}{N}\sum_{\alpha} I_{1,1}\, I^\dagger_{-1,-1}\\
&= -\mathrm{Im}\rho^2_{1,-1}\\
&\quad \rho^0_{00} = \rho^0_{1-1} = \mathrm{Re}\rho^0_{10} = \rho^1_{00} = \mathrm{Re}\rho^1_{10} = \rho^1_{11} = \rho^2_{10} = 0. && (1.10)
\end{aligned}
$$

The amplitudes for Pomeron exchange, scalar (0^+ glueball) exchange (natural-parity exchange, $J^P = 0^+$) and pseudo scalar (π,η) exchange (unnatural-parity exchange, $J^P = 0^-$)

are examples of the helicity-conserving amplitude at forward angles. Pure natural-parity exchange gives $\rho^1_{1-1} = -\mathrm{Im}\rho^2_{1-1} = +1/2$, while pure unnatural-parity exchange gives $-1/2$. When both of these two contribute to the scattering amplitude with a relative weight β ($I_{tot} = \sqrt{1-\beta^2}I^N + \beta I^{UN}$), the spin-density matrix elements are given by

$$\rho^1_{1-1} = -\mathrm{Im}\rho^2_{1-1} = \frac{1-2\beta^2}{2}, \tag{1.11}$$

and all the other elements are zero. Therefore, information on ρ^1_{1-1} and $\mathrm{Im}\rho^2_{1-1}$ provides the relative weight (β) between natural-parity exchange and unnatural-parity exchange under the absence of the helicity non-conserving amplitudes.

When the helicity non-conserving amplitude is present, the other seven spin-density matrix elements could have non-zero value. Examples of helicity non-conserving amplitude are the tensor meson (f'_2) exchange, and the production of nucleon resonances which couples to ϕN. At finite angle, Pomeron exchange could also violate the helicity conservation due to the spin-orbit and spin-spin interaction [18]. Fig. 1.4 shows predictions of the decay angular distribution for the Pomeron exchange, f'_2 exchange (2^+) and glueball exchange (0^+). A large helicity non-conserving contribution from f'_2 exchange results in remarkable difference in the angular distributions, while the Pomeron and glueball exchanges give similar distributions.

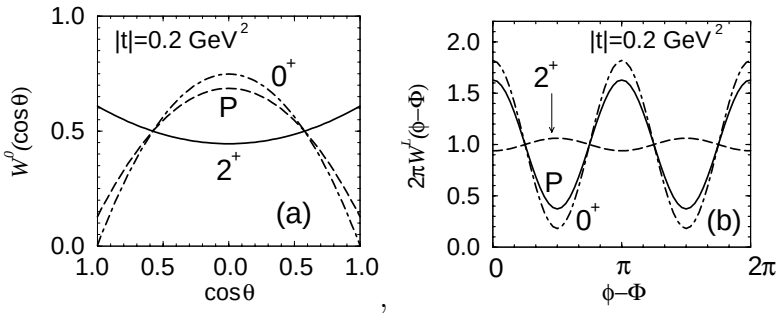

Figure 1.4: Predictions for the decay angular distribution by Ref. [18]. (a) $\cos\theta$ distribution (b) $\phi - \Phi$ distribution, for ϕ photoproduction at E_γ =2.2 GeV. The Solid, dashed and don-dashed curves indicate the predictions from (P) Pomeron exchange + pseudo scalar exchange, (2^+) f'_2 exchange + pseudo scalar exchange and (0^+) glueball exchange + pseudo scalar exchange (0^+), respectively.

In this way, ϕ-meson photoproduction measurement with a linearly-polarized photon beam allows us to study the detailed ϕ-meson production mechanism. Especially, a measurement of decay angular distributions of ϕ-meson is a powerful tool to decompose the scattering amplitude into a natural-parity exchange part (Pomeron and glueball) and an unnatural-parity exchange part (π and η). The experimental data for ϕ-meson photoproduction at higher energies (E_γ = 2.8, 4.7 and 9.3 GeV) [7](Fig. 1.5) have revealed a dominance of helicity-conserving amplitude with natural-parity exchange. On the other hand, there is a clear energy dependence of decay angular distributions for the ω photoproduction measured at forward angles ($0.02 < |t| < 0.3$ GeV^2) [7]. The reduction of modulation in the $\phi - \Phi$ distribution at lower energies can be understood from increase of π exchange contribution since ω meson strongly couples to π meson. This demonstrates that the decay angular distribution is well used as a parity filter.

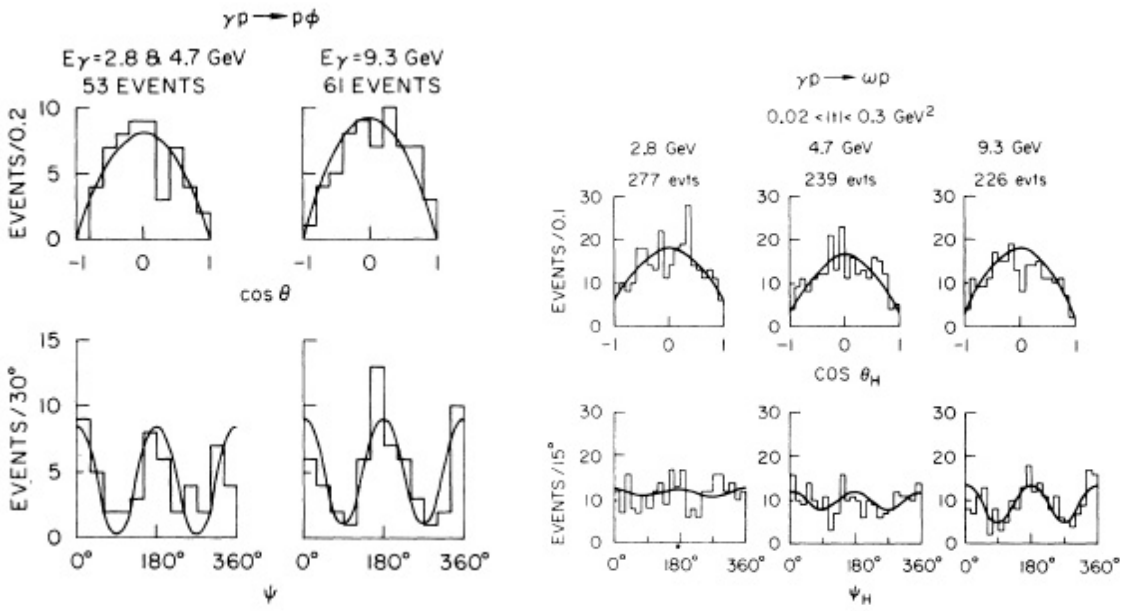

Figure 1.5: $\cos\theta$ and $\psi(\equiv \phi - \Phi)$ distributions for ϕ photoproduction (left-hand side) and ω photoproduction (right-hand side) in the helicity frame measured by Ballam et al. [7]. The curves in plots for ϕ photoproduction are the fits to the data assuming helicity conservation in the helicity frame, the curves in plots for ω photoproduction are the fits to the data without assumption of helicity consrvation.

In order to investigate a possible new production mechanism, such as the scalar (glueball) exchange, the measurements of cross sections and spin-density matrix elements near the threshold at forward angles are necessary. However, no precise experimental data is available at forward angles near the threshold although several measurements for this reaction have been reported [7, 13, 22, 24, 25, 26, 27, 28].

In this thesis, we report the first measurement of decay angular distributions and differential cross sections at very forward angles near the ϕ photoproduction threshold with a linearly-polarized photon beam.

Chapter 2

Experimental apparatus

The decay angular distributions and the differential cross sections of ϕ photoproduction were measured at the SPring-8/LEPS facility. The linearly-polarized photons were produced at SPring-8 BL33LEP beamline (LEPS facility). The liquid hydrogen target was installed and irradiated to the beam. The LEPS facility consists of a laser transport system, a photon tagging system (tagger), a liquid hydrogen target and a charged particle spectrometer. The experimental apparatus of the measurement is described in this chapter.

2.1 The beam

2.1.1 The backward Compton scattering

A Compton scattering of photons by electrons is an one of the most simple process in quantum electrodynamics (QED). In 1963, Milburn [29] and Tumanian [30] pointed out that high energy polarized photons are produced by collisions of polarized laser photons with relativistic electrons at a direction of electrons. This process is generally called as Backward Compton scattering (BCS). Energies of scattered photons are the same order of magnitude as those of electrons. For example, a few GeV photons are able to be produced by shooting a few eV light to 8 GeV electrons.

The BCS provides an opportunity to obtain high energy photon beams in electron accelerators. The first photon beam facility by using the BCS technique for physics measurements has been built at SLAC [7] in 1969. Since 1969, the BCS technique has been used to make a high energy photon beam [31, 32, 33]. On the basis of these facility construction and of the new development of laser technology, we have built a new facility (LEPS facility) for the BCS photon beam at the SPring-8 of Hyogo, Japan for the measurements of photoproduction of mesons and/or baryons [34]. The LEPS facility provides the BCS photon beams of the world highest energies (maximum 2.4 GeV) where the photoproduction of the ϕ meson can be studied from the threshold (E_γ=1.573 GeV). The Ar-ion laser (Coherent Sabre) was used as a source of photons in the UV region (333.6-363.8 nm).

An energy spectrum of scattered photons in the BCS process has a quasi-flat shape. On the other hand, the production of Bremsstrahlung photons, which is widely used to produce high energy photons, results in a spectrum proportional to $\sim 1/E_\gamma$, i.e. many low energy photons are produced due to the divergence at low energy. Low energy photons, which can not

produce ϕ mesons, generate a large amount of e^+e- pair backgrounds. Amount of such low energy photons can be much reduced in the BCS photon beams. Figure 2.1 (left-hand side) shows the energy spectrum of the BCS photons produced from the collision of 351 nm (single line) laser against the 8 GeV electron beam at the SPring-8 storage ring. The measurement was performed by using a full-absorption type electromagnetic calorimeter consists of PbWO crystals [35]. For comparison, the energy spectrum of the Bremsstrahlung photon when the laser light was turned off is shown in right-hand side of fig. 2.1. The flatness of the energy spectrum of the BCS photon beam compared to the Bremsstrahlung photon is evident.

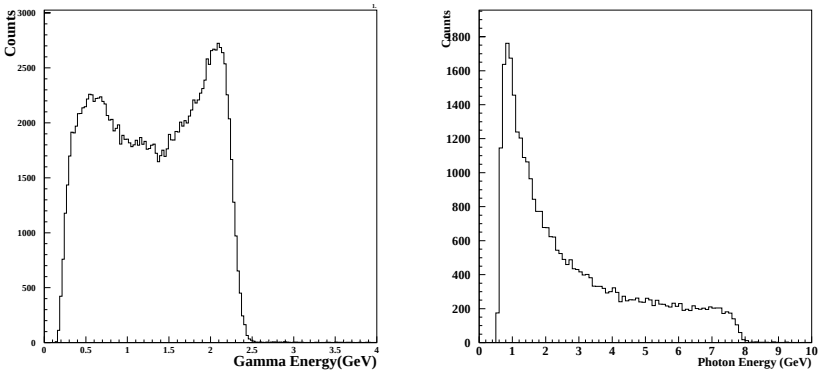

,

Figure 2.1: Energy spectrum of the BCS photon at the LEPS facility (left-hand side), Energy spectrum of the gas Bremsstrahlung photon (right-hand side)

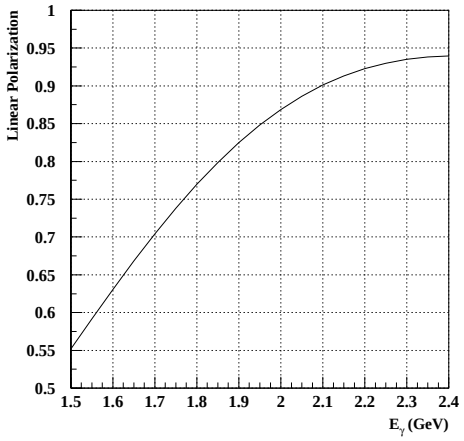

Figure 2.2: Linear polarization as a function of photon energy. 100% polarization of the laser light is assumed in the calculation.

Since the polarization of laser light is transferred to the photon beam according to the QED, high degree of polarization can be easily achieved. The linear polarization of the BCS photons depends on photon energy as shown in Figure 2.2. The maximum polarization amounts to

94% for the highest photon energy (2.4 GeV) when a 100% linearly-polarized laser is used. There is no major difficulty for controlling the polarization states of the BCS photons since the direction of the laser polarization is easily handled. The high degree of polarization allows us to perform precise measurements of polarization observables which are important to unveil the reaction mechanisms as discussed in Section 1.2.

2.1.2 Beamline set-up

The SPring-8 (Super Photon ring-8 GeV) is the facility of the 3rd generation synchrotron radiation source. The SPring-8 composed of 1 GeV injector linac, 8 GeV booster synchrotron, and 8 GeV electron storage ring. There are 61 beamlines available for scientific research activities [36]. The Laser-electron photon facility was built at the beamline BL33LEP which is dedicated for the experiments of subnuclear physics research [37, 38, 39, 40, 41, 42, 43].

The laser optics

A schematic view of the laser optics is shown in Fig. 2.3. An Ar-ion laser (Coherent Sabre) was used as a source of photons. The laser was operated with a multi-line mode. The wave length of the laser beam consists of several lines in the UV region (333.6-363.8 nm) where the major components are 351.1 nm and 363.8 nm. Thanks to the property of laser resonator, the emitted laser beam is almost 100% linearly polarized. A typical power of the laser beam was about 5 W. The laser beam size was enlarged by a beam expander, which consisted of a couple of optical lens to focus at the straight section of the storage ring where the electron beam circulated. Four optical mirrors were used to navigate the laser beam to the storage ring. The direction of linear polarization of the laser beam was controlled by a half wave length plate ($\lambda/2$ plate). We set the direction of the linear polarization (define as the direction of the electric field) to the vertical direction and the horizontal direction in the measurement. The direction of polarization was changed in every a few hours. The polarization angle and degree were measured at the end of the straight section in the storage ring. A Glan-laser prism was used as a polarization analyzer. In the polarization measurement, the Glan-laser prism was rotated and the intensity of the laser was measured behind the prism with a photodiode as a function of rotation angle of the polarizer. Fig. 2.4 shows the intensity distributions of the laser after a polarizer for the vertical and horizontal polarized laser. The angle and degree of the polarization were obtained by analyzing spectrum [44].

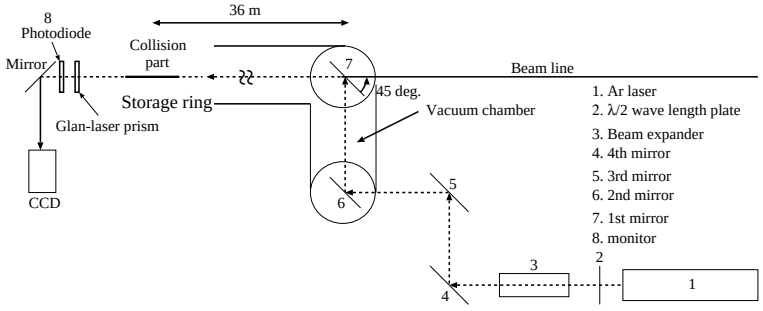

Figure 2.3: Laser optics of the LEPS facility

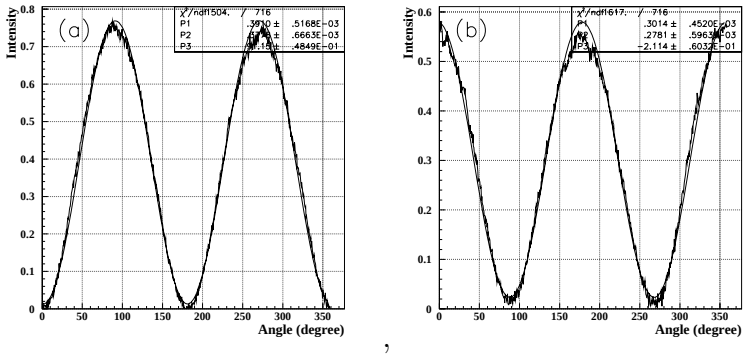

Figure 2.4: Intensity of photo-diode output as a function of the angle of the Glan-laser prism for (a) vertically polarized laser, (b) horizontally polarized laser [44]. The curves are the results of fitting to the data with a function of sine function plus constant.

2.2 The tagger

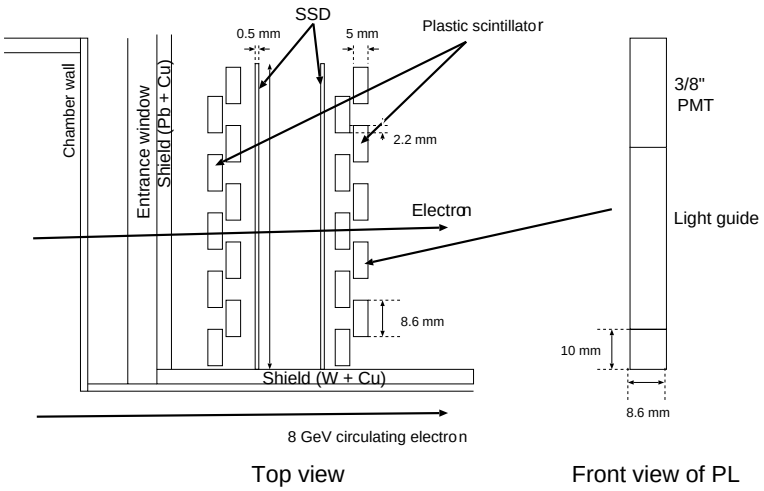

Figure 2.5: The tagging counter

The energy of photons was determined by measuring the energy of the recoiled electron $E_{e'}$. The energy conservation of the electron and photon leads the energy of photons as $E_\gamma = E_e - E_{e'}$ where E_e is the energy of the electron beam circulating in the storage ring (7.975 ± 0.003 GeV [45]). The recoiled electrons were detected with the tagging counter which was installed at the downstream of the bending magnet of the storage ring. The backward Compton scattering takes place at the straight section of the storage ring. The recoiled electrons passed through the bending magnet which bent the recoiled electron trajectory. Displacement of the trajectory at the downstream of the bending magnet depends on the energy of recoiled electrons. The position of tagging counter was corresponded to displacement of the recoiled electron from which the energy of photon was obtained. The tagging counter consisted of two layers of plastic scintillation counters and two layers of silicon strip detectors (SSD). A schematic view of the tagging counter is shown in Fig. 2.5. A layer of the plastic scintillation counter consisted of 10

segments of plastic scintillators which provided a timing signal of the recoiled electron signal. SSD consisted of 512 readout strips with a $100\mu m$ pitch which provided position information for the recoiled electron trajectory. The energy of photon was obtained by the position of the SSD strip. The photon energy resolution was 15 MeV [46] which was determined by the energy resolution of the electron beam and the performance of the bending magnet as a momentum analyzer for recoiled electrons. With the tagging counter, the photon energy from 1.5 GeV to 2.9 GeV was covered. The efficiency of the tagging counter will be described in Section A.

2.3 The target

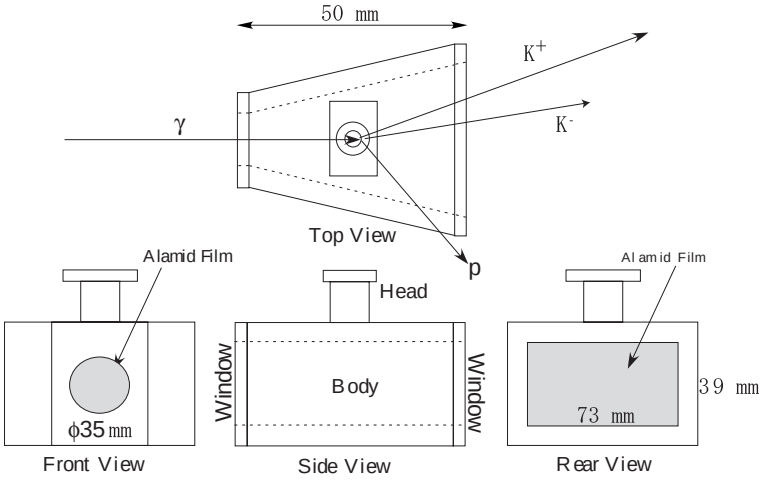

Figure 2.6: The liquid hydrogen target

A 50mm-long liquid hydrogen target [47] was used in the experiment. The size and shape of the target is shown in Fig. 2.6. The target cell was made of copper with a thickness of 8 mm. The entrance and exit windows of the target cell were made of Alamid films with a thickness of 0.05 mm. The target was located at the 952 mm upstream of the center of the dipole magnet (Section 2.4). The temperature and pressure of the target was kept at 20.5 K and 1.05 atom, respectively. The shape of the target cell was designed so that the target cell did not cut the acceptance of the charged particle spectrometer even when the reaction took place at the upstream of the target cell.

2.4 The charged particle spectrometer

The charged particle spectrometer consisted of a dipole magnet, tracking detectors, a start counter, a silica aerogel Čerenkov counter, an upstream veto counter and a time-of-flight counter. A schematic view of the charged particle spectrometer is shown in Fig. 2.7.

The dipole magnet provided the magnetic field for momentum analysis. Aperture of the dipole magnet was 55 cm high and 135 cm wide. The length of the pole along the photon beam was 60 cm. The maximum field strength was 0.7 T at center of the dipole magnet. A current provided to the magnet was 800 A. A magnetic field map was calculated by using OPERA-3d

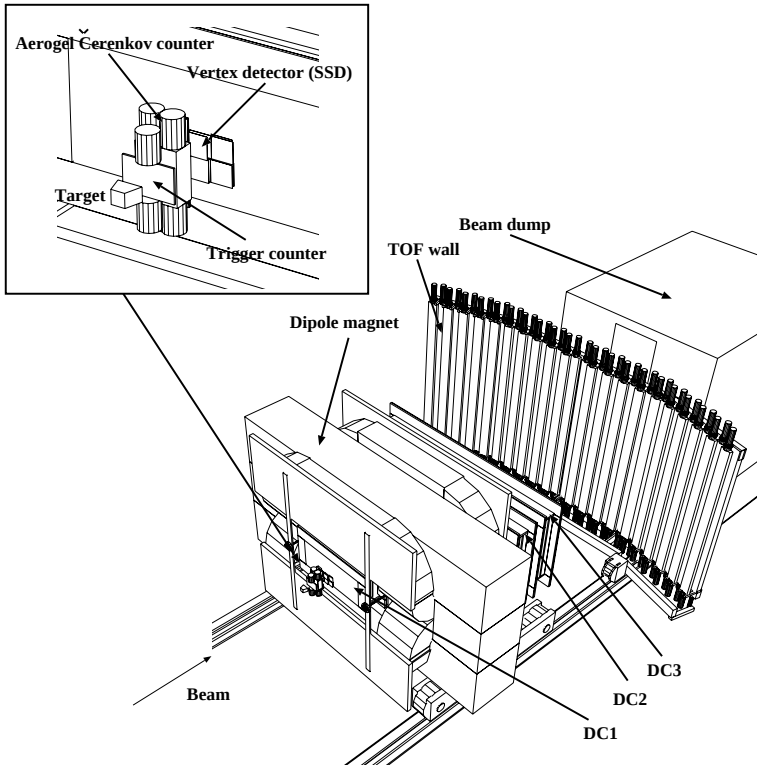

Figure 2.7: The LEPS charged particle spectrometer

TOSCA package [48] which provided the 3-dimensional magnetic field distribution. Results of the calculation by TOSCA agreed well with the measurements by hole probes. Inside the magnet, a pair of lead bar with 4 cm thick, 4 cm high and 44 cm wide were installed in the horizontal plane at the 20 cm downstream of the magnet center in order to block the e^+e^- pairs produced at upstream.

The tracking detectors consisted of a silicon vertex detector (SVTX) and three drift chambers (DC1, DC2 and DC3). The SVTX and DC1 were located at the upstream of the dipole magnet and DC2 and DC3 were located at the downstream.

The SVTX was a silicon strip detector with a thickness of 300 μm and with 120 μm strip pitch. Total number of strip was 8192 strip. Half of the strip were placed in the vertical direction and the other half were placed in the horizontal direction. There was a hole at the center of the detector where the photon beam went through without having any reactions with the detector. The efficiency of the SVTX detector was checked by good proton tracks reconstructed without using the SVTX hits. The efficiency was 100% for most of strips. There were 56 strips which were very noisy; They always gave high noise signals due to electrical noise (hot strip). The hot strips were killed in the offline analysis. The efficiency of the strips next to the hot strip were not 100% but 97% because of imperfection of collecting charge induced by the charged particle.

The DC1 consisted of 6 planes. There were 3 planes for the x direction, 2 planes for the u direction and 1 plane for the v direction). The u and v planes were inclined by +45° and -45° with respect to the vertical direction. The field wires were arranged in a hexagonal shape. The active area of the DC1 was 30 cm high and 60 cm wide. The wire spacing of sense wires was

12 mm. The total number of wire for the x, u and v planes were 144, 96 and 48, respectively. The DC2 and DC3 have same structure. They consisted of 5 planes with the two x plane, the two u plane and the one v plane. Here u and v planes were inclined by +30° and -30° with respect to the vertical direction. The field wires were arranged in a hexagonal shape. The active area of the DC2 and DC3 was 80 cm high and 200 cm wide. The spacing of sense wires was 20 mm. The windows of the entrance and exit of the DC1, DC2 and DC3 were made of Alminized-mylar sheet with a thickness of 125 μm. The efficiency of the drift chambers were 97-100% and the resolution was found to be approximately 200 μm [42].

The time-of-flight of the charged particle was measured using the start counter (TRG), the time-of-flight (TOF) counter, and RF signal of the accelerator. The start counter, which was made of a 5 mm thick plastic scintillator with 94 mm high 150 mm wide, provided a start timing of the trigger of data taking. The TOF start timing was given by the timing of RF signal of the accelerator with a frequency of 508 MHz. However, we found that there was a problem of RF signal in a part of data. In such a case, the start counter was used as a TOF start timing instead of the RF timing when RF signal was not valid. The TOF stop timing was provided by the TOF counter which consisted of 40 slats of 40 mm thick plastic scintillator with 2000 mm high and 120 mm wide. An average of timing resolution of TOF measurement was 123 psec when RF signal was used, and 170 psec when the start counter was used [49].

The silica aerogel Čerenkov counter (AC) was located at the downstream of the start counter to veto the events for e^+e^- pair creation in the trigger level. The index of the silica aerogel was 1.03. The Čerenkov threshold momentum for electron, pion and kaon were 0.002 GeV, 0.57 GeV and 2.0 GeV, respectively. The inefficiency of the Čerenkov counter for e^+e^- was about 0.1% [49].

The upstream veto counter (UPveto) was a plastic scintillation counter with a thickness of 5 mm, 200 mm high and 190 mm wide which was located at the 4 m upstream from the target. The UPveto was used to veto charged particles most of which are e^+ and/or e^- produced at upstream in trigger level.

2.5 Data acquisition

The trigger for the data taking [50] consisted of (1) a tagger signal (TAG) which was defined as the coincidence signal of valid signals of scintillator in each layer, (2) a signal from UPveto, (3) a signal from TRG, (4) signal from AC, (5) a signal from TOF. Diagram of the readout logic for trigger was shown in Fig. 2.8. The main trigger (hadron trigger) was defined as $(1) \times (\bar{2}) \times (3) \times (\bar{4}) \times (5)$. Another trigger ($e^+e^-$ trigger) to monitor the detector by using e^+e^- event was prepared. The e^+e^- trigger was define as $(1) \times (\bar{2}) \times (3) \times (5)$, i.e. veto signal for AC was removed from the hadron trigger. The diagram of trigger logic is shown in Fig. 2.9. In the experiment, data were taken by these two triggers. The e^+e^- trigger was prescaled so that trigger rate is sufficiently low. A typical trigger rate for the hadron trigger was 20 cps. The trigger rate for the prescaled-e^+e^- trigger was 4 cps.

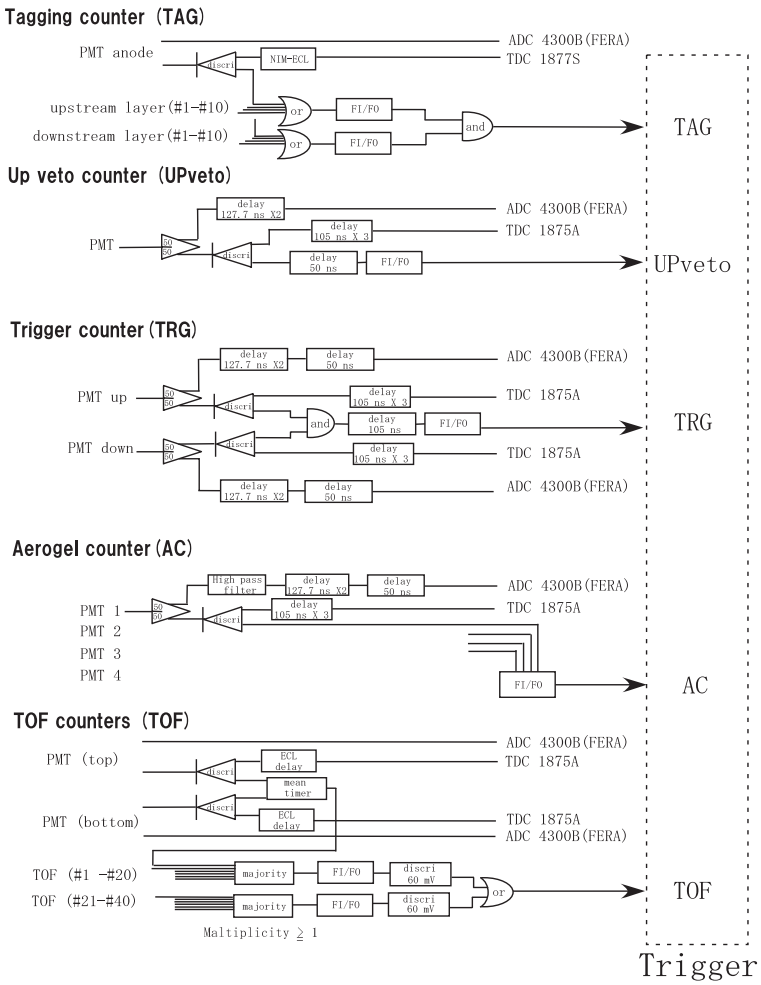

Figure 2.8: Read out logic

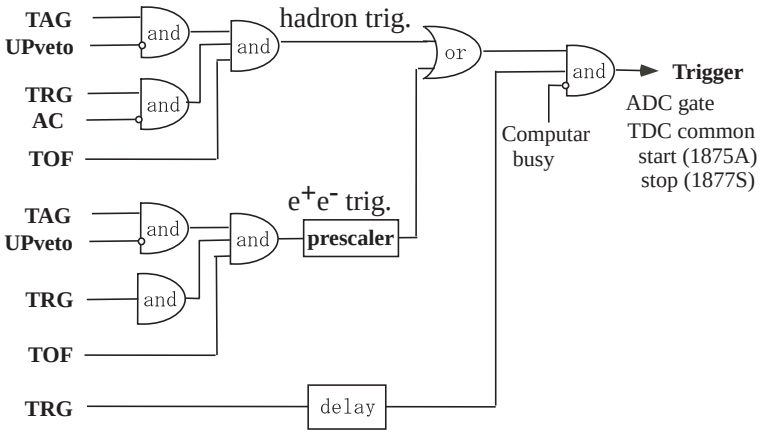

Figure 2.9: Trigger logic

Chapter 3

Data analysis

In this chapter, data analysis for the ϕ photoproduction is presented.

3.1 Offline analysis program, LEPSana

A general offline analysis program (LEPSana) was developed to extract information on the beam energy and momenta, positions, mass of charged particles from the experimental data. The LEPSana reads the raw experimental data and proceses a sequence of analysis. All necessary calibrations have been made in advance and properly implemented in the LEPSana. The outputs of the process were written in the NTUPLE format [51] and further analysis was done by accessing the ntuple in PAW.

Some of the calibration parameters, such as (1) timing offset and PMT gain of the TOF counter [49] and the tagging counter (2) timing offset, x-t curve (a conversion function from drift time to drift distance) and resolutions of the drift chambers [42], have been varied during the long run periods of data taking. Variation of calibrations were implemented by an file-control interface which handled run-by-run based parameters.

3.2 g3leps, Momte Carlo simulator

The acceptance of the LEPS spectrometer for the ϕ photoproduction was studied by a Monte Carlo simulator for the LEPS spectrometer, g3leps [52] which was developed based on the CERN program library, GEANT 3.21 [53]. The g3leps simulates a generation of particles from the ϕ photoproduction reaction and processes during passage of the particles through the experimental apparatus, such as particle decay, energy loss, multiple scattering. The GHEISHA package was used to simulate hadronic interactions. The g3leps describes responses of the detectors followed by a passage of the particles. The measured resolution and efficiency of the SVTX and the drift chambers, timing resolution of the TOF counter were implemented in the g3leps. A realistic beam shape of the polarized-photon beam and the beam energy resolution were implemented as well.

Data from the Monte Carlo simulator was linked to the offline analysis program, LEPSana which was used to analyze the real data. Monte Carlo data was analyzed by exactly the same analysis processes as in the case of the real data.

A Monte Carlo event generator dedicated for the generation of ϕ photoproduction reaction was developed. The ϕ-meson event generator generated K^+K^- and proton from the reaction $\gamma + p \rightarrow \phi + p$, $\phi \rightarrow K^+ + K^-$ in the ϕ-meson rest frame with user-defined parameterization of cross section as a function of energy, momentum transfer and spin density matrix elements. The acceptance for ϕ photoproducion was studied by this Monte Carlo simulator (See Section 3.7).

For the study of the backgrounds in the K^+K^-p final state, we made another event generator which generated the K^+K^-p without forming any resonance in neither the K^+K^- system nor the K^-p system (see Section 3.6).

3.3 Event selections

The K^+K^- decay mode of ϕ meson was used to identify photo-production of ϕ mesons. Several selections to identify elastic photoproduction of ϕ meson from protons were applied to the data. Definitions of selection cuts are described in this section.

3.3.1 Pre-selections

At the first stage of the offline analysis, pre-selections were applied to the data. The pre-selections are defined in Table 3.1. The main purpose of the pre-selections was to reject events which are commonly useless for any types of physics analysis. The pre-selections consisted of a cut to reject broken data block due to DAQ error, a cut on number of the TOF counter hits, a cut on the time-of-flight and the energy deposit of the TOF counter, cuts on number of raw hits in the drift chambers and the silicon vertex detector (SSD). After applying all of the cuts mentioned above, data were fed into the track finding routine in which charged particle tracks were reconstructed from a combination of detected hits by the Runge-Kutta method. In total, 4.37×10^7 events with charged tracks were survived.

Table 3.1: Cut definitions of pre-selection

Cuts	Definitions
DAQ ERR	
NTOF	Number of clusters in the TOF counter >0
TOFSQRT	Energy deposition in the TOF counter(adctof) >0.7 MIP
TOF	13<Time-of-flight(tof) <60 nsec
TOF_ADC	adctof >2.2 MIP and (tof-adctof*10.-15.)>0
NHIT_DC	Total number of hits in the drift chambers>11
DC1HIT	Number of cluster in DC1 >0
SSDHIT	Number of cluster in SSD >0

3.3.2 Track selection cuts

In order to identify the ϕ photoproduction reaction ($\gamma + p \rightarrow \phi + p$) unambiguously, the momenta of at least two out of three charged particles (K^+, K^- and p) in the final state and the incident photon energy had to be known. There were four types of event topologies which were used to identify the reaction; K^+K^-p-reconstructed events, K^+K^--reconstructed events and $K^\pm p$-reconstructed events. Events reconstructed from K^+K^- ($K^\pm p$) tracks were categorized as the KK mode (KP mode). Events reconstructed from the K^+K^-p track were called KKP mode. Note that there was a big difference of the kinematical coverage due to the acceptance for different event topologies although there was a small overlap between each other (See Section 3.5).

Cuts to select each reconstruction mode (KK, KP, KKP mode) are listed in Table 3.2. They consist of a cut on the number of tracks, the decay-in-flight cuts and the PID cuts.

Table 3.2: Cut definitions of track selection

Cuts	Definitions
NTRK2	number of reconstructed track>1
K^+PID	positive charge, $0.1 < m^2 < 0.55$ GeV^2
K^-PID	negative charge, $0.1 < m^2 < 0.55$ GeV^2
p PID	positive charge, $0.55 < m^2 < 1.20$ GeV^2
DIF	$\lvert y(track) - y(tof)\rvert < 80$ mm $\lvert x(track) - x(tof)\rvert < 1$ TOF slat number of outlier hits $\leq$6 prob(χ^2)>0.02
KKP CUT	NTRK2 .and. K^+PID .and. K^-PID .and. p PID .and. DIF
KK CUT	NTRK2 .and. K^+PID .and. K^-PID .and. DIF
K$^\pm$P CUT	NTRK2 .and. $K^\pm$PID .and. p PID .and. DIF

Decay-in-flight cuts

The event sample was cleaned up by removing tracks with large track-reconstruction errors due to decay-in-flight events (decay-in-flight cut). The decay-in-flight cut consisted of three parts:

- cuts on difference of positions between reconstructed track at the TOF counter and the position measured by the TOF counter was made. When the difference of y coordinate was greater than 80 mm or difference of the TOF slat number was greater than 1, those tracks were rejected by this cut.

- hits of tracking chambers which deviated from the expected trajectories more than the resolution were considered as a outlier and removed from the tracking. A cut on number of outliers hits was applied. Decay-in-flight event had a track with a large number of outliers when it decayed in the middle of tracking volume (between SVTX and DC3). When the number of outliers were greater than 6, the tracks were rejected in the analysis.

- a cut on χ^2 probability of a fitting of the track reconstruction was applied. The χ^2 probability of reconstructed track was required to be greater than 0.02.

The decay-in-flight cuts were applied not only for K mesons but also for proton tracks which have large reconstruction error due to mis-measurements of track position, such as mis-solving of left-right ambiguity of the drift chamber hits caused by the multiple scattering.

Particle identification (PID)

The reconstructed mass distributions for positive charged particles and negative charged particles are shown in Fig. 3.1. Note that deuteron and He^{++} were not produced at the LH_2 target, but produced at the target cell, holder or the start counter. The average resolution of the TOF counter (σ_{tof}) was measured to be 175 psec in real data [49]. Typical mass resolution is 30 MeV for 1 GeV Kaon. The PID cut points are shown in Fig. 3.2. The cut points for $K^{\pm}$ and proton were defined as $0.1 < m^2 < 0.55$ GeV^2 and $0.55 < m^2 < 1.20$ GeV^2, respectively. These cut points were determined to maximize the acceptance of the PID cuts considering variations of the TOF resolution and the mis-measurements of TOF.

For the normal events in which TOF were correctly measured, the reconstructed mass resolution $\sigma(m^2)$ was parameterized as:

$$\sigma(m^2)^2 = 4m^2(\sigma_{ms}^2(1+(m/p)^2) + \sigma_{spe}^2 p^2) + 4p^2(p^2+m^2)(\sigma_{tof}(c/L))^2 \tag{3.1}$$

where p, m and L are momentum, mass, and flight-path length of the particle, σ_{ms} is a contribution from the multiple scattering in momentum measurement. The σ_{spe} and σ_{tof} are resolution of angle measurement by the spectrometer and time-of-flight resolution. c stands for the speed of light. The Monte Carlo simulation were used to check the validity of Eq. 3.1. It was found that the simulation reproduced momentum dependence of the mass distribution reasonably well. The σ_{ms} and σ_{spe} were obtained from a fitting of the mass spectrum in the Monte Carlo calculation. They were found to be $\sigma_{ms} = 0.00458$ rad and $\sigma_{spe} = 0.00323$ GeV^{-2}. We have checked the validity of the obtained parameters describing the reconstructed mass resolution in the real data.

There are two sources of the mis-measurements of TOF :

- When there was no valid RF signal, the start counter was used as a TOF start timing. The determination of the start timing went systematically wrong when two or more charge particles hit the start counter with different timing.

- When the ADC of TOF counter was saturated due to large energy deposit of the charged particle, the slewing correction (time walk correction) to the timing measurement was too small. This introduced systematically larger TOF.

For both of above cases, we introduced phenomenological correction to the TOF measurement. However, mass resolutions for these cases were worse than those in normal events.

Therefore, the PID cut points were set to larger than the mass resolutions given by Eq. 3.1. Typically, the PID cut points corresponds to more than 4 σ for the particle below p<1 GeV.

In total, 721 (KKp mode) events , 11380 (KK mode), 11641 (K^-p mode), 69729(K^+p mode) passed the track-selection cuts. Summary of track-selection cuts are shown in Table 3.3, 3.4, 3.5 and 3.6.

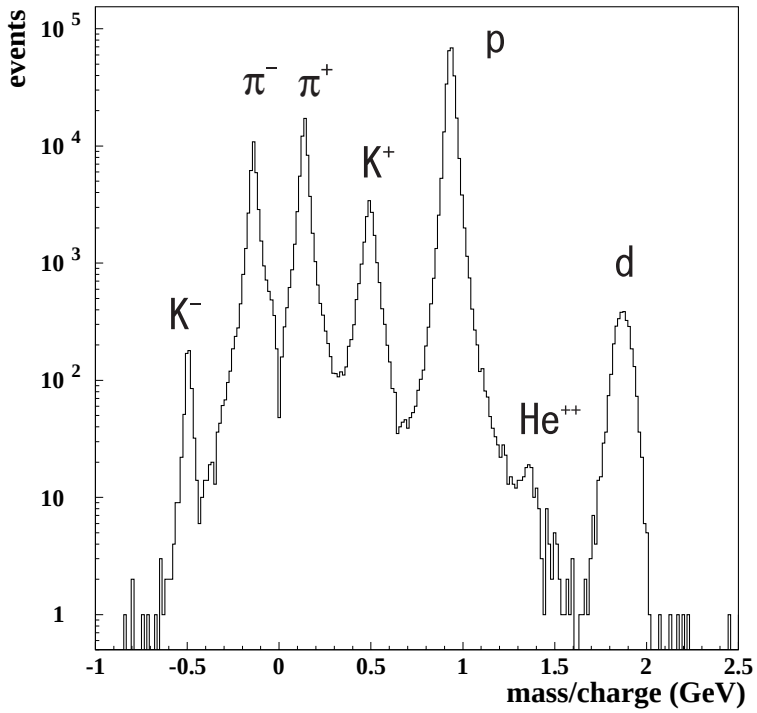

Figure 3.1: Reconstructed mass spectrum which passed the decay-in-flight selections. See the text for the detailed explanation.

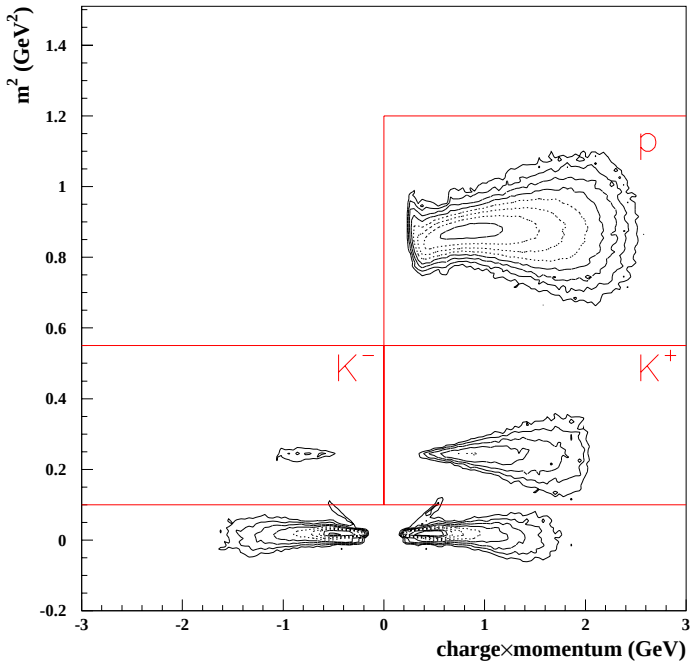

Figure 3.2: Two-dimensional scatter plot of the measured events as a function of reconstructed mass (m^2) versus charge $*$ momentum. The PID cut points are shown in the solid lines. Note that z-axis is drawn in log scale.

Table 3.3: Cut summary of KKp CUT

Cuts	Examined	Passed	Rejection
NTRK2	43690147	2073488	21.1
K^-PID	2073488	77085	26.8
K^+PID	77085	15589	4.94
p PID	15589	1016	15.3
DIF(K^-)	1016	908	1.118
DIF(K^+)	908	798	1.137
DIF(proton)	798	721	1.106

Table 3.4: Cut summary of KK CUT

Cuts	Examined	Passed	Rejection
NTRK2	43690147	2073488	21.1
K^-PID	2073488	77085	26.8
K^+PID	77085	15589	4.944
DIF(K^-)	15589	13498	1.154
DIF(K^+)	13498	12101	1.115
.not.(KKP cut)	12101	11380	1.063

Table 3.5: Cut summary of K^-P CUT

Cuts	Examined	Passed	Rejection
NTRK2	43690147	2073488	21.1
K^-PID	2073488	77085	26.898
p PID	77085	17008	4.532
DIF(K^-)	17008	13343	1.274
DIF(proton)	13343	12362	1.079
.not.(KKP cut)	12362	11641	1.061

Table 3.6: Cut summary of K^+P CUT

Cuts	Examined	Passed	Rejection
NTRK2	43690147	2073488	21.1
K^+PID	2073488	202897	10.219
p PID	202897	96092	2.111
DIF(K^-)	96092	76311	1.259
DIF(proton)	76311	70450	1.083
.not.(KKP cut)	70450	69729	1.010

3.3.3 The vertex cut

The distribution of the two-track vertex along with the z-coordinate after the track selection cuts (KKP or KK cut) are shown in Fig. 3.3. The events from reactions at the LH_2 target were clearly separated from the events from reactions at the start counter. There were small amount of background events at the vacuum windows at z=-900 and -1010 mm. A cut on the z-vertex ($-1000 < z < -910$ mm) was applied to select events from the LH_2 target. The right-handside of Fig. 3.3 shows the two-dimensional scatter plot of the events as a function of the x-vertex versus z-vertex. There were events coming from where the target holder was located ($z \sim -980$ and $x \sim -18$ mm). These events were rejected by the cut which was defined as $z < -960$ and $x < -15$ mm.

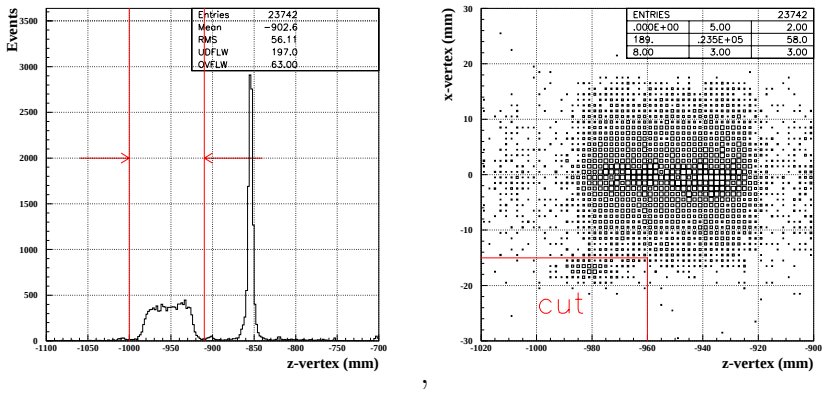

Figure 3.3: Right-hand side: two dimensional scatter plot of the two-track vertex along the z-vertex which passed the KK or KKp cuts. Left-hand side: two dimensional scatter plot of the x-vertex versus the z-vertex.

3.3.4 Selection for valid Tagger hit

The energy values of incident photons were obtained by analyzing the tagger signals. There are events in which non-valid tagger hit (ntag=0, ntag stands for number of valid tagger hits) was found although the tagger signal was required in the trigger condition. Figure. 3.4 shows the number of reconstructed tagger hits for the events which have passed the track selection cuts and the vertex cuts. There were two reasons for non-valid tagger hit.

The first one was due to an inefficiency of hit reconstruction which originated from inefficiency of the plastic scintillation counter. We required that all counters (the SSD and plastic scintillators) must provided a valid signal even where two scintillators are overlapped. On the other hand, the signal for the DAQ trigger was generated by a simple OR logic of ten scintillation counters in one layer, and the overlaps of the scintillator were not taken into account. This inefficiency of hit reconstruction was corrected afterwards (Section A).

The second reason of non-valid tagger hit was that the events with lower photon energies which was out of the tagger acceptance (1.5< E_γ <2.9 GeV). But they could make background hits in the tagger due to electro-magnetic shower at the vacuum pipe of the accelerator in the storage ring. However, the production threshold for K^+K^- ($E_\gamma = 1.507$ GeV) was above the

lowest limit of the acceptance. Only a contamination from π mesons in $K^{\pm}$ PID selection could make this background. But, the reconstructed mass distributions for $K^{\pm}$ with ntag=0 were quite similar to those in ntag$\neq$ 0 events. Therefore, the background from low energy photons were negligibly small.

To determine the incident photon energy , the number of valid tagger hit was required to be greater than 0 (ntag>0).

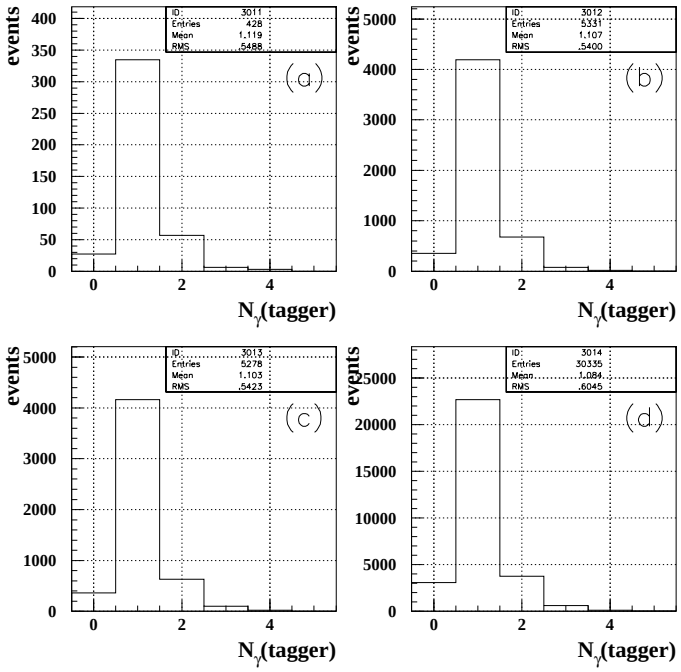

Figure 3.4: Distribution of the number of reconstructed tagger hits for the events which passed the track selection cuts and the vertex cuts. (a) KKp mode (b) KK mode (c) $K^{-}p$ mode (d) $K^{+}p$ mode.

3.3.5 E_γ selection

When the number of the tagger hits was more than one (ntag>1), a special treatment was applied to select one of the tagger hits by assuming the reaction $\gamma + p \rightarrow K^{+}K^{-}p$ on proton at rest. Most of the second tagger hits were originated from off-timing accidental hits in SSD by real electrons scattered by the interaction with the laser photon. These accidental hits should not have correlation with the tracks found in the spectrometer because the reaction took place with different photon.

Requirement of energy-momentum conservation gives an analytic form of the photon energy (E_γ^{KKP}) which is described by 4-momenta of two tracks (p_1 for particle 1 and p_2 for particle2); i.e. the relation

$$p_\gamma + p_p \;\; = \;\; p_1 + p_2,$$

$$\begin{aligned} p_\gamma &= (E_\gamma, 0, 0, E_\gamma), \\ p_p &= (M_p, 0, 0, 0) \end{aligned} \tag{3.2}$$

lead to

$$E_\gamma^{KKP} = \frac{M_3^2 - M_p^2 - M_{12}^2 + 2M_p E_{12}}{2(M_p - E_{12} + p_{12}^z)}, \tag{3.3}$$

where M_p is mass of the proton. M_{12}, E_{12} and p_{12}^z are mass, energy and the z component of momentum vector of the system of particle 1 and particle 2 respectively. The combination of particles 1 and 2 are either K^+K^- or $K^\pm p$. The index 3 represents p for K^+K^- mode and $K^\mp$ for $K^\pm p$ modes. There was a good correspondence between the calculated photon energy E_γ^{KKP} and E_γ measured by the tagger indicating the validity of selection of tagger hit. Figure 3.5(a) shows an accuracy of E_γ measurement was estimated using ntag=1 events. The accuracy was about 16 MeV which is smaller than the average difference of two possible photon energies measured by the tagger (∼70 MeV, see Fig. 3.6).

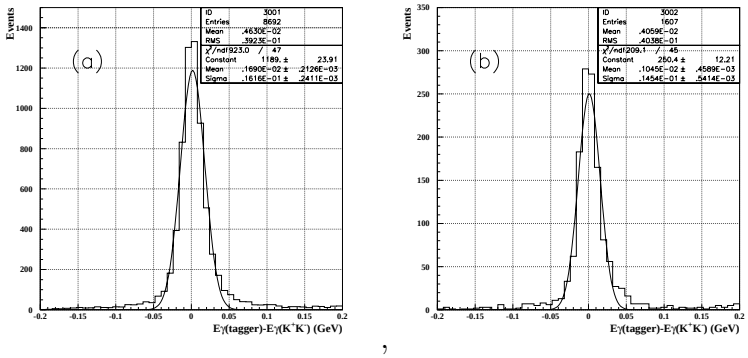

Figure 3.5: Difference of the incident-photon energies measured by the tagger and K^+K^- pair in the $p(\gamma, K^+K^-)p$ reaction from proton at rest. The KK or K^-p selection cut, the vertex cut were required. (a) Events with single tagger hit (ntag=1) (b) event with multi-tagger hits (ntag>1)

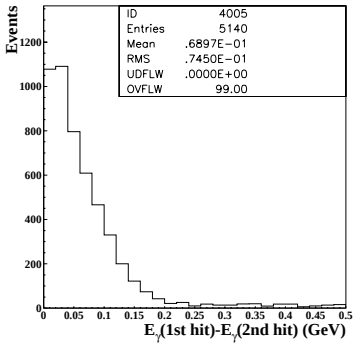

Figure 3.6: Difference of possible photon energies measured by the tagger when there are two hits (ntag=2). The KK or K^-p selection cut, the vertex cut and double tagger hit (ntag=2) were required.

A tagger hit closest to the E_γ^{KKP} was selected as the energy value of the incident photon when the number of tagger hit was greater than 1. Events with wrong choice of the tagger hit were removed by the cut on the missing mass distribution. The details of the missing mass cut is described in the next section.

3.3.6 Missing mass cut

After determining E_γ, the events from the reaction $\gamma + p \to K^+K^-p$ was identified with a cut on the missing mass distribution for the $(\gamma, K^+K^-)X$ process ($\equiv MM(\gamma, K^+K^-)$) in KKP mode and KK mode, and of the $(\gamma, K^\pm p)X$ process ($\equiv MM(\gamma, K^\pm p)$) in the $K^\pm P$ mode.

The missing mass distribution for the $(\gamma, K^+K^-)X$ is shown in Fig. 3.7(a) for KKP mode, and (b) for KK mode. A sharp peak at the proton mass was observed in the spectrum. there is essentially no background in the spectrum. This indicates majority of the events was come from the event with the K^+K^-p final state although a small bump is seen around 1.2 GeV which was a background from the non-K^+K^-p final state associated with a pion as discussed below. The missing mass resolution for the missing proton was found to be 10 MeV.

The missing mass distribution for the $(\gamma, K^-p)X$ reaction is shown in Fig. 3.7(c) for the K^-P mode. Similarly, the missing mass distribution for the $(\gamma, K^+p)X$ reaction is shown in Fig. 3.7(d) for the K^+P mode. A clear peak at K meson mass was identified in each plot. The missing mass resolution for missing the K meson was about 10 MeV.

A small bump around the MM(γ, K^+K^-) ~1.2 GeV in Fig. 3.7(a),(b) and a bump around MM(γ, K^-p) ~0.75 GeV in Fig. 3.7(c) were likely to be due to an additional pion (π^0 or $\pi^\pm$) in the final state which was missed in our detectors. Fig. 3.8(a) shows a missing mass square for the $(\gamma, K^+K^-p)X$ reaction in the KKp mode. There is an small peak around pion mass square m_π^2 besides a prominent peak at 0. GeV^2 which corresponds to the K^+K^-p final state. Correlations with other missing mass spectra ($MM(\gamma, K^+K^-)$,$MM(\gamma, K^-p)$ and $MM(\gamma, K^+p)$) are shown in Fig. 3.8(b),(c),(d). The red lines in these plots indicate the location of the π^0 mass square. These plot indicates that events associated with additional π^0 made the peak around the $MM(\gamma, K^+K^-)$ ~1.2 GeV and $MM(\gamma, K^{-(+)}p)$ ~0.75 GeV. Although there was no direct way to tag the additional pion in the K^+K^- and the $K^\pm P$ modes since the kinematics of the system was not determined by the measurement of two tracks, the bumps around the $MM(\gamma, K^+K^-) \sim 1.2$ GeV in Fig. 3.7(a),(b) and the $MM(\gamma, K^-p) \sim 0.75$ GeV Fig. 3.7(c) were likely to be the $K^+K^-p\pi^0$ (or $K^+K^-n\pi^+$, $K^+K^0p\pi^-$) final state.

In the K^+P mode, there were contribution from production of hyperons which could be the non-K^+K^-p final state. Figure. 3.9(a),(b),(c),(d) shows a missing mass spectrum for the $(\gamma, K^+)X$ reaction. There were clear signatures of the production of the hyperons ($\Lambda, \Sigma^0, \Sigma(1385), \Lambda(1405)$ and $\Lambda(1520)$) in plot (d). Except for the $\Lambda(1520)$ photoproduction, the final state of these hyperon production reaction are not allowed to be the K^+K^-p. For example, the following reactions allows to contain K^+p in the final state [54]:

$$\gamma + p \to K^+ + \Lambda \to K^+ + p + \pi^- \tag{3.4}$$
$$\gamma + p \to K^+ + \Sigma^0 \to K^+ + \Lambda + \gamma \to K^+ + p + \pi^- + \gamma \tag{3.5}$$
$$\gamma + p \to K^+ + \Sigma(1385) \to K^+ + \Lambda + \pi^0 \to K^+ + p + \pi^- + \pi^0 \tag{3.6}$$
$$\gamma + p \to K^+ + \Sigma(1385) \to K^+ + \Sigma^0 + \pi^0 \to K^+ + p + \pi^- + \gamma + \pi^0 \tag{3.7}$$

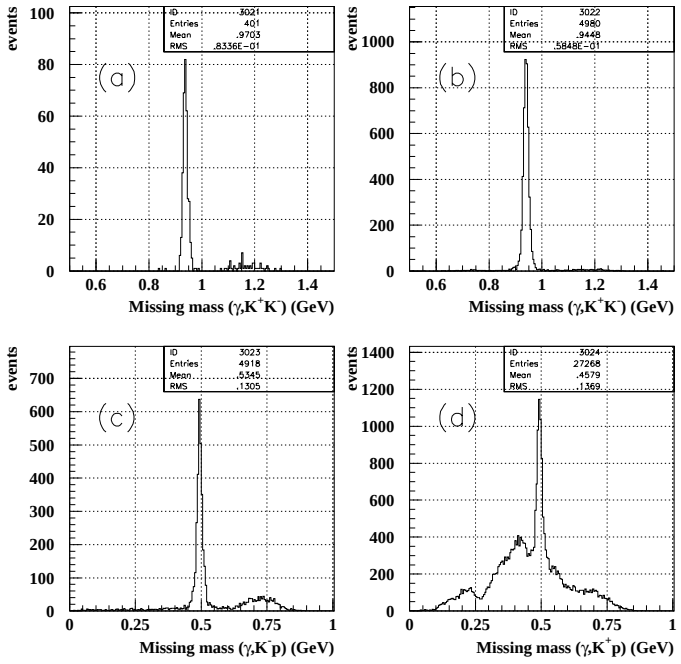

Figure 3.7: (a) Missing mass distribution for $(\gamma, K^+K^-)X$ reaction in the KKP mode (b) same for the KK mode. (c) Missing mass distribution for the $(\gamma, K^-p)X$ reaction in the K^-P mode (d) Missing mass distribution for the $(\gamma, K^+p)X$ reaction in the K^+p mode. In all the plots, the track selection cuts, the vertex cuts and valid tagger hits were required.

$$\gamma + p \quad \rightarrow K^+ + \Sigma(1385) \rightarrow K^+ + \Sigma^+ + \pi^- \rightarrow K^+ + p + \pi^0 + \pi^- \tag{3.8}$$
$$\gamma + p \quad \rightarrow K^+ + \Lambda(1405) \rightarrow K^+ + \Sigma^0 + \pi^0 \rightarrow K^+ + p + \pi^- + \gamma + \pi^0 \tag{3.9}$$
$$\gamma + p \quad \rightarrow K^+ + \Lambda(1405) \rightarrow K^+ + \Sigma^+ + \pi^- \rightarrow K^+ + p + \pi^0 + \pi^- \tag{3.10}$$
$$\gamma + p \quad \rightarrow K^+ + \Lambda(1520) \rightarrow K^+ + \Sigma^0 + \pi^0 \rightarrow K^+ + p + \pi^- + \gamma + \pi^0 \tag{3.11}$$
$$\gamma + p \quad \rightarrow K^+ + \Lambda(1520) \rightarrow K^+ + \Sigma^+ + \pi^- \rightarrow K^+ + p + \pi^0 + \pi^- \tag{3.12}$$

In order to select the K^+K^-p final state, a cut on the missing mass spectrum $0.908 < MM(\gamma, K^+K^-) < 0.968$ GeV was applied for the KKP and KK reconstruction modes, and a cut on the missing mass $0.464 < MM(\gamma, K^{-(+)}p) < 0.524$ GeV was applied for the K^-p (K^+p) modes. The cut points corresponded to 3σ of the missing mass resolution.

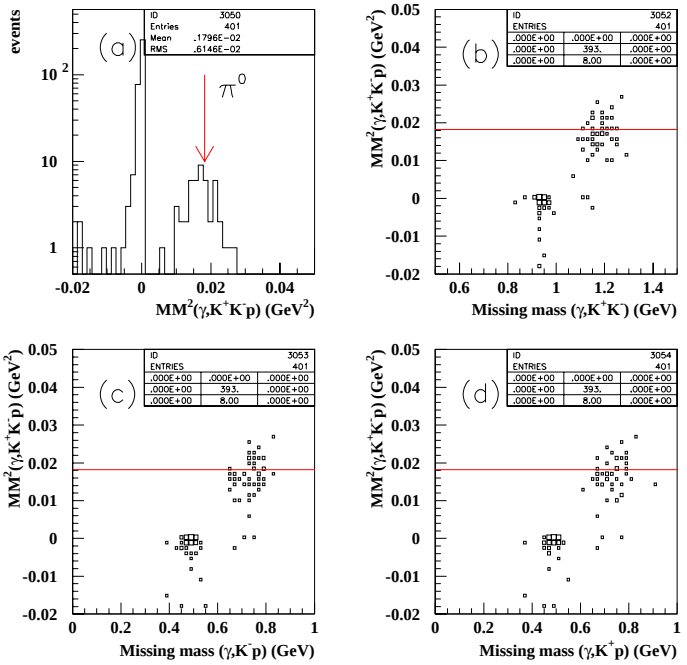

Figure 3.8: The missing mass distributions in the KKP mode. (a) missing mass square for the $(\gamma, K^+K^-p)X$ reaction (b) correlation between the $MM^2(\gamma, K^+K^-p)$ and the $MM(\gamma, K^+K^-)$, (c) correlation between the $MM^2(\gamma, K^+K^-p)$ and the $MM(\gamma, K^-p)$, (d) correlation between the $MM^2(\gamma, K^+K^-p)$ and the $MM(\gamma, K^-p)$. In all the plots, the track selection cuts for KKp mode, the vertex cuts and valid tagger hits were required.

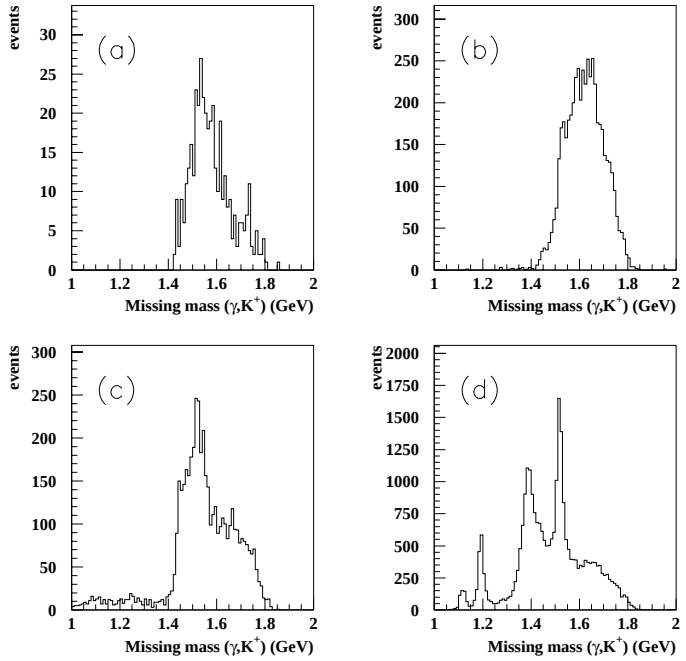

Figure 3.9: Missing mass distributions for the $(\gamma, K^+)X$ reaction in the KKP mode (a), in the KK mode (b). in K^-P mode (c), and the K^+p mode (d). In all the plots, the track selection cuts, the vertex cuts and valid tagger hits were required.

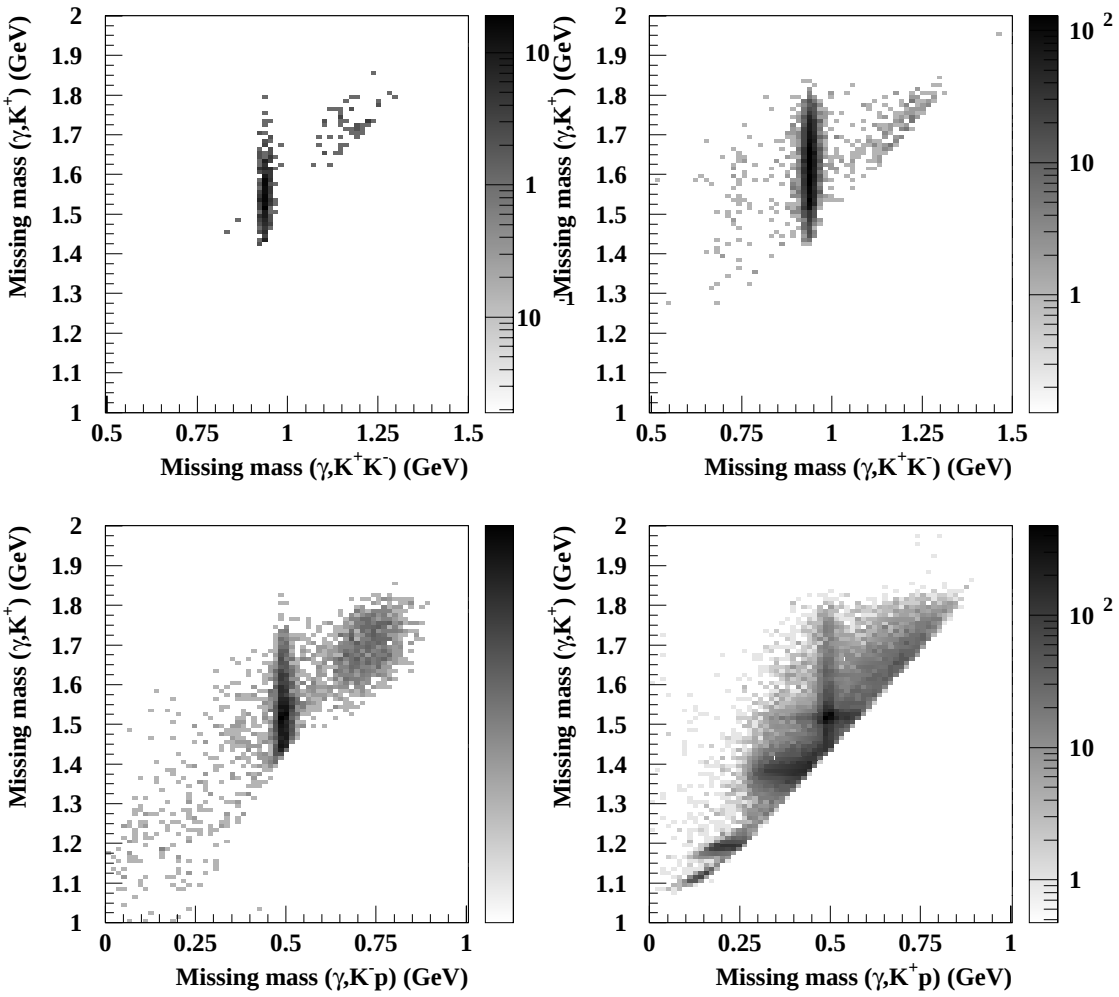

Figure 3.10: Missing mass distribution the $(\gamma, K^+)X$ reaction as a function of (a) missing mass for the $(\gamma, K^+K^-)X$ reaction in the KKP mode, (b) same for the KK mode. (c) missing mass for the $(\gamma, K^-p)X$ reaction in the K^-P mode and (d) missing mass for the $(\gamma, K^+p)X$ reaction in the K^+P mode. In all the plots, the track selection cuts, the vertex cuts and valid tagger hits were required.

3.3.7 KK invariant mass cut

The events of ϕ-meson photoproduction were identified using the K^+K^- invariant mass distribution. In the K^-P and K^+P mode, the momentum vector of the missing kaon was calculated by assuming the K^+K^-p final state. Figure. 3.11 shows the K^+K^- invariant mass distribution for each mode. The events of ϕ-meson photoproduction were clearly identified as a sharp peak at the mass of ϕ-meson. There was a small amount of backgrounds in the sample of the KKP and the KK modes. On the other hand, a significant amount of backgrounds besides the ϕ peak was observed in these spectra in the K^-P and K^+P modes.

It was found that the production of $\Lambda(1520)$ played an important role near the ϕ-meson production threshold where the acceptance of the $K^{\pm}P$ mode was large. $\Lambda(1520)$ decays into K^-p with a branching fraction of 23% [54], resulting in the K^+K^- final state. The Dalitz plot for the K^+K^-p final state is shown in Fig. 3.12. The locus corresponds to the $\Lambda(1520)$ mass was clearly visible in Fig. 3.12(c) and (d). A projection of these distributions onto the K^-p invariant mass is shown in Fig. 3.13. A peak at the mass of $\Lambda(1520)$ was clearly observed. In Fig. 3.12, we recognized that there were obviously other types of the continuum backgrounds under the ϕ meson peak. However, no strong signatures from other hyperon resonances (e.g. $\Lambda(1600)$, $\Lambda(1670)$ etc) were observed in the K^-p mass spectrum. The origin of this background could be a non-resonant K^+K^-p production and/or the $f_0(980)$ photoproduction. The mass of the f_0 is below the two-kaon threshold but because of large width ~ 60 MeV, the tail of the resonance can be the background events in the present analysis [26]. These backgrounds were subtracted in the data analysis. The procedure of the background subtraction is described in Section 3.6.

In order to determine the cut points on the K^+K^- invariant mass to select the events from ϕ-photoproduction, the K^+K^- invariant mass resolution for ϕ meson was checked by using a Gaussian-convoluted Breit-Wigner function, $N_{BW}(m,\sigma)$, and a phenomenological background shape $N_{BG}^{phen}(a,b,m)$ [55]:

$$N_{BW}(m,\sigma) = \frac{1}{\sqrt{2\pi\sigma^2}}\int_{2m_K}^{\infty} dm' e^{\frac{-(m'-m)^2}{2\sigma^2}} \frac{\Gamma/2\pi}{(m'-m_\phi)^2+(\Gamma/2)^2} \tag{3.13}$$

$$N_{BG}^{phen}(a,b,m) = a\sqrt{m^2-(2m_K)^2}+b(m^2-(2m_K)^2), \tag{3.14}$$

where m is the KK invariant mass, a and b are parameters, m_K is the K meson mass (0.493677 GeV), m_ϕ is the mass of ϕ meson (1.019456 GeV) and Γ is a full width of the ϕ meson decay (4.26 MeV)[54]. The invariant mass distribution was fitted with following parameterization:

$$N_{BW}(m) = P_1 N_{BW}(m,\sigma=P_2) + N_{BG}^{phen}(a=P_3,b=P_4,m), \tag{3.15}$$

where P_1, P_2, P_3 and P_4 are fitting parameters. The parameter P_2 represents a resolution (σ) of track reconstruction. The results of the fitting are shown in Fig. 3.14. The K^+K^- invariant mass resolution was found to be 1.82 $\pm$ 0.42 MeV (KKp mode), 1.40 $\pm$ 0.03 MeV (K^+K^- mode), 2.99 $\pm$ 0.18 MeV (K^-p mode), 2.42 $\pm$ 0.31 MeV (K^+p mode). They are compatible with the ϕ meson natural width ($\sigma = \Gamma/2.35 = 1.81$ MeV). The cut points on the K^+K^- invariant mass was set to $1.009 < M(K^+K^-) < 1.029$ GeV which corresponds to about 90 % acceptance for the ϕ events.

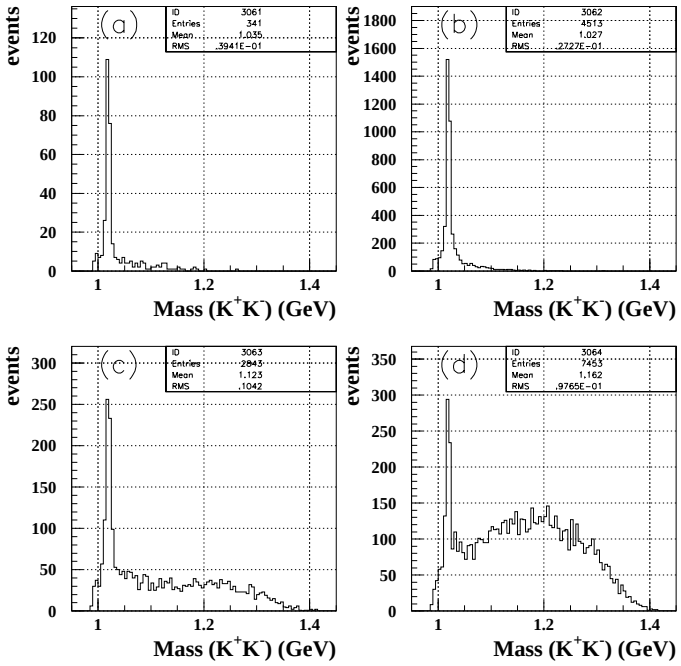

Figure 3.11: The K^+K^- invariant mass distribution in (a) the KKP mode , (b) the KK mode, (c) the K^-P mode, and (d) the K^+P mode. The track selection cuts, vertex cuts, tagger cut and missing mass cut were required.

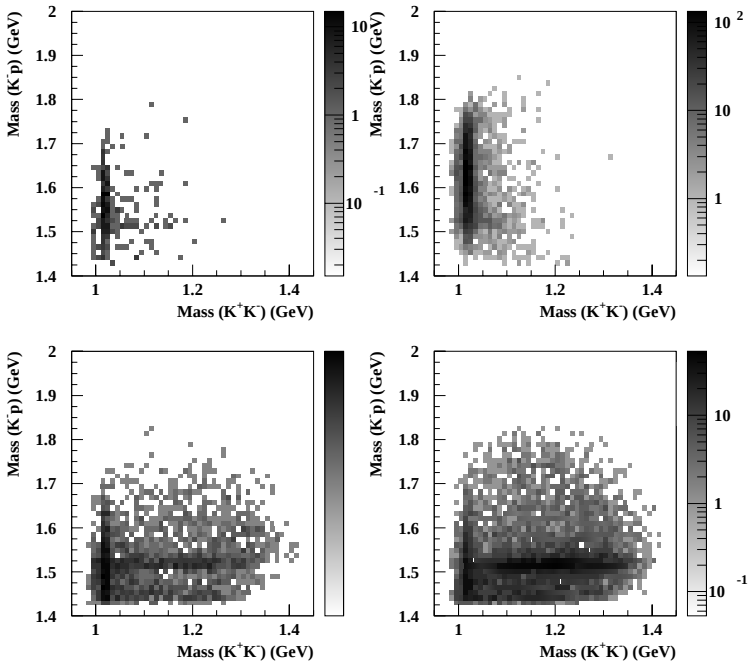

Figure 3.12: The Dalitz plot, K^-p invariant mass versus K^+K^- invariant mass in (a) the KKP mode, (b) the KK mode, (c) K^-P mode, and (d) K^+P mode. The track selection cuts, vertex cuts, tagger cut and missing mass cut were required. Note that z-axis (perpendicular to this paper) is in log scale.

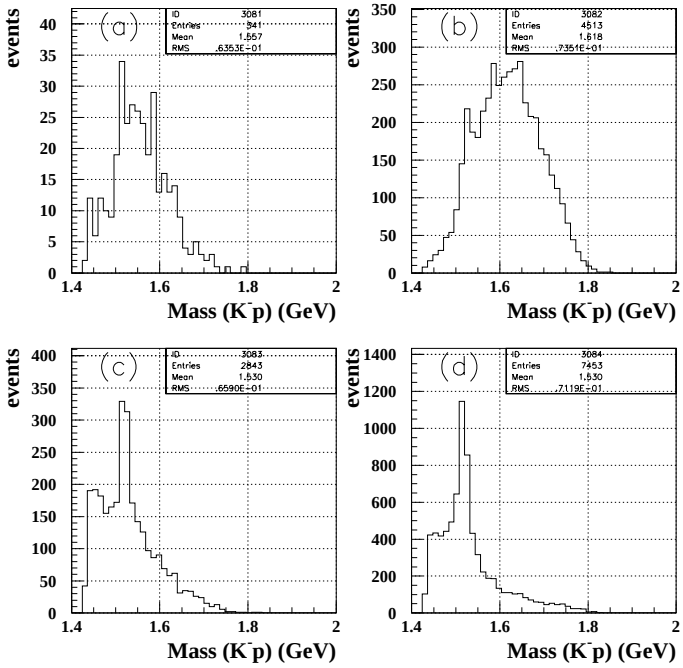

Figure 3.13: The K^-p invariant mass distribution in (a) the KKp mode , (b) KK mode, (c) K^-p mode, and (d) K^+p mode. The track selection cuts, vertex cuts, tagger cut and missing mass cut were required.

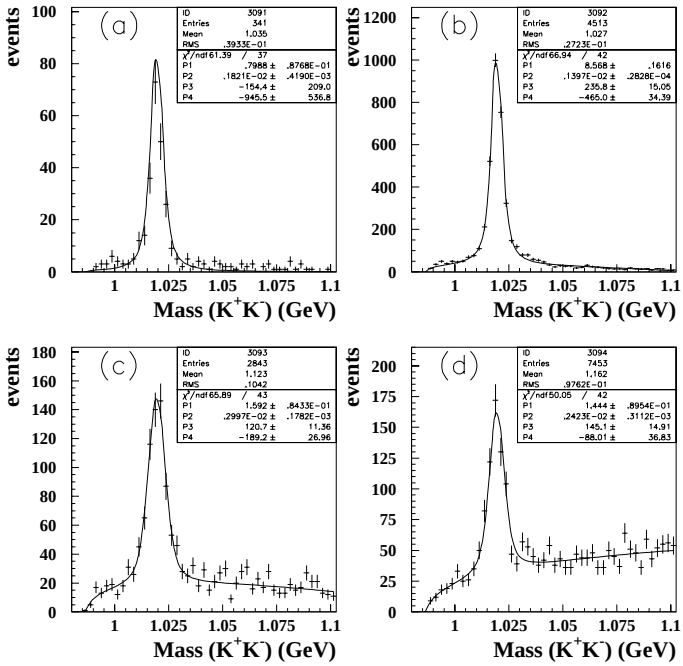

Figure 3.14: The K^+K^- invariant mass distribution and the fit by Eq 3.15 in (a) the KKP mode, (b) the KK mode, (c) the K^-p mode, and (d) the K^+p mode. The solid curves are the results of the fitting using Eq. 3.15. The track selection cuts, vertex cuts, tagger cut and missing mass cut were required.

3.3.8 Summary of ϕ selection cuts

The selection cuts for ϕ photo-production events, referred as the ϕ selection cuts, are defined as a combination of vertex cut and valid tagger cut and missing mass cut and the invariant mass cut. The number of events before and after the ϕ selection cuts are summarized in Table. 3.7,3.8,3.9 and 3.10.

Table 3.7: Summary of ϕ selection cuts for KKp mode

Cuts	Description	Examined	Passed	Rejection
Z-Vertex	-1000<z-vertex<-910 mm	721	432	1.668
(X,Z)-Vertex	.not.(z-vertex<-960 and x-vertex<-15 mm)	432	428	1.009
NTAG	ntag > 0	428	404	1.059
MISS	$0.908 < MM(\gamma, K^+K-) < 0.968$ GeV	404	341	1.184
KKMASS	1.009 <mass(K^+K^-) < 1.029 GeV	341	222	1.536

Table 3.8: Summary of ϕ selection cuts for K^+K^- mode

Cuts	Description	Examined	Passed	Rejection
Z-Vertex	-1000<z-vertex<-910 mm	10380	5500	1.887
(X,Z)-Vertex	.not.(z-vertex<-960 and x-vertex<-15 mm)	5500	5331	1.031
NTAG	ntag > 0	5331	4980	1.070
MISS	$0.908 < MM(\gamma, K^+K-) < 0.968$ GeV	4980	4513	1.103
KKMASS	1.009 <mass(K^+K^-) < 1.029 GeV	4513	3180	1.419

Table 3.9: Summary of ϕ selection cuts for K^-p mode

Cuts	Description	Examined	Passed	Rejection
Z-Vertex	-1000<z-vertex<-910 mm	11641	5396	2.157
(X,Z)-Vertex	.not.(z-vertex<-960 and x-vertex<-15 mm)	5396	5278	1.022
NTAG	ntag > 0	5278	4918	1.073
MISS	$0.908 < MM(\gamma, K^+K-) < 0.968$ GeV	4918	2843	1.729
KKMASS	1.009 <mass(K^+K^-) < 1.029 GeV	2843	694	4.096

Table 3.10: Summary of ϕ selection cuts for K^+p mode

Cuts	Description	Examined	Passed	Rejection
Z-Vertex	-1000<z-vertex<-910 mm	69729	31362	2.223
(X,Z)-Vertex	.not.(z-vertex<-960 and x-vertex<-15 mm)	31362	30335	1.033
NTAG	ntag > 0	30335	27268	1.112
MISS	$0.908 < MM(\gamma, K^+K-) < 0.968$ GeV	27268	7453	3.658
KKMASS	1.009 <mass(K^+K^-) < 1.029 GeV	7453	743	10.030

3.4 The kinematical fit

The K^+K^-p sample after the event selections explained in Section 3.3 were obtained in the measurements of momenta for at least two of three charged particles out of the final state in the reaction $\gamma p \to K^+K^-p$ with a known photon energy. For the elastic ϕ photoproduction from protons at rest, kinematics variables are over-determined by the measurement. However, no kinematical constraint for the energy and momentum conservations was taken into account in the reconstruction of individual tracks. A kinematical fit (1C) [56] was applied to reconstruct 4-momenta of K^+K^-p by requiring the energy and momentum conservations.

The main advantage of applying the kinematical fit is that the energy and momentum conservations give the constraint on the kinematical variables, such as momenta and angles, to be within a physical region. The measured variables before the kinematical fit lie in unphysical region due to the finite resolution.

The momentum and angular resolution of the reconstructed tracks and the beam energy resolution were provided to the fitting process as inputs for the covariant matrix. The beam energy resolution was taken from the measurement [46]. The momentum and the angular resolution of the reconstructed tracks were obtained from the Monte Carlo simulation. The resolutions used in the kinematical fit are summarized in Table 3.11.

Table 3.11: E_γ, momentum and angular resolution for kinematical fit

Variable	Resolution (KKP or KK mode)	Resolution (KP mode)
$\sigma(E_\gamma)(MeV)$	15.0	15.0
$\sigma^2(p)$ (GeV^2)	$0.003p^2 + (0.004(1 + (M/p)^2)^2$	$0.003p^2 + (0.004(1 + (M/p)^2)^2$
$\sigma(\theta_x)$ (rad)	0.0004	0.0007
$\sigma(\theta_y)$ (rad)	0.0004	0.0007

Fig. 3.15 (a) shows the beam energy resolution defined as a difference between a measured photon energy and an input photon energy ($E_{\gamma(meas)} - E_{\gamma(input)}$) in Monte Carlo simulation before the kinematical fit. Fig. 3.15 (b) shows the one after the fitting. The beam energy resolution resolution improved from 14 MeV to 7 MeV by the kinematical fitting. There was little improvement of the resolution by inclusion of an additional constraint for the K^+K^- invariant mass to be ϕ-meson mass (2C fit) since the K^+K^- invariant mass resolution for the ϕ meson is compatible with the natural width of the ϕ-meson as shown in Section 3.3.

The goodness of the kinematical fitting were checked by the probability of χ^2 (prob(χ^2)). The prob(χ^2) distribution in Monte Carlo data are shown in Fig. 3.16. No selection on the missing mass was made in the plots on left-hand side, and the plots on right-hand side were obtained with the missing mass cut. No strong structure was seen in the prob(χ^2) distributions in Monte Carlo simulation although the distributions for the $K^\pm P$ modes were not completely flat.

The prob(χ^2) distributions in real data are shown in Fig. 3.17. In real data, there was a peak near prob(χ^2)=0 when the missing mass cut was not applied. These events were attributed to either (1) mismeasurement of momentum vector, photon energy or (2) the backgrounds from non-K^+K^-p final state, for example Eq. 3.4-3.12.

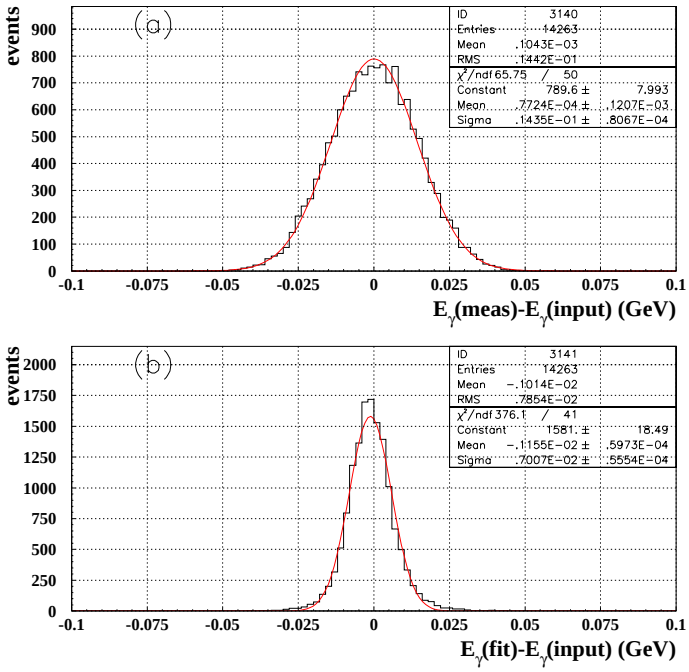

Figure 3.15: The beam energy resolution in Monte Carlo simulation (a) before the kinematical fitting (b) after the kinematical fitting. The solid line indicates a fit by Gaussian function.

No selection on the prob(χ^2) was applied since (1) the prob(χ^2) distribution was not completely flat due to an incomplete knowledge of resolutions and (2) the missing mass cut was already made to reject the low prob(χ^2) events. The momentum vectors and the beam energy after the kinematical fit were used to calculate the kinematical observables in the measurements of the differential cross section and the decay angular distribution.

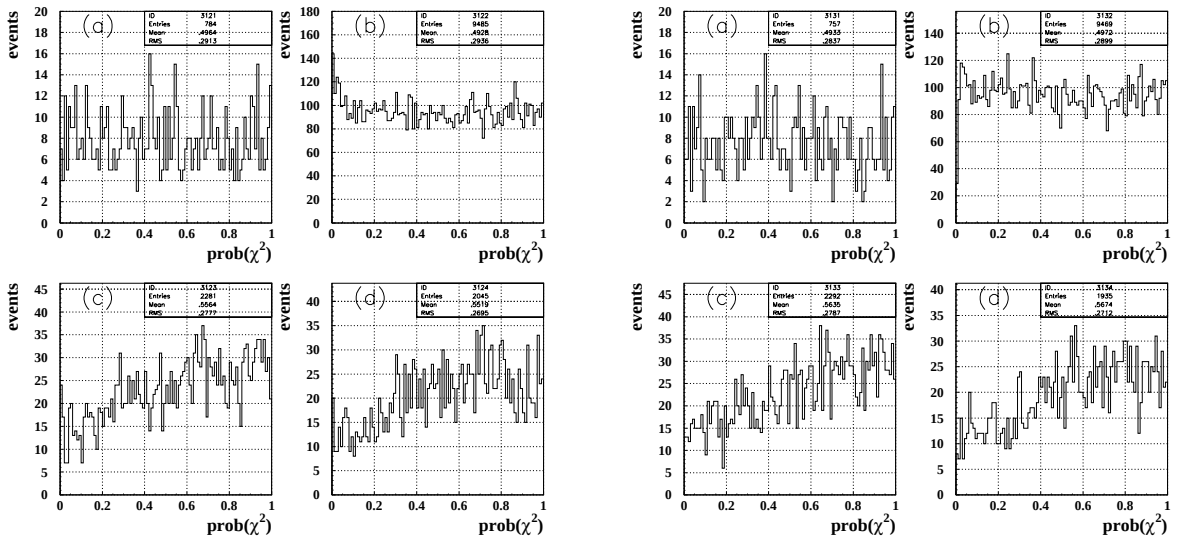

Figure 3.16: prob(χ^2) distribution for the kinematical fit in Monte Carlo data without the missing mass cut (left) and with the missing mass cut (right) in (a) the KKP mode, (b) the KK mode, (c) the K^-P mode, and (d) the K^+P mode.

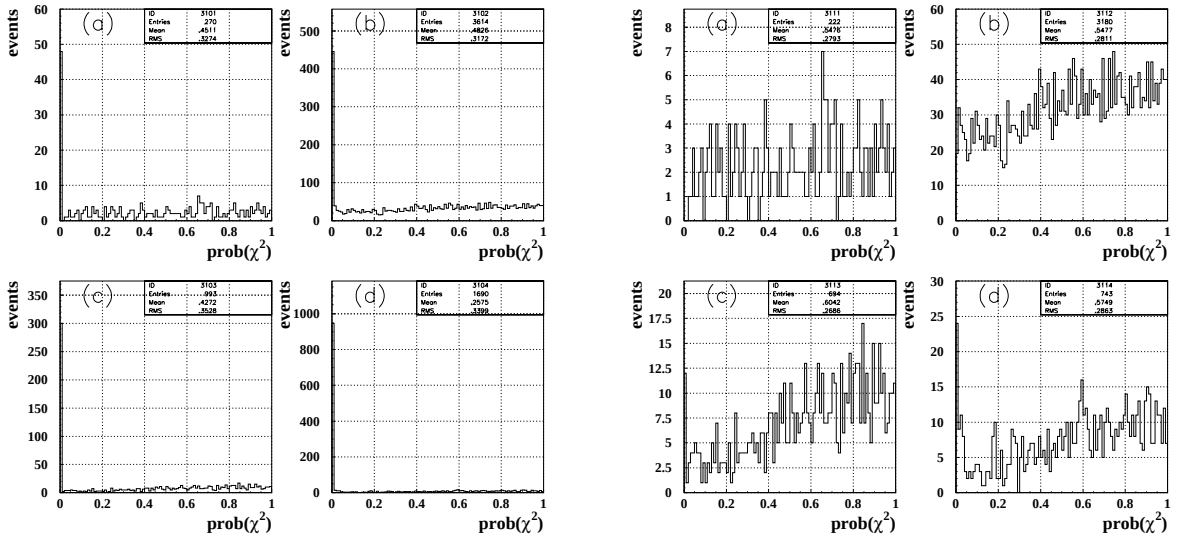

Figure 3.17: prob(χ^2) distribution for the kinematical fit in real data without the missing mass cut (left) and with the missing mass cut (right) in (a) the KKP mode, (b) the KK mode, (c) the K^-P mode, and (d) the K^+P mode

3.5 The kinematical coverage

Figure 3.18 shows the population of the events of the ϕ photoproduction events for each mode in the present data as a function of E_γ and $t + |t|_{min}$, where $|t|_{min}$ is the minimum momentum transfer allowed for ϕ photoproduction. The solid curves indicate kinematical boundary of the reaction assuming the nominal ϕ-meson mass although these limits are not exact in a sense that ϕ-meson has a finite decay width in reality. In fact, there were a few events outside of the solid line in Fig. 3.18, corresponding to the K^+K^- invariant mass which was slightly different from the nominal ϕ-meson mass. Note that the smearing due to resolutions were partly removed by the constraint in the kinematical fitting. In the data analysis, measured K^+K^- invariant mass after the kinematical fit was used to calculate momentum transfer t, $|t|_{min}$ and decay angles in the ϕ-meson rest frame.

There were differences in the population of the events between the KK mode and the $K^\pm P$ modes due to difference of acceptance; i.e. there were more K^+K^- events accepted in the higher E_γ where number of $K^\pm p$ events are smaller and vice versa. Combination of K^+K^- events and $K^\pm p$ events covered the full kinematical region at forward angles (small t).

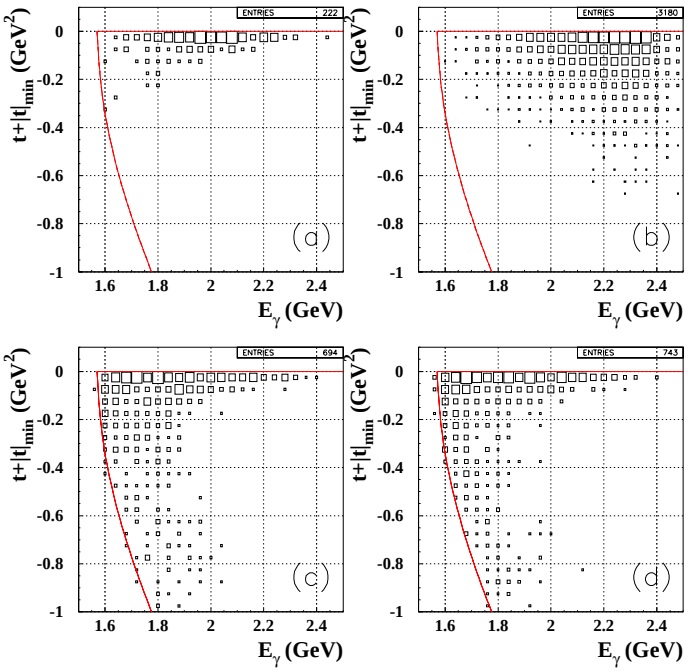

Figure 3.18: Population of ϕ events observed in real data as a function of the photon energy and the four momentum transfer in (a) the KKP mode, (b) the KK mode, (c) the K^-P mode, and (d) K^+P mode. All the ϕ selection cuts were required. No background subtraction was applied.

3.6 Background subtraction

The backgrounds were categorized into two types; the $\Lambda(1520)$ production and the non-resonant KKp backgrounds in which no signature of formation of the resonance was seen. Analysis of the backgrounds is described in this section.

The Monte Carlo simulation for the backgrounds was necessary in order to know the best way of background subtraction. The K^+K^- invariant mass distributions and the angular distributions for the backgrounds were studied for this purpose.

As for the $\Lambda(1520)$ background, there were two measurements of $\Lambda(1520)$ photoproduction at higher energies, [57] at 11 GeV and [58] at 2.8-4.8 GeV. These measurement showed an exponential decrease in the t-distribution by t-channel exchange of $K^*(892)$. However there is no measurement near production threshold, only a measurement of electro-production [59] is available. There is even less information on the non-resonant KKp background. Physical process of the non-resonant KKp background is unknown, and no experimental data near threshold has been published. It was difficult to build up a reliable Monte Carlo simulator for the background based on the existing database. Therefore, the backgrounds in real data were parameterized in the Monte Carlo simulation.

3.6.1 The Non-resonant KKp background

A Monte Carlo simulator for the non-resonant KKp background was obtained by a fit to the real data. At first, the Monte Carlo data for the K^+K^-p final state was generated according to the 3-body phase space distribution. Fig. 3.19 shows a phase space distribution in the Monte Carlo data in four different beam energies (a)$2.173 < E_\gamma < 2.373$ GeV, (b)$1.973 < E_\gamma < 2.173$ GeV, (c)$1.773 < E_\gamma < 1.973$ GeV and (d)$1.573 < E_\gamma < 1.773$ GeV. The phase space shrinks rapidly as the energy decreases. Discrimination of the ϕ-meson signal from the backgrounds become more difficult around the threshold.

In the first Monte Carlo data, the polar angle distributions ($\cos\theta^{CM}$) of K^+, K^- and proton in total center-of-mass system were set to be flat over all angles. The polar angle distributions of K^+ and proton in Monte Carlo data were compared with the real data for the events which survives all of the ϕ selection cuts, except for the invariant mass cut. In this comparison, a selection to the beam energy, $2.173 < E_\gamma < 2.373$ GeV, was applied to reduce an ambiguity of unknown energy dependence of the cross section for the backgrounds. The invariant mass cut was reversed to kill the signal from ϕ-meson, i.e $M(K^+K^-) < 1.009$ GeV or $1.029\text{GeV} < M(K^+K^-)$. A cut on K^-p invariant mass, $M(K^-p) < 1.500$ GeV or $1540\text{GeV} < M(K^-p)$, was applied to exclude the event from $\Lambda(1520)$. Note that mass and full width of $\Lambda(1520)$ are 1.5195 GeV and 15.6 MeV, respectively [54].

Figure 3.20 (a) represents the polar angle distributions for the K^+ accepted in the LEPS detector in Monte Carlo data, the real data behaves as Fig. 3.20 (b), where events in K^+K^-p mode, K^+K^- mode and $K^\pm p$ modes were combined. A ratio of real data to Monte Carlo data is shown in Fig. 3.20(c). The ratio showed a non-flat structure, indicating that angular distribution of the K^+ in the non-resonant K^+K^-p background was not flat, but forward peaked. The solid curve in Fig. 3.20(c) represents a fit to the ratio by 4th-order polynomial function.

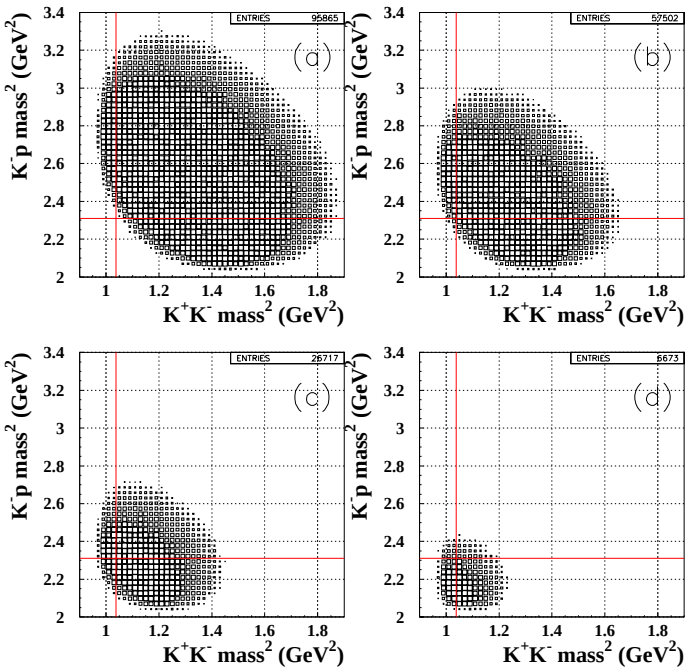

Figure 3.19: Phase space distributions for the three body reaction $\gamma + p \rightarrow K^+K^-p$ for (a) $2.173 < E_\gamma < 2.373$ GeV,(b) $1.973 < E_\gamma < 2.173$ GeV, (c)$1.773 < E_\gamma < 1.973$ GeV, (d)$1.573 < E_\gamma < 1.773$ GeV. The vertical and the horizontal lines indicates locations of mass of ϕ-meson and $\Lambda(1520)$, respectively.

Similarly, the angular distributions of the proton are shown in Fig. 3.21. A fitting by a 3rd order polynomial function was shown as the solid curve in Fig. 3.21(c).

Based on the polynomial functions obtained from the angular distribution of the K^+ and proton in real data, the non-resonant K^+K^-p events for the background were generated in the Monte Carlo simulation. The shape of the K^+K^- invariant mass distribution for the non-resonant KKp ($N_{BG}^{non-resontant}(m_{KK})$) were obtained for KKP, KK and $K^\pm P$ modes separately.

In order to check the validity of the Monte Carlo simulation for the non-resonant K^+K^-p background, a fit to the K^+K^- invariant mass distribution in real data was examined with following parameterization :

$$\begin{aligned} N_{K^-pmode}(m_{KK}) &= (P_1 N_{BW}(m_{KK}, \sigma_{K^-p}) + P_4 N_{BG,K^-pmode}^{non-resontant})(m_{KK}) \\ N_{K^+pmode}(m_{KK}) &= (P_2 N_{BW}(m_{KK}, \sigma_{K^+p}) + P_4 N_{BG,K^+p}^{non-resontant})(m_{KK}) \\ N_{KKmode}(m_{KK}) &= (P_3 N_{BW}(m_{KK}, \sigma_{K^+K^-}) + P_4 N_{BG,KKmode}^{non-resontant})(m_{KK}), \end{aligned} \tag{3.16}$$

where event samples for the KK mode, the K^+P mode and the K^-P mode were fitted simultaneously. $N_{BG}^{non-resontant}(m_{KK})$ is the simulated shape of the invariant mass, N_{BW}(Eq. 3.15) is the Gaussian convoluted Breit-Wigner distribution. The invariant mass resolution for ϕ signal was fixed to the measured values ($\sigma_{KK}, \sigma_{K^-P}, \sigma_{K^+P}$) which were described in Section

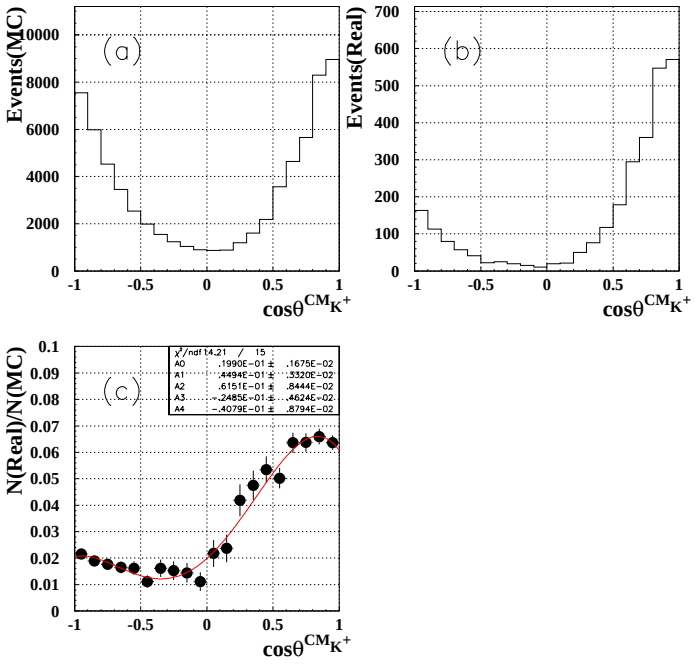

Figure 3.20: Polar angle distribution of the K^+ accepted by the LEPS detector for the background sample. (a) Monte Carlo data (phase space), (b) real data, (c) ratio of real data to Monte Carlo data.

3.3.7. Note that events in the KKP mode and the KK mode were combined (just referred as the KK mode from now). The results of the fitting as a function of beam energy are shown in Table 3.12 and Fig. 3.22. Results of the fit shows that general agreements between real data and Monte Carlo simulation for (1) the background shape and (2) a relative number of the background in different reconstruction modes. The simulated invariant mass distributions for the non-resonant KKp backgrounds, $N_{BG}^{non-resontant}(m_{KK})$, was used for the background subtraction.

Table 3.12: Fitting to the K^+K^- invariant mass for events with the $\Lambda(1520)$ exclusion cut.

E_γ(GeV)	1.573-1.773	1.773-1.973	1.973-2.173	2.173-2.373
P_1	0.741 ± 0.061	0.598 ± 0.053	0.366 ± 0.038	0.143 ± 0.024
P_2	0.903 ± 0.078	0.666 ± 0.067	0.496 ± 0.047	0.153 ± 0.026
P_3	0.120 ± 0.028	1.067 ± 0.073	3.480 ± 0.125	6.039 ± 0.1651
P_4	0.01163 ± 0.00067	0.01041 ± 0.00033	0.00801± 0.00021	0.00724 ± 0.00015
χ^2/ndf	64.77/30	149.9/56	135.0/74	143.5/100

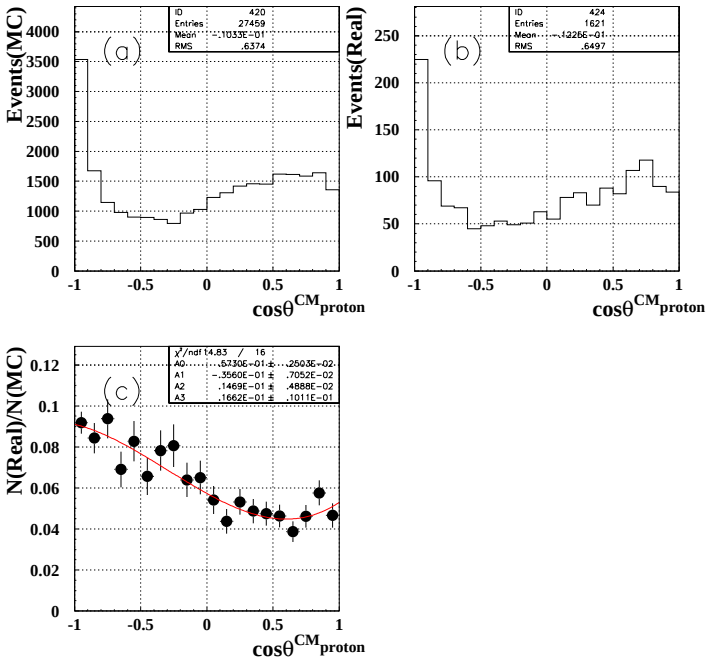

Figure 3.21: Polar angle distribution of the proton accepted by the LEPS detector for the background sample. (a) Monte Carlo data (phase space), (b) real data, (c) ratio of real data to Monte Carlo data.

3.6.2 The $\Lambda(1520)$ background

The background shape of the $\Lambda(1520)$ background in the K^+K^- invariant mass distribution was studied by the same Monte Carlo simulator as the one for the non-resonant KKp backgrounds. The K^-p invariant mass was limited to $1.500 < M(K^-p) < 1.540$ GeV in the simulation to match kinematical conditions for $\Lambda(1520)$ In real data, the data sample which contains $\Lambda(1520)$ events were selected by applying a cut on the K^-p invariant mass distribution, $1.500 < M(K^-p) < 1.540$ GeV. The ϕ-meson exclusion cut was also applied. Note that the continuous non-resonant KKp backgrounds were also present in the same sample even after the cut $1.500 < M(K^-p) < 1.540$ GeV. A simultaneous fit to the K^+K^- invariant distribution with Eq. 3.16 failed to represent the observed distribution. This implies that the non-resonant KKp simulator worked imperfectly as a $\Lambda(1520)$ simulator. However, a fit to an individual spectrum with the following parameterization :

$$N_(m_{KK}) = (P_1 N_{BW}(m_{KK}, \sigma) + P_2 N_{BG}^{non-resontant})(m_{KK}) \tag{3.17}$$

succeed to reproduce the experimental data, where the relative numbers of events in the KK and the $K^{\pm}p$ modes were not required to be consistent with the Monte Carlo data. The results of fitting are shown in Fig. 3.23.

The results of the fit indicated that at least the shape of the spectrum for the $\Lambda(1520)$ backgrounds was well represented by the non-resonant KKp simulator. The difference of angular distribution between the non-resonant KKp background and the $\Lambda(1520)$ background

maybe the reason of the failure to reproduce the relative numbers in KK and $K^{\pm}P$ modes. However, the systematic error due to wrong angular dependence would not be large since the background subtraction was made in each sub-sample of angles, E_γ and $t + |t|_{min}$, the Therefore, the non-resonant KKp simulator was also used for the $\Lambda(1520)$ background. A procedure of the background subtraction is described in next section.

3.6.3 Background subtraction

It was clear that a simple background subtraction by using sidebands in the K^+K^- invariant mass using a linear interpolation between sidebands failed at lower energies as indicated in Fig. 3.22 and 3.23 where the shape of the backgrounds had an maximum around ϕ-meson signal. Therefore, the background shape simulated by the Monte Carlo simulation had to be used for the background subtraction. Number of background counts in the ϕ signal region was deduced by scaling the simulated background shape to fit the real data. The scaling factor was obtained from the sidebands in the K^+K^- invariant mass in both real data and Monte Carlo data. The sidebands were defined as $0.989 < M(K^+K^-) < 1.009$ GeV (sideA) and $1.039 < M(K^+K^-)$ (sideB). The signal region was defined as $1.009 < M(K^+K^-) < 1.029$ GeV (see Section 3.3). Number of background counts $N_{signal,BG}$ in signal region was given by:

$$N^{real}_{signal,BG} = \alpha(N^{real}_{sideA,BG} + N^{real}_{sideB,BG}) \tag{3.18}$$

$$\alpha = \frac{N^{MC}_{signal,BG}}{N^{MC}_{sideA,BG} + N^{MC}_{sideB,BG}}, \tag{3.19}$$

where $N_{sideA,BG}$ and $N_{sideB,BG}$ are number of background in sideA and sideB, respectively.

In real data, a tail of the Breit-Wigner distribution for the ϕ-meson was also present in sidebands. The leakage of ϕ signal in sidebands was estimated by Monte Carlo simulation for the ϕ photproduction, and they were 5% for sideA and 4% for sideB which were almost independent of E_γ and t. The number of the background counts in sidebands ($N^{real}_{sideA,BG}$, $N^{real}_{sideB,BG}$) were obtained from total numbers of counts in sidebands ($N^{real}_{sideA,all} + N^{real}_{sideB,all}$) by correcting for the leakage of ϕ meson events into sidebands; i.e.

$$N^{real}_{sideA,BG} = N^{real}_{sideA,all} - 0.05N^{real}_{signal} \tag{3.20}$$

$$N^{real}_{sideB,BG} = N^{real}_{sideA,all} - 0.04N^{real}_{signal}, \tag{3.21}$$

where N^{real}_{signal} stands for number of counts in signal region. The number of ϕ-meson signal in the signal region was obtained by subtracting $N_{signal,BG}$ from total number of events in the ϕ signal region (N^{real}_{signal}),

$$N^{real}_{\phi} = N^{real}_{signal} - N_{signal,BG}. \tag{3.22}$$

In order to avoid an oversubtraction of the ϕ-meson tail (Eq. 3.20 and 3.21) which was initially estimated by the raw number of events in the ϕ-meson signal region (N^{real}_{signal}), the calculations (Eq. 3.18-3.22) was repeated by using N^{real}_{ϕ} instead of N^{real}_{signal}.

The observed ϕ-meson sample (Section 3.3) was divided into several parts in terms of E_γ, t and decay angles. The backgrounds were subtracted by this method in each sub-sample.

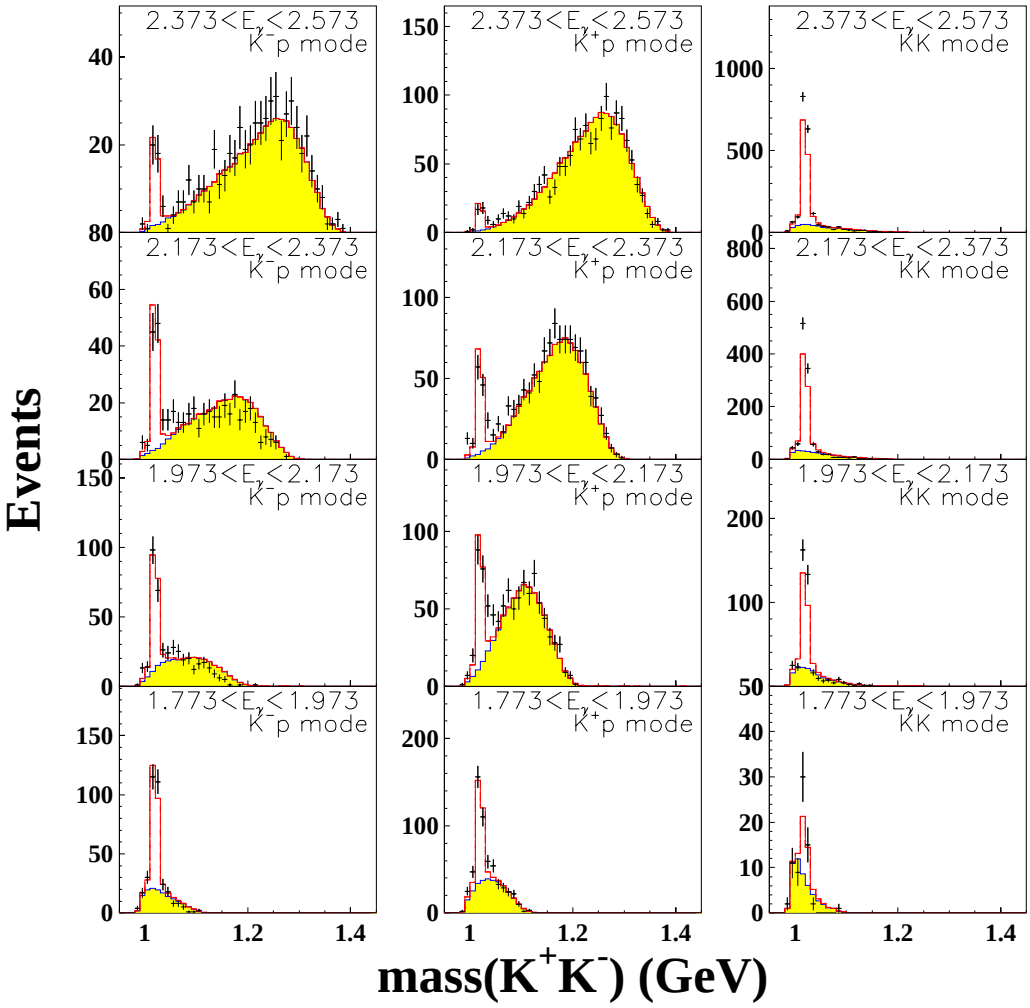

Figure 3.22: The K^+K^- invariant mass distributions in real data for K^-p mode,K^+p mode and KK mode in four different energies. The $\Lambda(1520)$ exclusion cut was applied. The closed circles are data points, the hatched histograms are contributions from the backgrounds calculated by the Monte Carlo simulation, and the dashed curves indicate the results of the fit by Eq. 3.16.

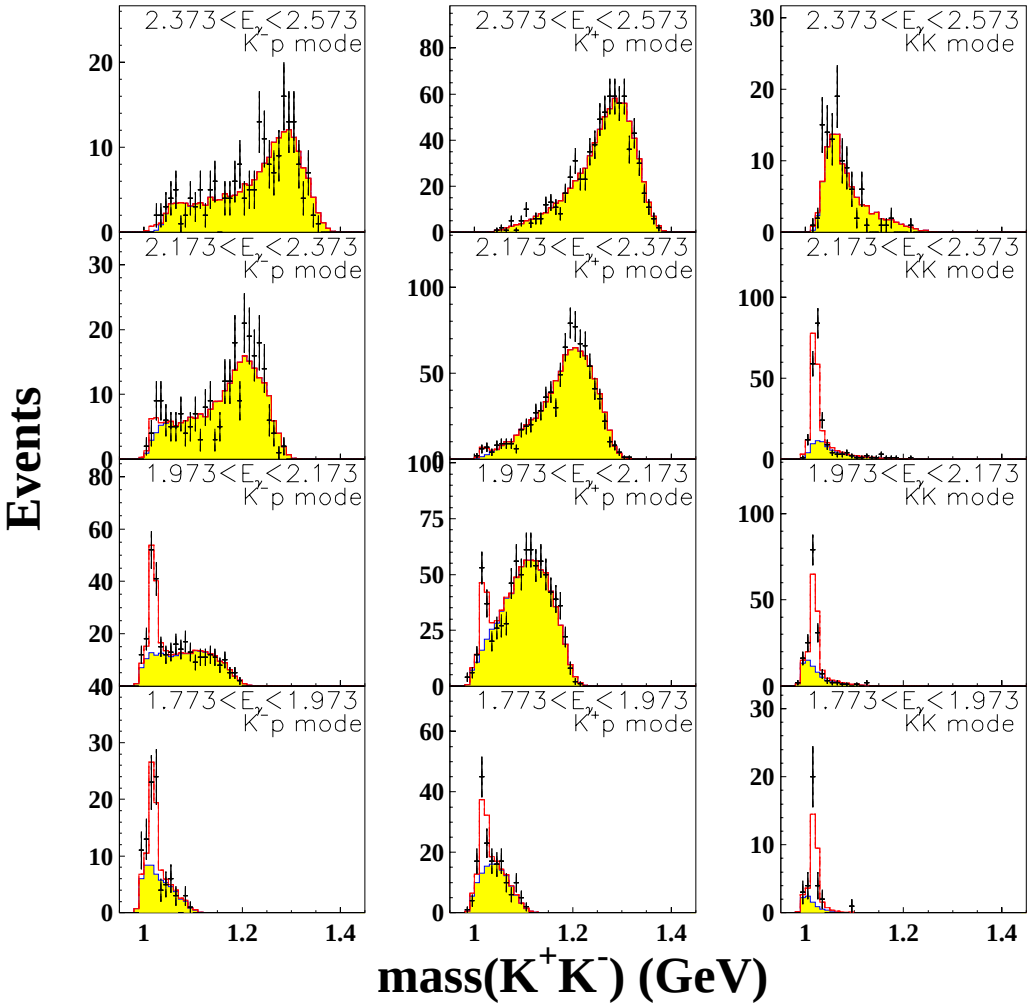

Figure 3.23: The K^+K^- invariant mass distributions in real data for the K^-p mode, the K^+p mode and the KK mode in the four different energies. The $\Lambda(1520)$ selection cut was applied. The closed circles are data points, the hatched histograms are contributions from the backgrounds calculated by the Monte Carlo simulation, and the dashed curves indicate the results of the fit by Eq. 3.17.

3.7 The acceptance

The acceptance for the LEPS spectrometer was obtained by the Monte Carlo simulation for ϕ photoproduction. The same selection cuts and analysis criteria, which were described in Section 3.3, were applied for the Monte Carlo data. The acceptance was given by the number of accepted events divided by the number of generated events in the Monte Carlo simulation.

In the cross section measurement, the data with the horizontal polarization (HZ data) and data with the vertical polarization (VT data) were merged to make an unpolarized data where any polarization effects were canceled in the first order. Note that there was a difference of the beam profile between the vertical polarization and the horizontal polarization, however dependence of the acceptance on the x and y coordinates of the production point was found to be small. Therefore, the effect of different beam profile was neglected. The acceptance for the HZ data was different from that for VT data. The acceptance also depended on the spin density matrix elements. However, the acceptance for the merged data (HZ+VT data) was insensitive to the assumption of the spin density matrix elements in the acceptance calculation since effects in the HZ data was opposite to those in the VT data. The details of the study for the cancellation of the polarization effect in the merged data are described in Appendix B.3. Taking advantage of this cancellation between the HZ data and the VT data, the acceptance was obtained with less ambiguity due to assumption for the spin density matrix elements. In the measurements of the decay angular distributions, the HZ data and the VT data were analyzed separately.

The ϕ photoproduction events were generated according to the zero spin density matrix elements ($\rho^0 = 0$, $\rho^1 = 0$ and $\rho^2 = 0$) assuming that there was no helicity non-conserving amplitude. The E_γ and t-distributions were given by the following form [60], [61]:

$$\begin{aligned} \frac{d\sigma}{dtdE_\gamma} &= \sigma_0 |p_\phi|^n \exp(b\tilde{t}) \\ \tilde{t} &= t + |t|_{min}, \end{aligned} \tag{3.23}$$

where σ_0 is a constant factor and p_ϕ is a space part of the ϕ-meson momentum in the total center-of-mass system. n and b are parameters which are responsible for the energy dependence of the cross section and the slope of the cross section, respectively. A factor $|p_\phi|^n$ was introduced to represent the threshold behavior of the cross section. This phenomenological parameterization gives essentially same E_γ dependence given in [13] and [16]. Similar treatments for the threshold behavior in the vector meson photoproduction are found in [62] and [63]. b was set to 3.0 GeV^{-2}, which represent the observed t-slope in real data which is shown in Section 4.1. There was very little change of acceptance by changing n for events at higher E_γ. The effect of choice of n was only seen around the production threshold where E_γ dependence of the acceptance was large (see Appendix B.1). n was determined iteratively from real data by the analysis described in Section 4.1 so that the Monte Calro simulation matched with observed E_γ increase of the cross section near the threshold in real data. n was chosen to be 0.5.

In order to check whether the iteration in the acceptance calculation worked or not, Monte Calro tests to check the applicability of the acceptance to the data were performed using the Monte Calro data with different choice of the spin density matrix elements and t slope. It was

found that the t distribution is reproduced with reasonable accuracy. Details of the study of acceptance applicability is given in Appendix B.1.

Chapter 4

Results

4.1 Differential cross section

In this section, the differential cross section as a function of the photon energy are presented. The differential cross section was measured with an arbitrary unit in the present analysis.

4.1.1 Extraction of ϕ yield

The photon energy dependence of the differential cross section was measured with a 0.1 GeV step of E_γ from the threshold. The $\tilde{t}(= t + |t|_{min})$ distribution was measured with a 0.1 step of $\tilde{t}$. The E_γ bins and $\tilde{t}$ bins were defined in Table 4.1.

Table 4.1: Definitions of E_γ and $\tilde{t}$ bins

E_γ bin	E_γ (GeV)	$\tilde{t}$ bin	$\tilde{t}$ (GeV^2)
E1	2.273 - 2.373	T1	-0.1 - 0.0
E2	2.173 - 2.273	T2	-0.2 - -0.1
E3	2.073 - 2.173	T3	-0.3 - -0.2
E4	1.973 - 2.073	T4	-0.4 - -0.3
E5	1.873 - 1.973	T5	-0.5 - -0.4
E6	1.773 - 1.873	T6	-0.6 - -0.5
E7	1.673 - 1.773	T7	-0.7 - -0.6
E8	1.573 - 1.673	T8	-0.8 - -0.7
		T9	-0.9 - -0.8

For E1-E4, the events in the KK mode were used. For E5 and E6, the events in both the KK and the $K^\pm P$ modes were used. For E7 and E8, the events in the $K^\pm P$ mode were used in the analysis. Note that number of events which was excluded by this criteria was small.

Some of $\tilde{t}$ bins at larger angles were not used in the analysis since the number of ϕ event was too small or separation of the signal from the backgrounds was too difficult. In order to check, whether the ϕ signals were unambiguously identified or not, the K^+K^- invariant

mass distributions in real data and Monte Carlo data were checked by visual inspection. The $\tilde{t}$ bins which were used in the analysis were judged by the visual inspection. The K^+K^- mass distribution in real data were compared with background shape for the non-resonant KKp given by the Monte Carlo simulation to check whether the background shape resembles the distribution of the ϕ signal or not. The criteria for the selection for the valid $\tilde{t}$ bin was (1) there was a distinct peak at the ϕ-meson mass and (2) the backgrounds were distinguished from the ϕ signal. The K^+K- invariant mass distributions as a function of $\tilde{t}$ are shown in Appendix C.1.

The number of the ϕ events were obtained by subtracting the backgrounds. The background subtraction which was explained in Section 3.6.3 was applied. Since there were two kinds of backgrounds (the non-resonant KKp background and the $\Lambda(1520)$ background), amounts of backgrounds were estimated separately from the two types of sideband samples , $N_{side,\Lambda excl.}$ with the $\Lambda(1520)$ exclusion cut ($M_{K^-p} \leq 1.500$ GeV or $1.540 GeV \leq M_{K^-p}$) and, $N_{side,\Lambda selec.}$ with the $\Lambda(1520)$ selection cut ($1.500 < M_{K^-p} < 1.540$ GeV). The total amount of the background in the signal region ,$N_{signal,BG}$, was sum of the two ; $N_{signal,BG} = N_{BG,\Lambda excl.} + N_{BG,\Lambda selec.}$. Table C.1 summarizes the number of observed ϕ mesons and backgrounds for each E_γ and $\tilde{t}$ bin. The S/N ratio was defined as N_ϕ divided by N_{BG}.

4.1.2 Systematic errors in background subtraction

As shown in Section 3.6.2, the Monte Carlo simulator for the non-resonant KKp production failed to reproduce the relative number of events among different reconstruction modes for the $\Lambda(1520)$ background although the background shape was reproduced well. There was little information to reconstruct the good simulator for the $\Lambda(1520)$ production because of no published data near threshold and poor statistics for $\Lambda(1520)$ production in our data. In this analysis, no selection to exclude $\Lambda(1520)$ was applied because (1) significant amount of ϕ event would be lost by this cut at the lower energy bins where kinematics of the $\Lambda(1520)$ background was very similar to the ϕ events, (2) there was no clear $\Lambda(1520)$ peak was seen in the K^-p mass distribution when ϕ selection cuts were required. As explained in Section C.2, the compromised prescription was to use the Monte Carlo simulator for the non-resonant KKp production to estimate the $\Lambda(1520)$ background. This prescription may introduce a systematic deviation of the result. In order to estimate systematic error, the same analysis was performed with the $\Lambda(1520)$ exclusion cut. The systematic error from the assumption of the background subtraction was quoted from the difference of the results.

4.1.3 Acceptance as a function of $\tilde{t}$

The acceptance of the LEPS detector as a function of E_γ bin and $\tilde{t}$ bin is shown in Figs. 4.1. The acceptance correction was applied to the measured $\tilde{t}$-distribution. The acceptance-corrected $\tilde{t}$ distribution was further corrected by a factor $\omega_\gamma(E_\gamma)$ which took into account difference of the relative photon flux among different E_γ bins due to the non-flat beam energy spectrum. The analysis to obtain the $\omega_\gamma(E_\gamma)$ is described in Appendix A.

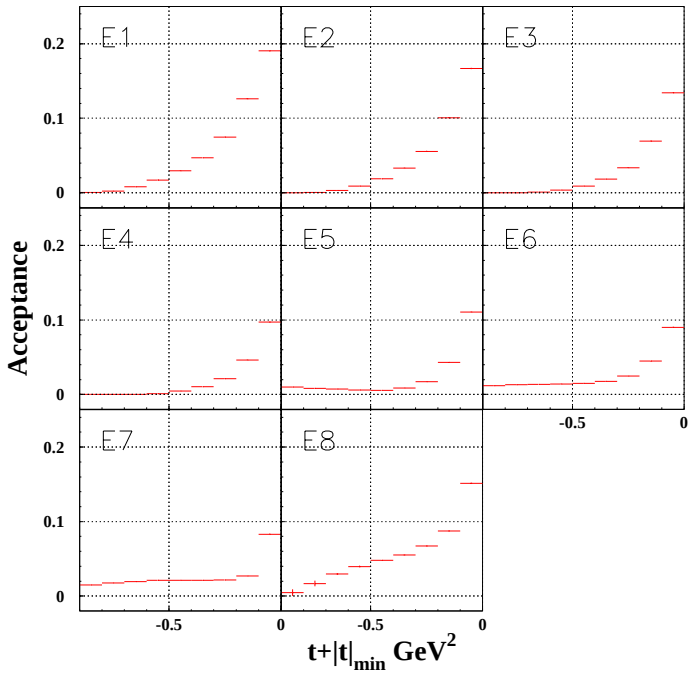

Figure 4.1: Acceptance for the LEPS detector as a function of $\tilde{t}$

4.1.4 The $\tilde{t}$ distribution and the slope parameter

Figure 4.2 shows the t distributions as a function of energy after the above corrections.

A fit to the acceptance-corrected $\tilde{t}$ distribution was applied by a following parameterization :

$$n_0 \exp(b\tilde{t}) a(E_\gamma, \tilde{t}) / \omega_\gamma(E_\gamma), \tag{4.1}$$

where n_0 and b are fitting parameters, $a(E_\gamma, \tilde{t})$ is a t-dependent factor representing a kinematical reduction of the physical region. As shown in the solid curve in Fig. 3.18 in Section 3.5, a boundary of the physical region placed by the $|t|_{max}$ introduces an additional t-dependent factor in the $\tilde{t}$ distribution, which is nothing to do with the physics processes of the reaction. The $\tilde{t}$ distribution at E8 bin was corrected by the factor $a(E_\gamma, \tilde{t})$ so that the observed slope parameter b in E8 had the same meaning as those in E1-E7 bins. This correction was applied only for E8; i.e. $a(E_\gamma, \tilde{t}) \leq 1$ for E8, $a(E_\gamma, \tilde{t}) = 1$ for E1-E7. Figure 4.3 shows the correction factor $a(E_\gamma, \tilde{t})$ in E8 bin which was calculated by assuming the same energy dependence of the cross section in the acceptance calculation.

The results of the fit to the $\tilde{t}$ distribution was summarized in Table 4.2. The quality of the fit was reasonably good based on the χ^2/ndf. The results of the same analysis with the $\Lambda(1520)$ exclusion cut are shown in Table 4.3

The solid curve in Fig. 4.2 indicates the result of the fit. The slope parameter b as a function of photon energy is shown in Fig. 4.4(a) where error bars in the data points indicate statistical error and the hatched histogram represents systematic error from the background

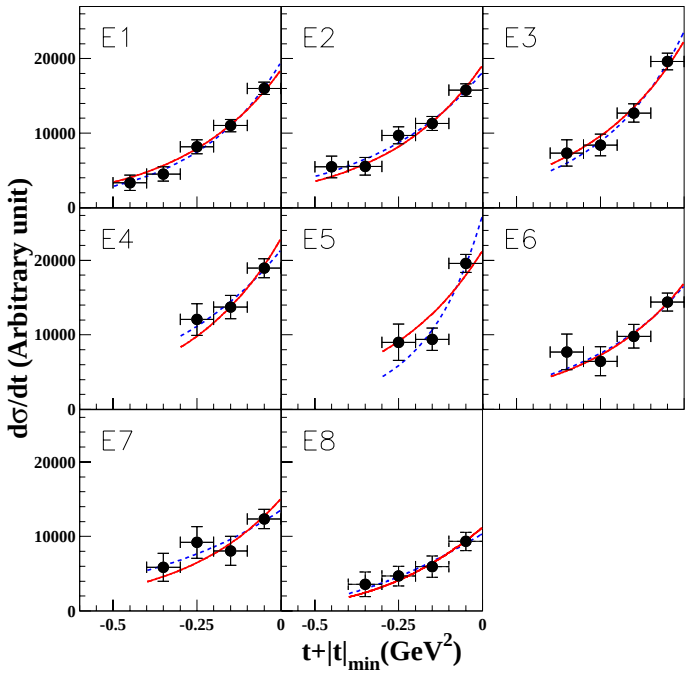

Figure 4.2: Acceptance-corrected $\tilde{t}$ distribution. Dashed curve indicates a fit to the data by Eq. 4.1 with b as a free parameter. the solid curve represents a fit by a constant slope $b = 3.376$ GeV^{-2}.

subtraction. The slope parameters were almost constant. Note that the slope of E5 bin is larger than the other energies, but error bar is also large. A hypothesis test whether the observed energy dependence of the slope can be explained by a statistical fluctuation of the smooth energy dependence was examined as follows.

The energy dependence of the observed slope was parameterized by a simple function. The solid line drawn in Fig. 4.4(a) is a fit by a constant function (= average of slope). The fit gave $\chi^2/ndf = 1.33$. Similarly, a fit by a linear function (A0 + A1 E_γ) is shown in Fig. 4.4(b). χ^2/ndf was 1.37. Both of the fitting functions (constant, linear) are able to fit the data with reasonable χ^2. It supports the hypothesis for the smooth change of slope with energy. In the present analysis, the larger slope in E5 was regarded as a statistical fluctuation.

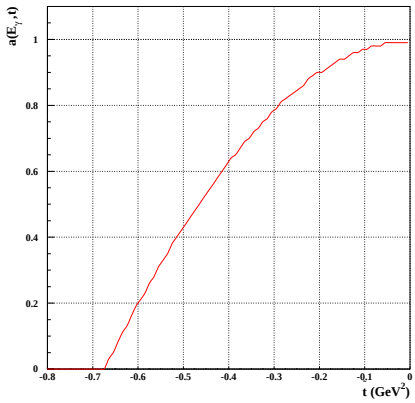

Figure 4.3: Correction factor of reduction of the physical region in E8

Table 4.2: Results of the fit to the $\tilde{t}$ distributions

E_γ bin	n_0 (events/0.1 GeV^2)	b (GeV^{-2})	χ^2/ndf
1	2714 ± 165	3.83 ± 0.41	0.3070
2	2684 ± 172	2.93 ± 0.42	0.5984
3	2884 ± 223	3.92 ± 0.63	0.4191
4	2451 ± 237	2.59 ± 0.87	0.4278
5	2597 ± 284	5.95 ± 1.34	2.4001
6	1471 ± 171	3.17 ± 0.99	0.6531
7	1090 ± 146	2.28 ± 0.93	0.6105
8	794 ± 139	2.61 ± 1.28	0.2044

Table 4.3: Results of the fit to the $\tilde{t}$ distributions with the $\Lambda(1520)$ exclusion cut

E_γ bin	n_0 (events/0.1 GeV^2)	b (GeV^{-2})	χ^2/ndf
1	2706 ± 164	3.82 ± 0.41	0.2553
2	2688 ± 173	2.81 ± 0.42	0.8605
3	2899 ± 227	3.73 ± 0.64	0.0226
4	2401 ± 255	2.44 ± 0.95	0.1135
5	2686 ± 334	6.18 ± 1.46	1.3342
6	1510 ± 254	3.70 ± 1.42	3.3663
7	1546 ± 230	4.37 ± 1.29	0.5527
8	826 ± 147	2.93 ± 1.37	0.3798

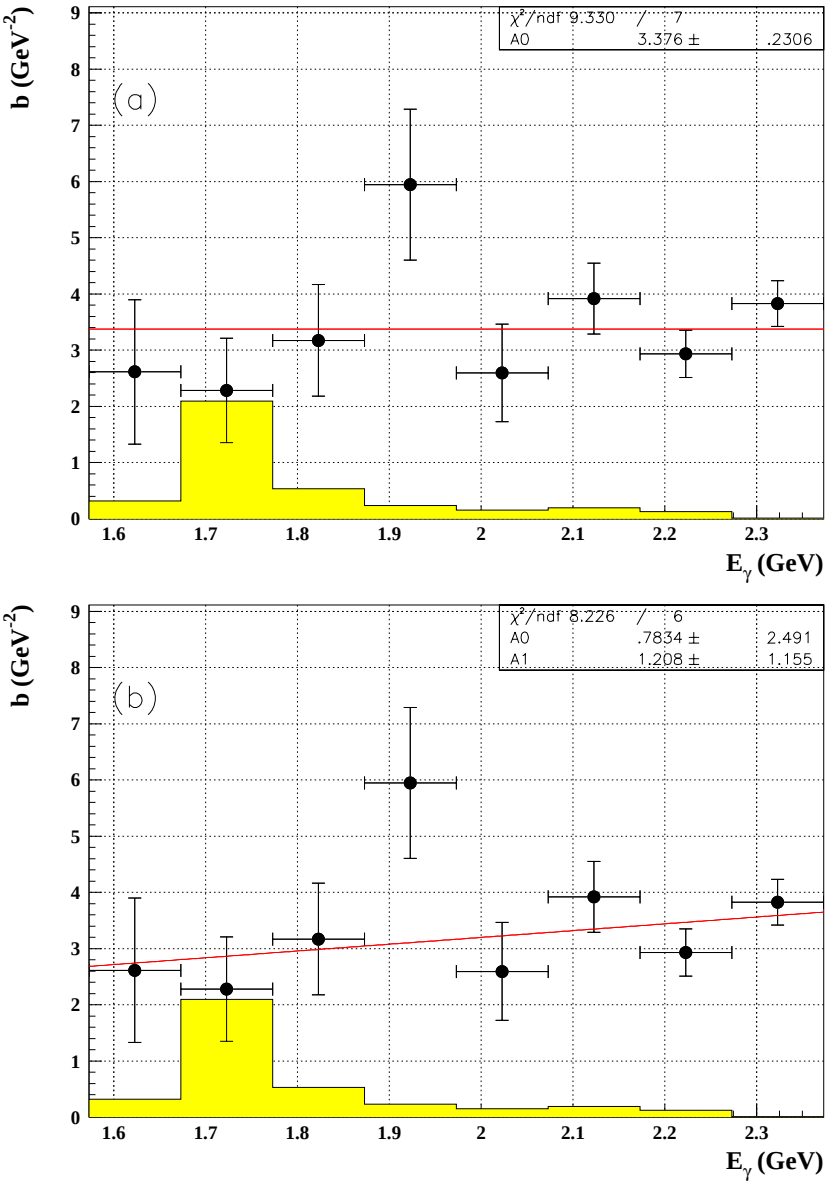

Figure 4.4: The energy dependence of the slope parameter b. Error bar represents statistical error only. The hatched histogram indicates the systematic error due to background subtraction.

4.1.5 Energy dependence of differential cross section at $\tilde{t} = 0$ GeV^2

Figure 4.5 shows the energy dependence of the differential cross section at $\tilde{t} = 0$ GeV^2 without assuming any smooth energy dependence of the t-slope. The error bar represents statistical error only, the hatched histogram indicates the systematic error from the background subtraction.

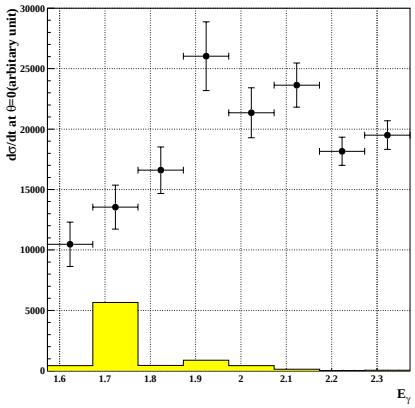

Figure 4.5: The energy dependence of the differential cross section at $\tilde{t} = 0$. Error bar represents statistical error only. Hatched histogram indicates the systematic error due to background subtraction.

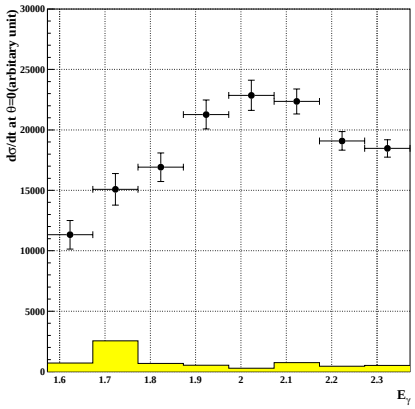

Figure 4.6: The energy dependence of the differential cross section at $\tilde{t} = 0$ with constant slope $b = 3.376$ GeV^{-2}. Error bar represents statistical error only. The hatched histogram indicates the systematic error due to background subtraction and assumption of E_γ dependence of the slope.

Since the hypothesis of a smooth energy dependence for the slope was found to be consistent with the data, the same analysis was repeated assuming a constant slope as a function of energy. Figure 4.6 shows the energy dependence of the differential cross section at $\tilde{t} = 0$ GeV^2 with an assumption of a constant slope ($b = 3.376$ GeV^{-2}, see Fig. 4.4(a)) Since the choice of the energy dependence of the slope parameter was not necessary to be constant, a systematic error

due to choice of the energy dependence was quoted from deviations of the results when the linear function was used. The systematic error from the background subtraction and the choice of energy dependence of the slope were added in quadrature, they are shown as the hatched histogram in Fig. 4.6. Fig. 4.6. The same results are tabulated in Table 4.4.

Table 4.4: Differential cross sections at $\tilde{t} = 0$ (arbitrary unit).

E_γ bin	$d\sigma/dt\|_{\tilde{t}=0}$ (Method I)	$d\sigma/dt\|_{\tilde{t}=0}$ (Method II)
1 (1.573 – 1.673 GeV)	$1.05 \pm 0.18 \times 10^4$	$1.13 \pm 0.12 \times 10^4$
2 (1.673 – 1.773 GeV)	$1.35 \pm 0.18 \times 10^4$	$1.51 \pm 0.13 \times 10^4$
3 (1.773 – 1.873 GeV)	$1.66 \pm 0.19 \times 10^4$	$1.69 \pm 0.12 \times 10^4$
4 (1.873 – 1.973 GeV)	$2.60 \pm 0.28 \times 10^4$	$2.13 \pm 0.12 \times 10^4$
5 (1.973 – 2.073 GeV)	$2.13 \pm 0.21 \times 10^4$	$2.29 \pm 0.12 \times 10^4$
6 (2.073 – 2.173 GeV)	$2.36 \pm 0.18 \times 10^4$	$2.24 \pm 0.10 \times 10^4$
7 (2.173 – 2.273 GeV)	$1.82 \pm 0.12 \times 10^4$	$1.91 \pm 0.08 \times 10^4$
8 (2.273 – 2.373 GeV)	$1.95 \pm 0.12 \times 10^4$	$1.85 \pm 0.07 \times 10^4$

The χ^2 test was examined to check the quality of the fits for three different treatments of the energy dependence of the slope. Table 4.5 shows χ^2 for three methods. No significant deterioration of the χ^2 was seen when a constant or linear energy dependence for the slope was used.

The numerical values for the differential cross sections are tabulated in E.1.

Table 4.5: comparison of χ^2 values for various fitting methods

Method	description	χ^2	ndf	χ^2/ndf	prob(χ^2,ndf)
I	slope as a free parameter	9.32	16	0.582	0.900
II	fixed slope (constant)	19.51	23	0.848	0.671
III	fixed slope (linear)	18.85	22	0.857	0.654

4.2 The decay angular distribution

Measurement of the decay angular distributions of ϕ meson is described in this section. The angular distributions of the K^+ from the ϕ decay were measured at forward angles in two energy ranges (1) $2.173 < E_\gamma < 2.373$ GeV, $\tilde{t}$ >-0.2 GeV^{-2} and (2) $1.973 < E_\gamma < 2.173$ GeV, $\tilde{t}$ >-0.2 GeV^{-2} with the KK reconstruction mode. The kinematical range (1) and (2) were called ET1 and ET2,respectively. The angular distributions for 5 angular variables ($\cos\theta, \phi, \phi-\Phi, \phi+\Phi, \Phi$) were used to extract the spin density matrix elements. The angles were divided into 12 bins with equal bin size.

4.2.1 The acceptance for VT data and HZ data

The acceptance for different polarization angle (the VT data and the HZ data) was obtained separately from the Monte Carlo simulation. As a starting point, it was assumed that all the spin density elements are 0 (zero SDMs). The spin density matrix elements were determined by using the acceptance given with zero density matrix elements. The measured spin density matrix elements were then used in the acceptance calculation iteratively. The acceptance with zero SDMs as a function of angles are shown in Fig. 4.7 for ET1 and Fig. 4.8 for ET2. b

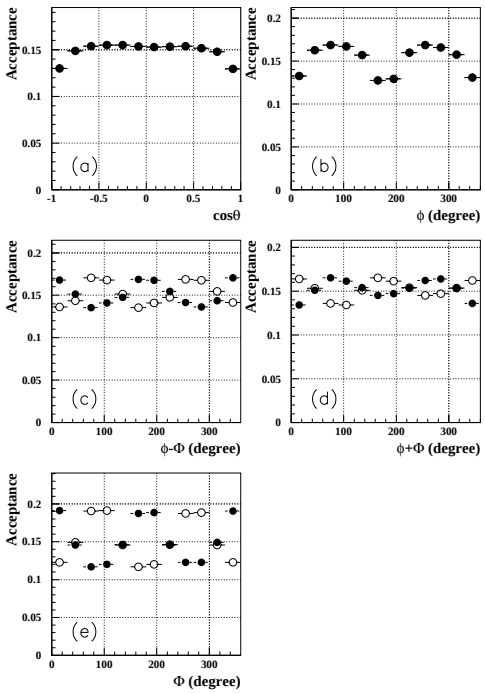

Figure 4.7: Acceptance with zero SDMs for ET1 as a function of angles (a) $\cos\theta$, (b) ϕ, (c) $\phi - \Phi$, (d) $\phi + \Phi$, (e) Φ. The open circles indicates the acceptance for the VT data and the closed circles indicates the acceptance for the HZ data. The acceptance with zero SDMs for the VT and HZ data are same for (a) and (b).

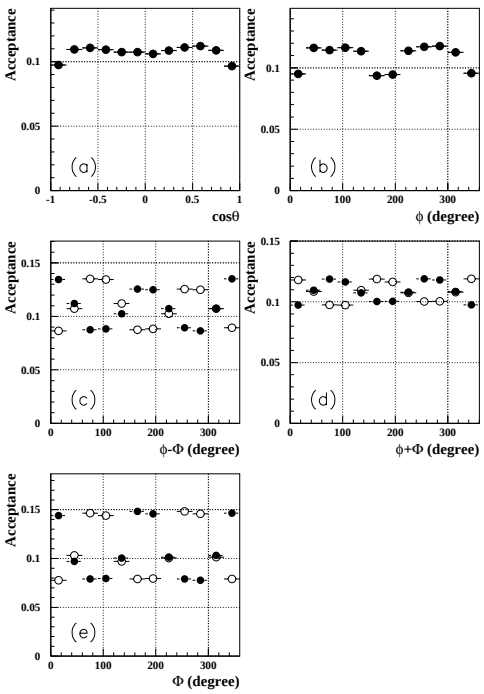

Figure 4.8: Acceptance with zero SDMs for ET2 as a function of angles (a) $\cos\theta$, (b) ϕ, (c) $\phi - \Phi$, (d) $\phi + \Phi$, (e) Φ. The open circles indicates the acceptance for the VT data and the closed circles indicates the acceptance for the HZ data. The acceptance for the VT and HZ data are same for (a) and (b).

4.2.2 Number of ϕ events

The number of events from the ϕ photoproduction as a function of the decay angle were measured by the same way as those in the measurement of the differential cross section (Section 4.1). The background subtraction was applied in each angular bin. The number of events for ϕ signal and background are shown in Table C.2, Table C.3, Table C.4 and Table C.3 for 12 bins of angles. It was found that S/N ratio was large in all angular bins in contrast to the events at lower energies (Table C.1). The K^+K^- invariant mass distributions in each angular bin were checked by visual inspection as the same way in the differential cross section (Appendix C.1, Figs. C.3-C.15). Clear peak at the ϕ-meson mass was identified in all angular bins without ambiguity. Therefore, all angular bins were included in the analysis.

4.2.3 The spin density matrix elements

The acceptance-corrected angular distributions were analyzed to extract the density matrix elements. The decay angular distributions for ET1 and ET2 sample are shown in Fig. 4.9 and Fig. 4.10, respectively. The acceptance used to obtain these plots were given by the first iteration of the acceptance calculation (acceptance with non-zero SDMs). The dashed curve indicates a fit to the distribution. Fitting procedure is explained below.

Fit to the one-dimensional angular distribution was applied using following parameterizations :

$$
\begin{aligned}
W(\cos\theta) &= N_0(\frac{1}{2}(1-\tilde{\rho}_1)(1-\cos^2\theta)+\tilde{\rho}_1\cos^2\theta) && (4.2)\\
W(\phi) &= N_0(1-2\tilde{\rho}_2\cos(2\phi)) && (4.3)\\
W(\phi-\Phi) &= N_0(1+2P_\gamma\tilde{\rho}_3\cos(2(\phi-\Phi)) && (4.4)\\
W(\phi+\Phi) &= N_0(1+2P_\gamma\tilde{\rho}_4\cos(2(\phi+\Phi)) && (4.5)\\
W(\Phi) &= N_0(1-P_\gamma\tilde{\rho}_5\cos 2\Phi), && (4.6)
\end{aligned}
$$

where N_0 and $\tilde{\rho}_1$, $\tilde{\rho}_2$, $\tilde{\rho}_3$, $\tilde{\rho}_4$, $\tilde{\rho}_5$ are parameters in the fit. P_γ is a degree of photon polarization, calculated by QED (Fig. 2.2) multiplied by the polarization of the laser (P_{laser}). The polarization of the laser was obtained by averaging the measured polarization for each run [44] weighted by the number of photon. The P_{laser} was 0.9869 for the VT data and 0.9498 for the HZ data. The average polarization of the photon P_γ was 0.918, 0.883 in ET1 for the VT and the HZ data, respectively and 0.877, 0.843 in ET2.

The fitting to the angular distributions by Eqs. 4.2-4.6 was made simultaneously for the VT and the HZ data.

In comparison of Eqs. 4.2-4.6 with Eqs. 1.4-1.8, there are following relations between fitting parameters $\tilde{\rho}_i(i=1-5)$ and the spin density matrix elements (see Section 1.2):

$$
\begin{aligned}
\tilde{\rho}_1 &= \rho^0_{00} && (4.7)\\
\tilde{\rho}_2 &= \rho^0_{1-1} && (4.8)\\
\tilde{\rho}_3 &= (\rho^1_{1-1}-\mathrm{Im}\rho^2_{1-1})/2 && (4.9)\\
\tilde{\rho}_4 &= (\rho^1_{1-1}+\mathrm{Im}\rho^2_{1-1})/2 && (4.10)\\
\tilde{\rho}_5 &= 2\rho^1_{11}+\rho^1_{00} && (4.11)
\end{aligned}
$$

Results of the fits obtained using the acceptance with zero SDMs are summarized in Table 4.6 and Table 4.7. Fitting results with different choices of number of bin (10 and 8 bins) are also shown in these tables.

The acceptance calculation was iterated with the measured spin density matrix elements shown in Table 4.6 and Table 4.6; i.e.

$$
\begin{aligned}
\rho^0_{00} &= 0.07,\\
\rho^0_{1-1} &= 0.03,\\
\rho^1_{1-1} &= -\mathrm{Im}\rho^2_{1-1} = 0.18
\end{aligned}
$$

(other elements were set to 0) for ET1,

$$
\rho^0_{00} = 0.03,
$$

$$\begin{aligned}\rho^0_{1-1} &= 0.12,\\ \rho^1_{1-1} &= -\mathrm{Im}\rho^2_{1-1} = 0.18\end{aligned}$$

(other elements were set to 0) for ET2, where a relation $\rho^1_{1-1} = -\mathrm{Im}\rho^2_{1-1}$ was assumed because $\tilde{\rho}_4$ was small. The same analysis with the acceptance with non-zero SDMs was performed. The results of the fits are shown in the dashed curves in Figs. 4.9-4.10 and Table 4.8 and 4.9. Difference of the results for the different bin sizes was found to be small. The bin size of $N_{bin} = 12$ was selected because fitting error was smallest among choices of $N_{bin} = 8, 10, 12$. Based on χ^2/ndf, quality of the fit is reasonably good. The fitting curves (the dashed curves in Figs. 4.9-4.10) described the data points for the VT data and the HZ data within error bars. It indicates a good consistency between the VT and the HZ data. No systematic difference between the VT and HZ data were observed. Systematic error from the background subtraction was estimated by a similar manner which was explained in the cross section measurement. The systematic errors were found to be small as understood from good S/N ratio shown in Table C.2-C.5. The spin density matrix elements, statistical errors and systematic errors are summarized in Table 4.10.

The measured angular distributions were normalized in the standard normalization:

$$\begin{aligned}&\int_{-1}^{1} W(\cos\theta) d\cos\theta = 1,\\ &\int_{0}^{2\pi} W(x)dx = 1.(x = \phi, \Phi, \phi - \Phi, \phi + \Phi)\end{aligned} \tag{4.12}$$

The normalized angular distributions for all data (the VT data + the HZ data) are shown in Fig. 4.11. The systematic error from the background subtraction are shown by the hatched histogram in each plot. The numerical values results for the decay angular distributions are tabulated in E.2.

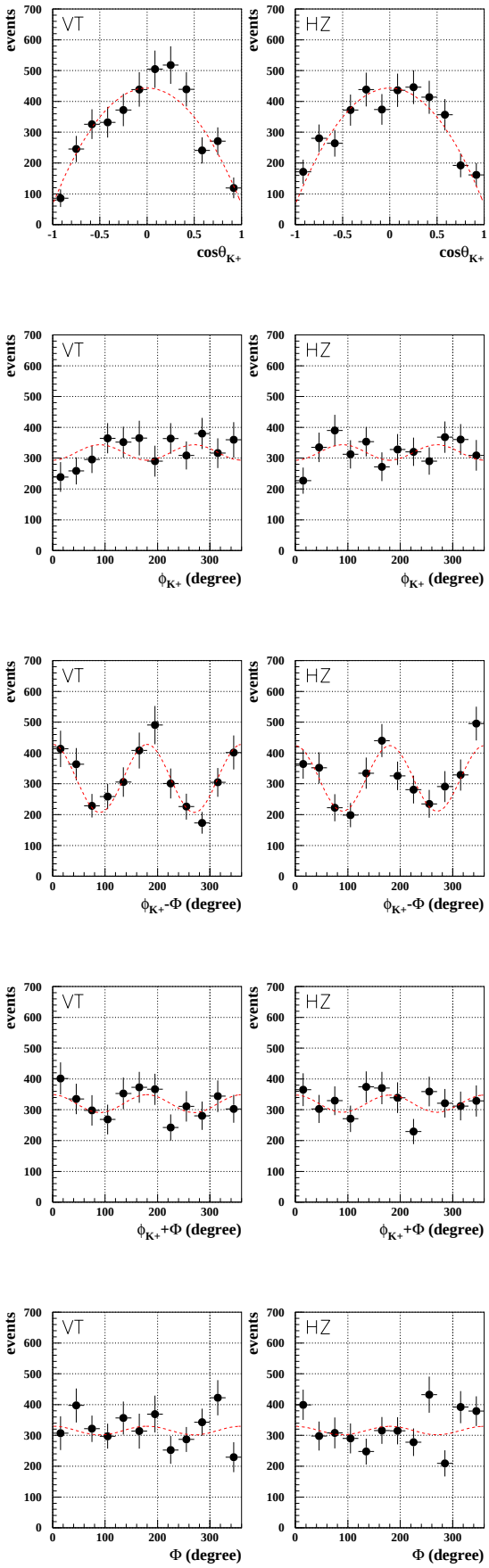

Figure 4.9: Decay angular distribution for the VT data and the HZ data at 2.173< E_γ <2.373 GeV, -0.2< $\tilde{t}$ after the acceptance correction. The solid curve indicates a fit to the data.

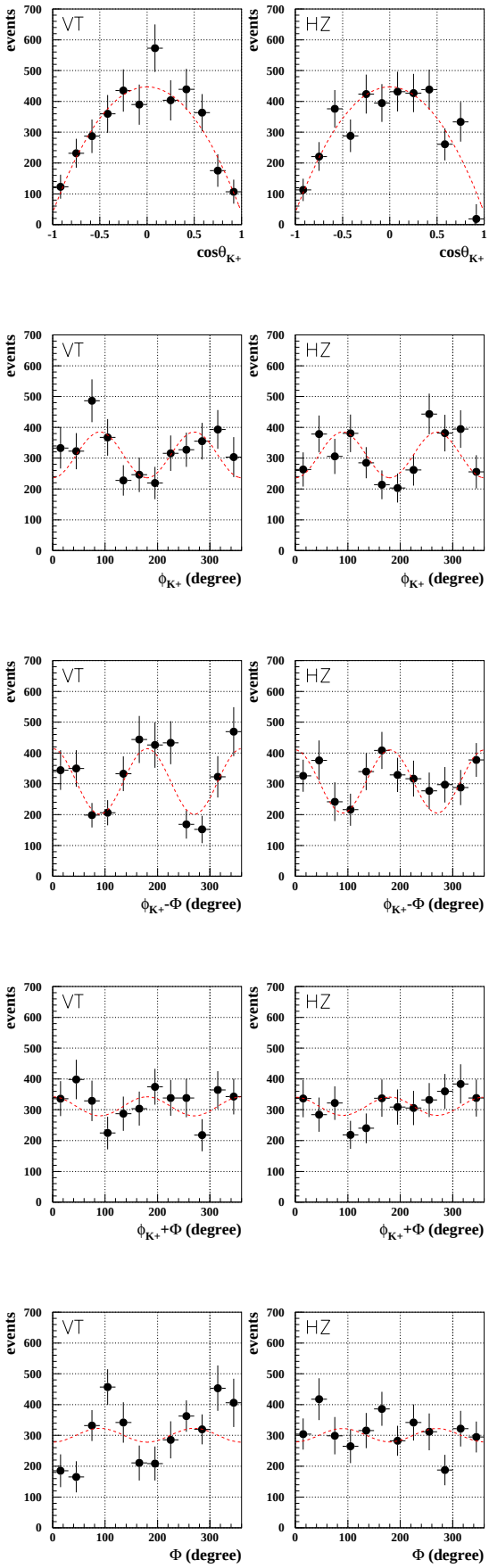

Figure 4.10: Decay angular distribution for the VT data and the HZ data at 1.973< E_γ <2.173 GeV, -0.2< $\tilde{t}$ after the acceptance correction. The solid curve indicates a fit to the data.

Table 4.6: Results of fit to the angular distributions for ET1 with the acceptance with zero SDMs

angle	N_{bin}	N_0	$\tilde{\rho}$	χ^2/ndf
$\cos\theta$	12	957.5 ± 29.4	0.069 ± 0.020	0.9295
	10	1147.6 ± 35.3	0.067 ± 0.020	1.0579
	8	1437.2 ± 44.1	0.080 ± 0.021	1.1086
ϕ	12	316.5 ± 9.8	0.039 ± 0.022	0.8198
	10	379.4 ± 11.7	0.040 ± 0.022	1.0735
	8	473.5 ± 14.6	0.060 ± 0.022	1.3450
$\phi - \Phi$	12	317.0 ± 9.8	0.190 ± 0.024	0.7232
	10	381.3 ± 11.8	0.197 ± 0.024	0.6927
	8	477.6 ± 14.8	0.183 ± 0.024	0.8786
$\phi + \Phi$	12	319.4 ± 9.8	0.049 ± 0.025	0.7513
	10	385.3 ± 11.8	0.049 ± 0.024	0.5695
	8	484.2 ± 14.7	0.059 ± 0.024	0.3357
Φ	12	315.1 ± 9.7	0.033 ± 0.048	1.4511
	10	381.2 ± 11.7	0.076 ± 0.049	1.2194
	8	480.5 ± 14.7	0.041 ± 0.048	0.8538

Table 4.7: Results of fit to the angular distributions for ET2 with the acceptance with zero SDMs

angle	N_{bin}	N_0	$\tilde{\rho}$	χ^2/ndf
$\cos\theta$	12	945.2 ± 35.3	0.039 ± 0.023	0.8775
	10	1138.0 ± 42.4	0.037 ± 0.024	0.6184
	8	1419.5 ± 53.1	0.044 ± 0.026	0.9703
ϕ	12	309.0 ± 11.5	0.117 ± 0.027	0.9469
	10	371.8 ± 13.9	0.106 ± 0.027	1.1597
	8	469.6 ± 17.4	0.092 ± 0.026	0.9079
$\phi - \Phi$	12	309.0 ± 11.8	0.199 ± 0.030	0.9262
	10	374.4 ± 14.2	0.188 ± 0.030	0.8167
	8	465.9 ± 17.7	0.180 ± 0.031	1.0529
$\phi + \Phi$	12	313.6 ± 11.7	0.061 ± 0.031	0.8438
	10	377.9 ± 14.0	0.062 ± 0.031	0.8779
	8	470.2 ± 17.5	0.058 ± 0.031	1.5022
Φ	12	304.6 ± 11.5	0.166 ± 0.062	1.9331
	10	370.1 ± 13.9	0.224 ± 0.062	1.6885
	8	467.7 ± 17.5	0.125 ± 0.063	1.7352

Table 4.8: Results of fit to the angular distributions for ET1 with the acceptance with non-zero SDMs

angle	N_{bin}	N_0	$\tilde{\rho}$	χ^2/ndf
$\cos\theta$	12	952.8 ± 29.3	0.069 ± 0.020	0.9878
	10	1142.1 ± 35.1	0.068 ± 0.020	1.1367
	8	1431.9 ± 44.0	0.081 ± 0.021	1.1929
ϕ	12	318.5 ± 9.8	0.039 ± 0.022	0.7852
	10	381.5 ± 11.8	0.041 ± 0.022	1.0622
	8	475.8 ± 14.7	0.060 ± 0.022	1.3423
$\phi - \Phi$	12	317.5 ± 9.9	0.189 ± 0.024	0.7204
	10	382.4 ± 11.8	0.197 ± 0.024	0.6595
	8	478.5 ± 14.8	0.181 ± 0.024	0.8377
$\phi + \Phi$	12	319.9 ± 9.8	0.049 ± 0.025	0.7627
	10	385.9 ± 11.8	0.050 ± 0.024	0.5764
	8	485.0 ± 14.8	0.061 ± 0.024	0.3332
Φ	12	315.8 ± 9.8	-0.049 ± 0.048	1.5033
	10	382.1 ± 11.8	-0.002 ± 0.049	1.1849
	8	481.6 ± 14.7	-0.035 ± 0.048	0.8874

Table 4.9: Results of fit to the angular distributions for ET2 with the acceptance with non-zero SDMs

angle	N_{bin}	N_0	$\tilde{\rho}$	χ^2/ndf
$\cos\theta$	12	933.2 ± 35.0	0.042 ± 0.023	0.8860
	10	1123.5 ± 41.9	0.041 ± 0.024	0.6476
	8	1403.6 ± 52.6	0.049 ± 0.026	0.9606
ϕ	12	310.5 ± 11.6	0.120 ± 0.027	0.8718
	10	373.2 ± 13.9	0.108 ± 0.027	1.1033
	8	469.0 ± 17.4	0.099 ± 0.026	1.0182
$\phi - \Phi$	12	307.7 ± 11.7	0.197 ± 0.030	0.7846
	10	372.2 ± 14.1	0.195 ± 0.030	0.7374
	8	464.9 ± 17.6	0.176 ± 0.031	0.7186
$\phi + \Phi$	12	311.3 ± 11.6	0.056 ± 0.031	0.7654
	10	374.6 ± 13.9	0.059 ± 0.031	0.8367
	8	466.8 ± 17.4	0.052 ± 0.031	1.3501
Φ	12	300.6 ± 11.4	0.085 ± 0.062	1.9587
	10	365.6 ± 13.8	0.158 ± 0.062	1.6265
	8	462.6 ± 17.3	0.059 ± 0.063	1.7217

Table 4.10: Spin density matrix elements in ET1 and ET2

Spin density matrix	ET1 (2.173< E_γ <2.373 GeV) (sys. error)	ET2 (1.973< E_γ <2.173 GeV) (sys. error)
$\tilde{\rho_1}$	0.069 ± 0.020 (0.002)	0.042 ± 0.024 (0.008)
$\tilde{\rho_2}$	0.039 ± 0.022 (0.014)	0.120 ± 0.027 (0.011)
$\tilde{\rho_3}$	0.189 ± 0.024 (0.006)	0.197 ± 0.030 (0.022)
$\tilde{\rho_4}$	0.049 ± 0.025 (0.006)	0.056 ± 0.031 (0.012)
$\tilde{\rho_5}$	-0.049 ± 0.048 (0.005)	0.085 ± 0.062 (0.048)

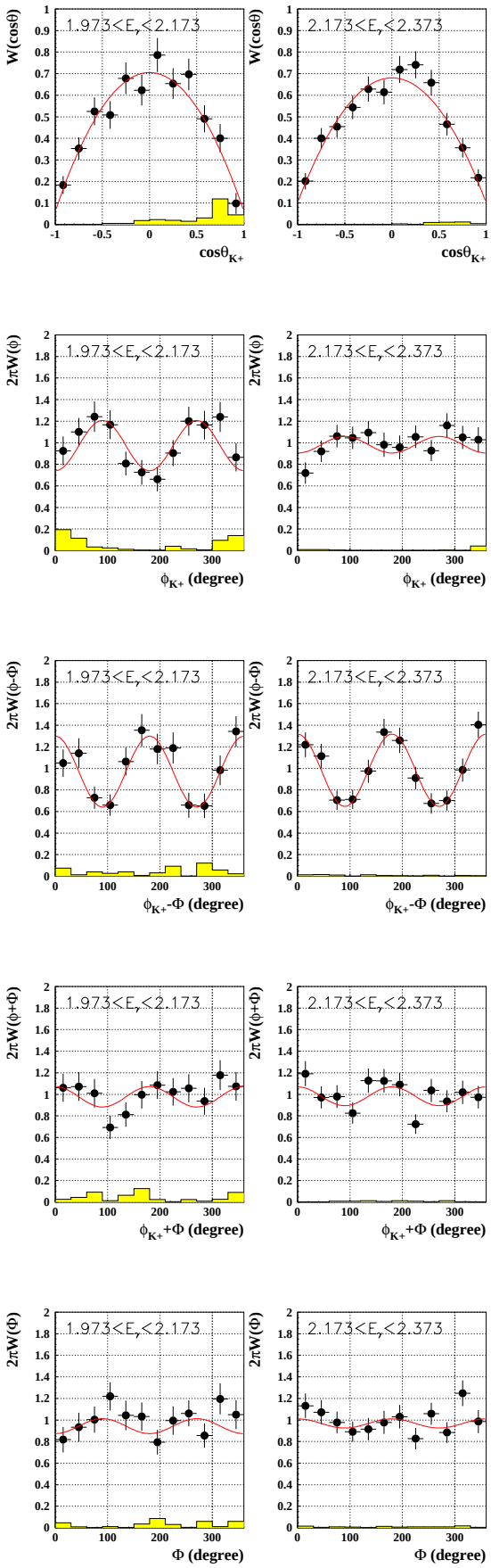

Figure 4.11: The decay angular distribution for -0.2< $\tilde{t}$, 2.273< E_γ <2.373 GeV (ET1) and 1.973< E_γ <2.173 GeV (ET2). The solid curve indicates a fit to the data. Systematic errors are shown in hatched histogram

Chapter 5

Discussions

Differential cross section

The differential cross section at forward angles (Fig. 4.2) has a forward peaking shape. This means that the diffractive t-channel exchange is the dominant contribution in ϕ photoproduction at forward angles. Fig. 5.1 shows the slope parameter b as a function of photon energy for the LEPS data and the previous published data. No strong energy dependence of the slope was observed.

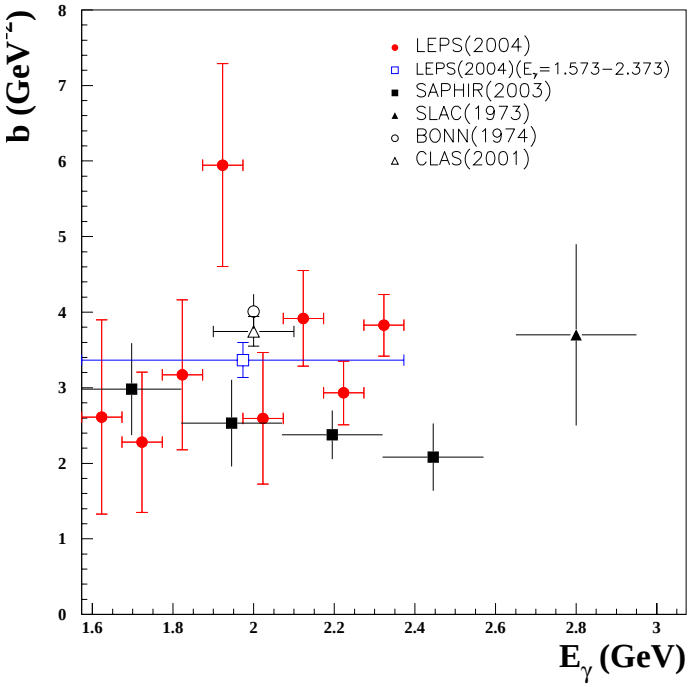

Figure 5.1: Slope parameters b as a function of the photon energy. The closed circles indicate the LEPS results in steps of 0.1 GeV. The open square is the average value for 1.573< E_γ <2.373 GeV. The other data are taken from [7, 22, 27, 64]

The energy dependence of differential cross sections at $\tilde{t} = 0$ GeV^2 ($\theta_{phi}^{CM} = 0^\circ$) showed a non-monotonic behavior (Fig. 4.5 and Fig. 4.6), i.e. a peak appeared around $E_\gamma = 2$ GeV. The absolute values for the cross section have not been determined yet. However, it is hard to change the relative dependence on the energy by further analysis to obtain the absolute cross sections since all energy dependent corrections were applied to the data.

The data was compared with the results calculated in the model [18] including the Pomeron exchange and π/η exchange processes. Figure 5.2 shows the experimental data with a normalization factor to adjusting the data points to the model prediction. The normalization factor was obtained by the least square fit to the model prediction. The fit gives $\chi^2/ndf = 261.5/7$. The model prediction, which agrees with the previous data at higher energies, was not well described the present experimental data points. The Regge theory predicts that the standard Pomeron exchange provides only the monotonical increase of ϕ-meson photoproduction cross sections with increasing the energy [60]. Therefore it is expected that the peak of the cross-sections at $E_\gamma \sim 2$ GeV is not explained with the Pomeron exchange process only. We note that no peaking structure was reported in the recent measurement of the total cross-sections from the threshold to 2.6 GeV by SAPHIR collaboration [27].

A question addressed here is whether the non-monotonic behavior is a signature of necessity for introducing a new production mechanism. In order to explain the non-monotonic behavior, there should be a contribution which increases as the energy decreases. In the Regge theory, when energy decreases, all of meson trajectories, except for the Pomeron trajectory, increase their contribution and the possible daughter Pomeron trajectory (glueball trajectory) is also expected to increase its contribution. Fig. 5.3 shows the differential cross section at $\tilde{t} = 0$ GeV^2 ($\theta_{\phi}^{CM} = 0^\circ$) with a normalization to the same model at 2.327 GeV where the contribution from the Pomeron exchange is expected to be the maximum among the LEPS data points. The extra part on top of the solid curve may give an estimate of the possible additional contribution which was missing in the current model. Only the half of the measured cross section was explained by the standard production mechanisms (the Pomeron and the pseudo scalar exchanges) at 2 GeV. Note that this speculation is not very conclusive since there was a large discrepancy at 2 GeV between the LEPS data and the earlier measurements [22, 64, 27] with this normalization (see the plot on the left-hand side of Fig. 5.3). Regardless of the normalization, no satisfactory interpretation was obtained by the standard production mechanisms.

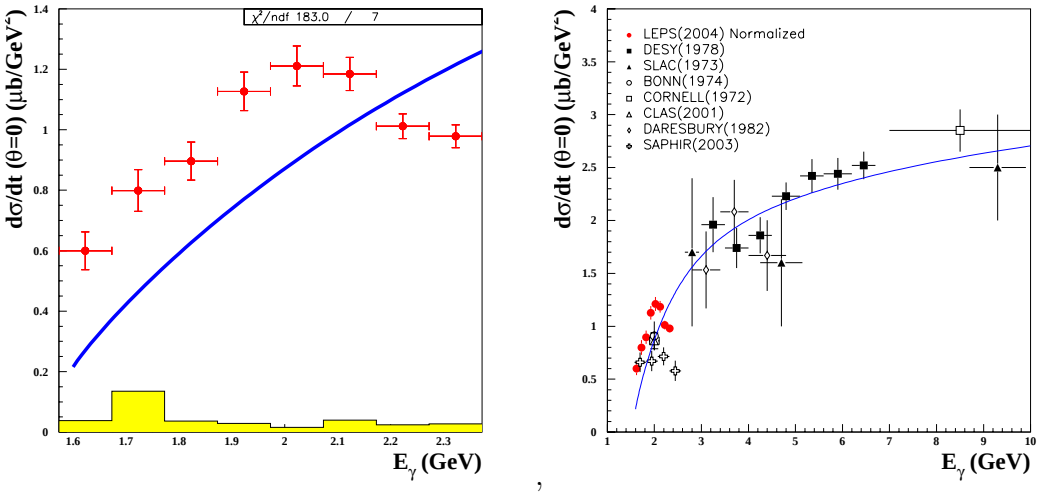

Figure 5.2: Differential cross sections at $\tilde{t} = 0$ GeV^2 ($\theta_\phi^{CM} = 0°$). The closed circle indicates the LEPS data. The solid curve shows the prediction from the model (the Pomeron + the pseudo scalar exchanges)[18]. The LEPS data points were normalized by the factor which minimize the χ^2 of the fit to the model. The other data points are taken from [7, 22, 65, 25, 13, 64]

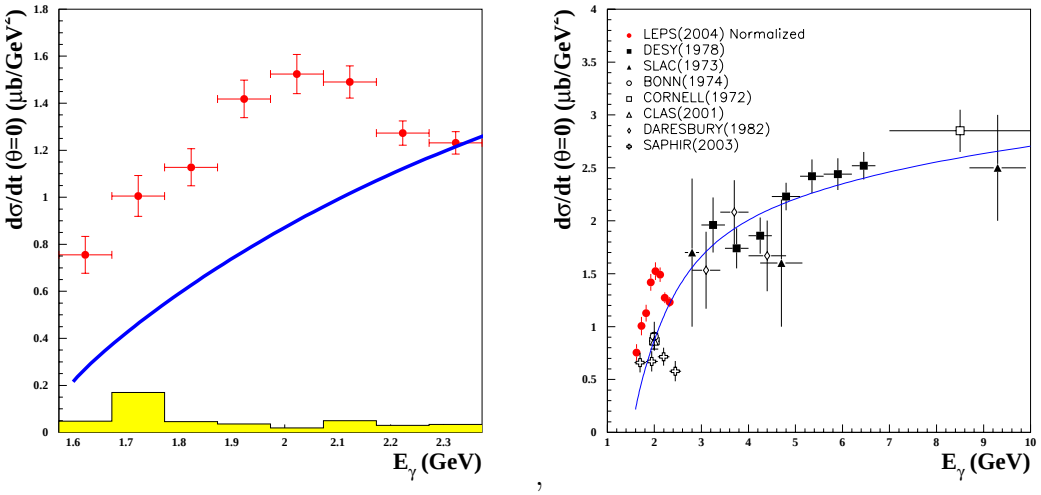

Figure 5.3: Differential cross section at $\tilde{t} = 0$ GeV^2 ($\theta_\phi^{CM} = 0°$). The closed circle indicates the LEPS data. The solid curve shows the prediction from the model (the Pomeron + the pseudo scalar exchanges)[18]. The LEPS data points were normalized at 2.327 GeV. The other data points are taken from [7, 22, 65, 25, 13, 64]

Decay angular distribution

By using the experimental results of the decay angular distributions, some of ϕ photoproduction mechanisms to explain the peaking structure in the cross sections are possible to be excluded. We measured the decay angular distributions at two different energies of $1.973 < E_\gamma < 2.173$ GeV and $2.173 < E_\gamma < 2.373$ GeV. Note that the measured energy range of $1.973 < E_\gamma < 2.173$ GeV corresponds to the energy just around the peak of the cross section at $\tilde{t} = 0$, and the range of $2.173 < E_\gamma < 2.373$ GeV is off from the peak.

The spin density matrix element, $\tilde{\rho^1}(= \rho^0_{00})$ (Table 4.10) is found to be small and to have no energy dependence. As discussed in Section 1.2, ρ^0_{00} is sensitive to the single helicity flip amplitude. The tensor-meson exchange, such as f'_2 exchange, is predicted to introduce a large helicity flip as shown in Fig. 1.4($\rho^0_{00} > 0.3$ at E_γ=2.2 GeV). The experimental results give a constraint that the contribution of the tensor exchange predicted by Ref. [19] to be small. The $\tilde{\rho^3}$ was positive and there was no significant difference between $2.173 < E_\gamma < 2.373$ GeV and $1.973 < E_\gamma < 2.173$ GeV. The positive value for $\tilde{\rho^3}$ excluded the case of a dominant contribution from the unnatural parity exchange (π, η exchange) predicted by Ref. [6] at this energy regime. However, the measured $\tilde{\rho^3}(= 1/2(\rho^1_{1-1} - \mathrm{Im}\rho^2_{1-1}))$ was not close to +0.5 which was a prediction for pure natural parity exchange. This implies that there are finite contributions from the unnatural parity exchange. The relative contribution between the natural parity exchange and the unnatural parity exchange was the same for the two energy ranges since there was no energy dependence of $\tilde{\rho^3}$. As mentioned above, a contribution from the Pomeron decreases with decreasing energy, and the contributions from the pseudo scalar exchange increase. In order to keep the relative contribution same, an additional contribution with natural parity exchange is needed.

The conclusion of this simple analysis based on the naive considerations of spin and parity of the exchanged particle was further confirmed by a comparison with the more realistic model [18] based on the the Pomeron exchange and the π/η exchange amplitudes. Fig. 5.4 shows comparisons of data with the model. The model described the data reasonably well. But, as discussed in the previous section, the same model failed to explain the peaking structure of the cross sections around $E_\gamma \sim 2GeV$. This suggests a possible non-conventional mechanism of ϕ photoproduction has the spin properties similar to those of the Pomeron exchange process.

The peaking structure in the cross sections and the independence of relative contributions from natural-parity and unnatural-parity exchange can be interpreted as a possible presence of an additional natural parity exchange in ϕ photoproduction near the threshold.

The extraction of the absolute cross sections in this data is necessary to check consistency with the previous data and to develop the theoretical framework, unambiguously. In the future, new measurements of energy dependence of the forward angle cross sections at higher energies ($E_\gamma > 2.4$ GeV) will be important to confirm the peaking structure.

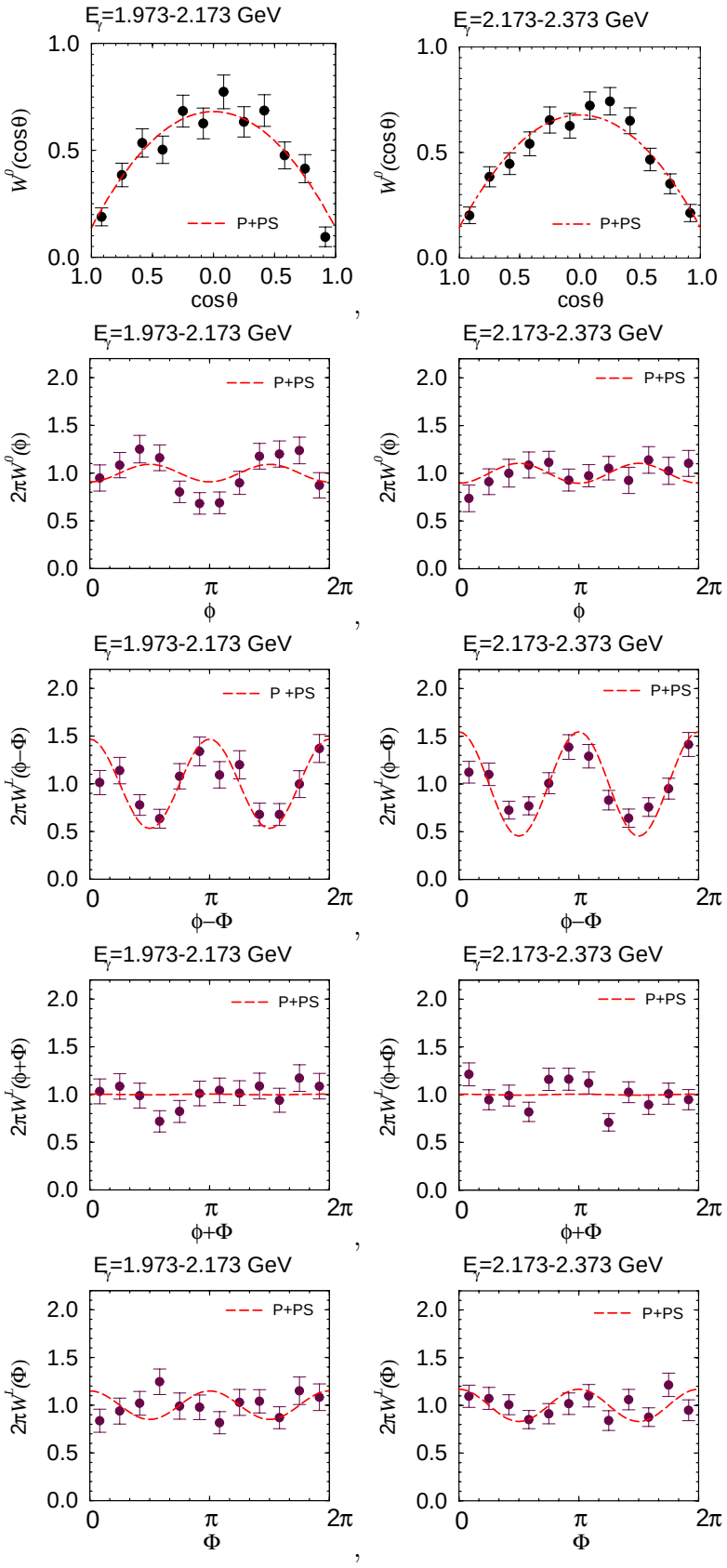

Figure 5.4: Decay angular distributions for 2.173< E_γ <2.373 GeV(left plot), 1.973< E_γ <2.173 GeV (right plot) in -0.2< $\tilde{t}$. Curves represent predictions from the Pomeron exchange (P) and the π/η exchange (PS). The predictions are given by Ref. [18]

Chapter 6

Summary

The photoproduction of ϕ meson has been studied in the energy range from the production threshold to E_γ =2.4 GeV using the linearly-polarized photon beam at LEPS/SPring-8.

Thanks to the OZI suppression of the conventional meson exchanges in the t-channel, the energy dependence of the differential cross sections and the spin-density matrix elements are sensitive to the possible non-conventional production mechanisms, such as the glueball exchange. The measurements at forward angles near the threshold provides a good opportunity to search for such mechanisms.

The decay angular distribution also provides useful information on the production mechanisms. Photoproduction using a linearly polarized photon beam is represented by the nine spin-density matrix elements. The spin-density matrix elements are bilinear combinations of scattering amplitude. The angular correlation between the K-meson emission angle and the polarization vector of the photon is sensitive to the relative contribution from the natural-parity exchange and the unnatural-parity exchange.

The elastic photoproduction of ϕ mesons from the liquid hydrogen target were identified by the exclusive measurement with the LEPS magnetic spectrometer in the K^+K^- decay mode. Highly polarized photon beam was provided by the backward Compton scattering of the laser photon off the 8 GeV electrons in the storage ring. The foundations of the present successful measurements and analysis, such as the programs for the track reconstruction, the beam energy reconstruction, the particle identification and the Monte Carlo simulator have been developed in this work.

In total, about 5000 ϕ events have been accumulated in the experiment from December, 2000 to June, 2001. The t slope of the differential cross sections was found to be independent of the beam energy near the threshold. The energy dependence of the differential cross sections at $\tilde{t} = 0$ GeV^2 ($\theta_\phi^{CM} = 0^\circ$) was measured. We observed the peaking structure of the ϕ-meson photoproduction cross section near $E_\gamma = 2.0$ GeV. The model based on the Pomeron exchange and the pseudo scalar exchange failed to give such a peaking structure.

We measured the decay angular distribution of the ϕ meson near the threshold with linearly polarized photon for the first time. The five spin-density matrix elements were extracted from projected angular distributions. It turned out that the helicity conserving amplitude were dominant at forward angles. A constraint was given for the contributions from the helicity non-conserving processes, such as the tensor (f_2') exchange and the nucleon resonance production. As a result, the helicity non-conserving processes are found to be small at forward angles. The

angular correlation between the K^+ and the polarization vector of the photon showed that the contribution from the natural-parity exchanges is larger than that from the unnatural-parity exchanges, such as π and η meson exchange. No significant energy dependence of the angular distributions was observed between $1.973 < E_\gamma < 2.173$ GeV and $2.173 < E_\gamma < 2.373$ GeV.

The peaking structure in the cross section and the independence of relative contributions from the natural-parity and the unnatural-parity exchange can be interpreted as a possible presence of an additional natural-parity exchange process in the ϕ photoproduction near the threshold.

The absolute values of cross sections, which were not presented in this thesis, are important to confirm the consistency with the previous data and the theoretical predictions. In the future, new measurement at higher energies ($E_\gamma > 2.4$ GeV) will be important to establish the non-monotonical structure of the cross section near the threshold.

Appendix A

The correction of photon flux

The energy spectrum of the photon beam is not uniform. Therefore, energy dependence of the observed ϕ yield depends not only due to energy dependence of the cross section , but also due to ununiformity of the photon energy spectrum. An analysis to obtain a correction factor to correct relative difference of the photon flux in different photon energies are described in this section. The analysis was based on the information on the tagging counter.

A.1 Efficiency of the tagging counter

A counter efficiency of the plastic scintillator of the tagging counter was measured by using the electron tracks which go through the overlapped region of adjacent scintillators.

The tracks which at least have hits on upstream and downstream SSDs and all of scintillators, except for the scintillator which we are looking at, were selected. A response of the scintillator whether it provide a valid signal was checked. The efficiency was measured as a ratio of number of event with a valid scintillator hit to number of total selected events. The efficiency depends on run period. The run dependence of the efficiency is shown in Fig.A.1. The efficiency had been gradually decreased from December,2000 to February, 2001. Main source of inefficiency is due to lower pulse height of the scintillator signal. The efficiency has kept high again after March, 2001 when the discriminator threshold was lowered.

The counter efficiency of the SSD was measured by similar manner as that of the scintillator. It was found out that the efficiency was close to 100% in all run periods, except for the some of problematic strips. There are dead strips which do not make any signal make dead region. The efficiency of strips next to the dead strip also decreased to 97-98 % because of an imperfect collection of the deposited-charge associated with energy loss by the electron track. Although the counter efficiency of the SSD is not perfect over all region, tracks which went through the inefficient strip were saved by an algorithm to save tracks which passed through one of the dead strip, but left a signal in another SSD plane. Therefore, the overall efficiency of the tagging counter was determined by the efficiency of the plastic scintillators.

A.2 Relative strength of multiline laser

The laser beam consists of three major lines with their wavelength λ =363.8, 351.1 and 333.6 nm. The energy spectrum of the photon beam is a convolution of three spectra for different wavelength. A relative strength of three components was obtained by fitting to a tagger spectrum. The tagger-triggered data which was taken by requiring the tagger signal only was used to obtain the unbiased-energy distribution of the photon. Tight event selections were applied to select the clean sample. The selections are as follows: (1) number of SSD track is required to be 1. The SSD track is defined as a pair of SSD hits in the upstream SSD and the downstream SSD with a angle which is consistent with the good electron track. (2) the SSD track must have a valid signal in corresponding scintillator(s). The observed distribution is shown in Fig. A.2(a). This distribution is distorted by the inefficiency of the tagger scitillator. Fig. A.2(b) represents the efficiency of the tagger scintillator as a function of SSD strip in this data. A correction for the inefficiency was made to Fig. A.2(a). A fit to the efficiency-corrected distribution, Fig. A.2(c), was examined by a function which consists of three components of the Compton scattering cross section [29] convoluted by the resolution:

$$P_1(\frac{d\sigma}{dE_\gamma}(363.8nm) + P_2\frac{d\sigma}{dE_\gamma}(351.1nm) + P_3\frac{d\sigma}{dE_\gamma}(333.6nm)) \otimes \frac{1}{\sqrt{2\pi\sigma_\gamma^2}}\int dE'_\gamma e^{\frac{-(E'_\gamma - E_\gamma)^2}{2\sigma_\gamma^2}} \quad \text{(A.1)}$$

, where P_1,P_2,P_3 and $P_4 = \sigma_\gamma$ are fitting parameters and beam energy E_γ was converted to SSD position through the inverse function of the E_γ calibration function. The fitting range was limited to a region of three Compton edges (250-300 ch) because it was not possible to fit the whole distribution with Eq. A.1 due to backgrounds from electro-magnetic shower at the accelerator wall. The results of the fit is shown by the solid line in Fig. A.2(c). A dashed curve indicates an extrapolation of the fitting function to the lower E_γ side. A close-up plot around Compton edges are shown in Fig. A.2(d). The parameters P_2 and P_3 which represent relative strength of multilines, were used in the following anal-sys.

A.3 Efficiency of the selection of valid tagger hit

In the tagger analysis, signals for all of the scintillators associated with the SSD track were required. The efficiency for this condition (full tagger hits) are referred as ϵ_{AND}. On the other hand, photon flux was measured by the scintillator signal where it is not necessary to have signals for all corresponding scintillators when the recoiled electron passed the overlapped region of the scintillators. The efficiency for this condition is referred as ϵ_{OR}. The tagger signal was required in the trigger condition. Keeping this in mind, the efficiency of the selection of the valid tagger hit (Section 3.3.4) is therefore $\epsilon_{tagcut} = \epsilon_{AND}/\epsilon_{OR}$.

In order to obtain the beam energy spectrum, the efficiency of the tagger was averaged over whole run periods weighted by the number of tagged photons (N_γ):

$$\epsilon_{OR} = \frac{\sum_i \epsilon_{OR}(i) N_\gamma(i)}{\sum_i N_\gamma(i)} \quad \text{(A.2)}$$

$$\epsilon_{AND} = \frac{\sum_i \epsilon_{AND}(i) N_\gamma(i)}{\sum_i N_\gamma(i)} \quad \text{(A.3)}$$

, where i runs over all run number. The number of the tagged photon flux for the tagger acceptance ($E_\gamma = 1.5 - 2.9$ GeV) was measured by the scaler counts which were corrected for the dead time of the scaler module and an accidental coincidence of multiple electron hits in the tagger within a timing gate width [66]. The average tagger efficiencies as a function of photon energy are shown in Fig. A.3(a) and (b). The photon energy spectrum after the requirement of valid tagger hit was obtained by multiplying Eq. A.1 by $\epsilon_{OR}\epsilon_{tagcut} = \epsilon_{AND}$ (Fig. A.3(c)).

A.4 Correction for the energy dependence of the photon flux

The photon energy dependence of the differential cross section was measured in a 0.1 GeV step from the production threshold (see Section 4.1). Fraction of events in a certain E_γ bin (ω_γ) was calculated by the area of the energy spectrum (Fig. A.3(c))) in which efficiency of the tagging counter (ϵ_{OR}) and efficiency of the tagger selection cut (ϵ_{tagcut}) were taking into account. The average efficiencies (ϵ_{OR},ϵ_{AND}) and the fraction for each E_γ bin are summarized in Table A.1.

The difference of photon flux in the yield of ϕ photoproduction was corrected by the factor $1/\omega_\gamma$ each E_γ bin.

Table A.1: The tagger efficiencies and relative weights of the photon flux

Photon energy (GeV)	ϵ_{OR}	ϵ_{AND}	fraction(ω_γ)
1.573 - 1.673	0.9380	0.9380	0.0758
1.673 - 1.773	0.9740	0.9165	0.0805
1.773 - 1.873	0.9490	0.9490	0.0886
1.873 - 1.973	0.9676	0.9299	0.0998
1.973 - 2.073	0.9552	0.9515	0.1148
2.073 - 2.173	0.9841	0.9166	0.1220
2.173 - 2.273	0.9313	0.9190	0.1478
2.273 - 2.373	0.9469	0.9073	0.1392
2.373 - 2.473	0.9644	0.9391	0.0537
2.473 - 2.573	0.9885	0.8963	0.0029

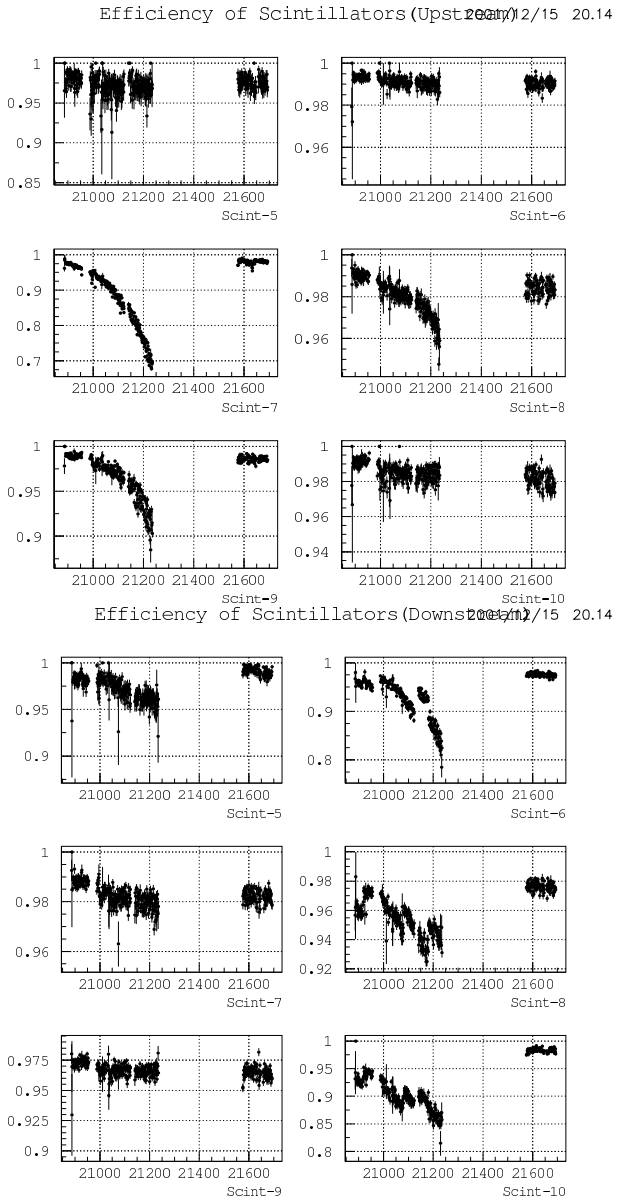

Figure A.1: Efficiency of plastic scintillator. Top plots are for up-stream layer, bottom plots are for down-stream layer.

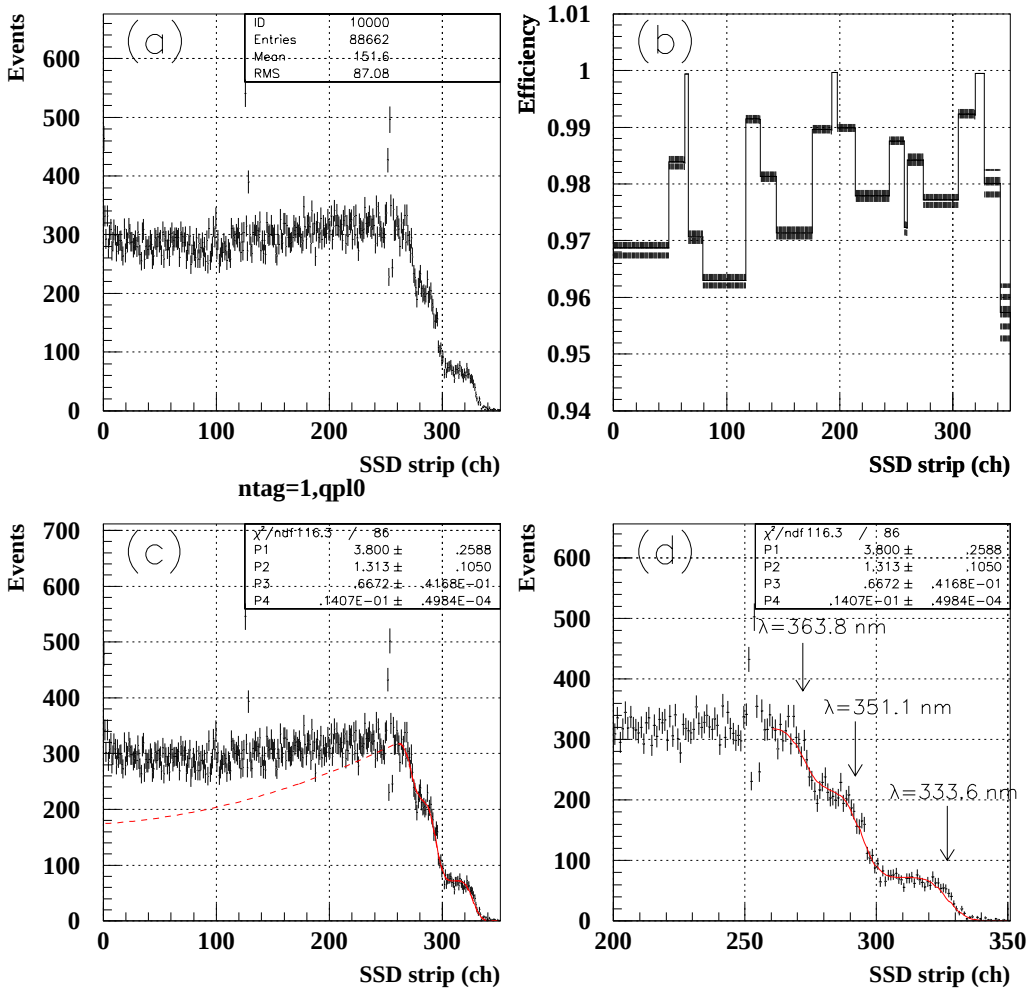

Figure A.2: (a) The tagger SSD hit distribution for the tagger-triggered data. (b) Efficiency of the scintillator as a function of SSD strip. (c) The efficiency-corrected SSD hit distribution. (d) The efficiency-corrected SSD hit distribution near the Compton edges. Dashed curve indicates an extrapolation of the fitting function.

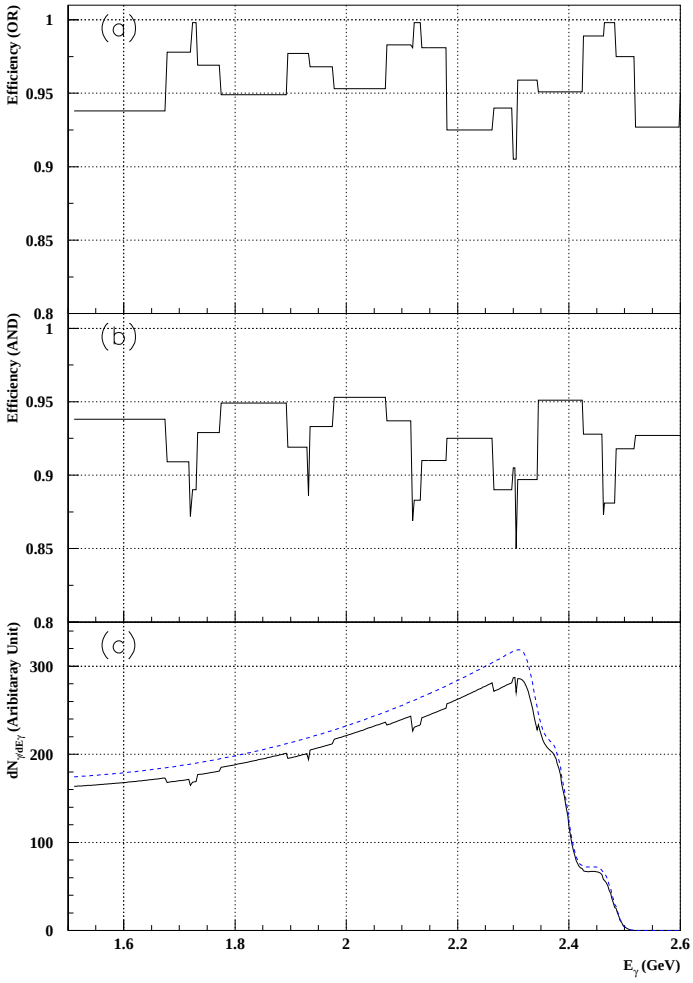

Figure A.3: (a) The tagger efficiency (OR) as a function of photon energy (b) the tagger efficiency (AND) as a function of photon energy (c) the simulated energy spectrum for the tagged photons

Appendix B

Supplementary studies for the acceptance determination

B.1 Applicability of the acceptance

Applicability of the acceptance to the real data was checked for cases when the slope parameter and the spin density matrix elements were different from those used for the acceptance calculation. To check this, a set of Monte Carlo data with different choice of parameters was generated. Table. B.1 lists choices of the slope parameter b and the unpolarized-part of the spin density matrix elements ρ^0. The parameter choices 5 and 45 are the same as those used in the acceptance calculation. There is a physical boundary for ρ^0's due to the unitarity of the scattering amplitude [23]. Within the physical boundary of ρ^0, the list covers whole region of parameter space for ρ^0_{10} and ρ^0_{1-1} with $0 \leq \rho^0_{00} \leq 0.2$. The number of events in the Monte Carlo simulation were much larger than those in real data to check the effect purely due to the acceptance.

The Monte Carlo data listed in Table B.1 were processed in the same analysis flow as those in real data (details will be given in Section 4.1). The $t + |t|_{min} (= \tilde{t})$ distribution after the acceptance correction was fitted by $n_0 \exp(b\tilde{t}) a(E_\gamma, \tilde{t})$, where n_0 and b are parameters in the fit. $a(E_\gamma, \tilde{t})$ is a correction factor for kinematical limit (see Section 4.1 for detail). The parameters obtained from the fit were compared with the exact inputs of Monte Carlo data. Fig. B.1 (a) shows a deviation of observed n_0 from the input value as a function of the parameter choice in 2.173< E_γ <2.373 GeV. A reproducibility of the slope parameter b is shown in Fig. B.1 (b). Similar results for lower energies are shown in Figs. B.2, B.3 and B.4. The n_0 reproduced within ∼10% precision in the worst case (parameter choice 25). The slope b were reproduced within a range of +0.6< $b_{fit} - b_{in}$ < -0.8 GeV^2. When the parameters are close to the ones in acceptance calculation, the agreement are much better.

In the next step, the reproducibilities were checked with lower statistics which is similar to the real data. Many sets of Monte Carlo data with the same statistics and the same conditions were generated to reduce statistical fluctuation for a single Monte Carlo data. Fig. B.5 demonstrates an example of this study. 28 runs of Monte Carlo data were generated with the parameter set 5 at 2.173< E_γ <2.373 GeV. Each run contains 1198 ϕ reconstructed events. The fitting results for each run are shown in Fig. B.5(a) and (b) where n_0 was normalized to 1. A solid line indicates the inputs of Monte Carlo simulation. Means of obtained parameters were

Table B.1: Choices of parameters for the applicability check

Parameter choice	$b(\mathrm{GeV}^{-2})$	ρ^0_{00}	ρ^0_{10}	ρ^0_{1-1}	Parameter choice	$b(\mathrm{GeV}^{-2})$	ρ^0_{00}	ρ^0_{10}	ρ^0_{1-1}
1	3.0	0.0	0.1	-0.2	25	3.0	0.2	0.2	-0.2
2	3.0	0.0	0.1	-0.1	26	3.0	0.2	0.2	-0.1
3	3.0	0.0	0.0	-0.2	27	3.0	0.2	0.1	-0.2
4	3.0	0.0	0.0	-0.1	28	3.0	0.2	0.1	-0.1
5	3.0	0.0	0.0	0.0	29	3.0	0.2	0.1	0.0
6	3.0	0.0	0.0	0.1	30	3.0	0.2	0.1	0.1
7	3.0	0.0	0.0	0.2	31	3.0	0.2	0.1	0.2
8	3.0	0.0	0.1	-0.2	32	3.0	0.2	0.0	-0.2
9	3.0	0.0	0.1	-0.1	33	3.0	0.2	0.0	-0.1
10	3.0	0.1	0.1	-0.2	34	3.0	0.2	0.0	0.0
11	3.0	0.1	0.1	-0.1	35	3.0	0.2	0.0	0.1
12	3.0	0.1	0.1	0.0	36	3.0	0.2	0.0	0.2
13	3.0	0.1	0.1	0.1	37	3.0	0.2	-0.1	-0.2
14	3.0	0.1	0.1	0.2	38	3.0	0.2	-0.1	-0.1
15	3.0	0.1	0.0	-0.2	39	3.0	0.2	-0.1	0.0
16	3.0	0.1	0.0	-0.1	40	3.0	0.2	-0.1	0.1
17	3.0	0.1	0.0	0.0	41	3.0	0.2	-0.1	0.2
18	3.0	0.1	0.0	0.1	42	3.0	0.2	-0.2	-0.2
19	3.0	0.1	0.0	0.2	43	3.0	0.2	-0.2	-0.1
20	3.0	0.1	-0.1	-0.2	44	2.0	0.0	0.0	0.0
21	3.0	0.1	-0.1	-0.1	45	3.0	0.0	0.0	0.0
22	3.0	0.1	-0.1	0.0	46	4.0	0.0	0.0	0.0
23	3.0	0.1	-0.1	0.1	47	5.0	0.0	0.0	0.0
24	3.0	0.1	-0.1	0.2	48	6.0	0.0	0.0	0.0

found to be $n_0 = 1.003 \pm 0.006$ and $b = 3.04 \pm 0.05$ GeV^{-2}, respectively (Fig. B.5(c),(d))). The χ^2/ndf for the fit in each Monte Carlo data are shown in Fig. B.5. The obtained parameters are consistent with the inputs of Monte Carlo. Similarly, no significant deviation was found in Monte Carlo data with different E_γ bins.

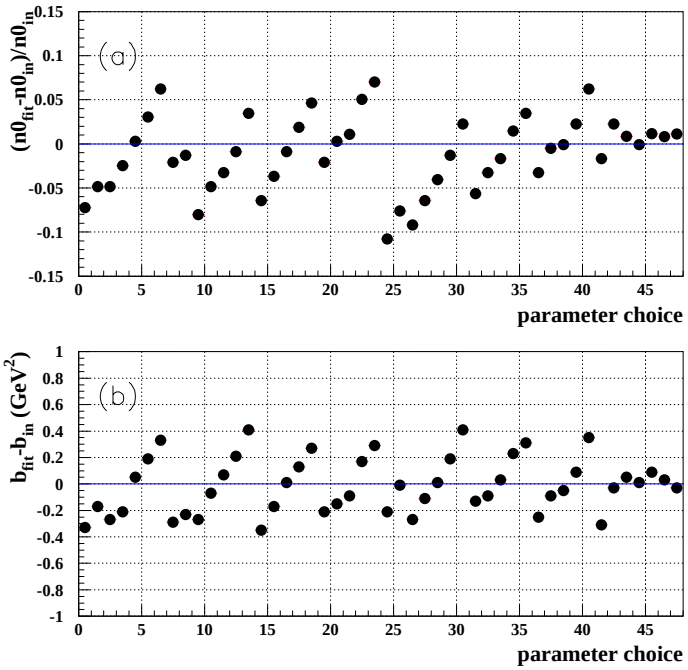

Figure B.1: Reproducibility of t distribution in Monte Carlo data. Deviation of fitting parameters from the inputs (a) intercept n_0, (b) slope b for 2.173< E_γ <2.373

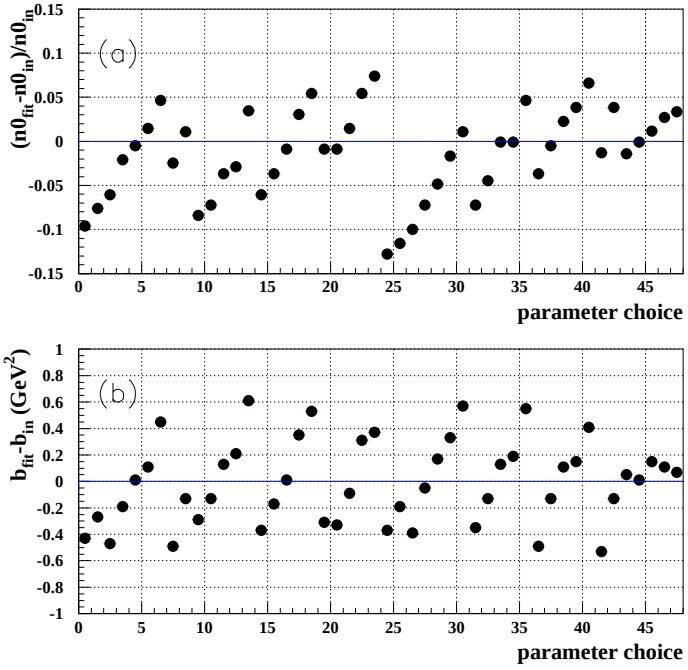

Figure B.2: Reproducibility of t distribution in Monte Carlo data. Deviation of fitting parameters from the inputs (a) intercept n_0, (b) slope b for 1.973< E_γ <2.173

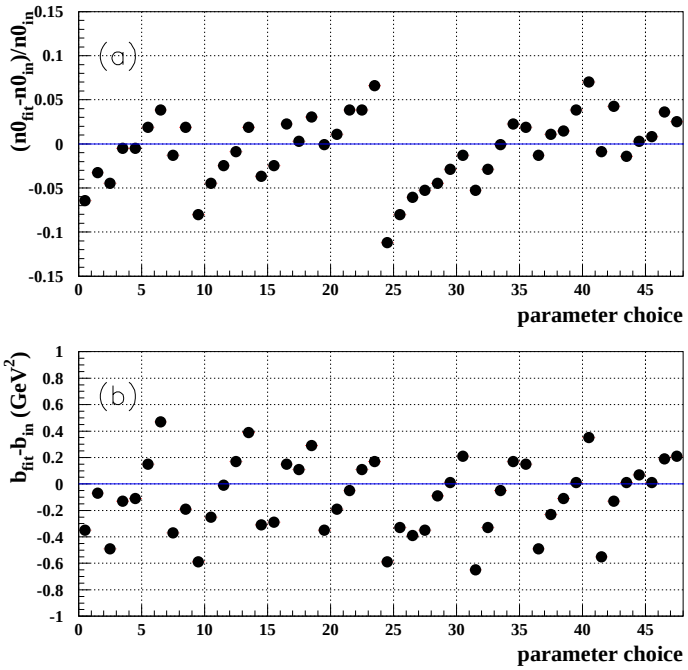

Figure B.3: Reproducibility of t distribution in Monte Carlo data. Deviation of fitting parameters from the inputs (a) intercept n_0, (b) slope b for 1.773< E_γ <1.973

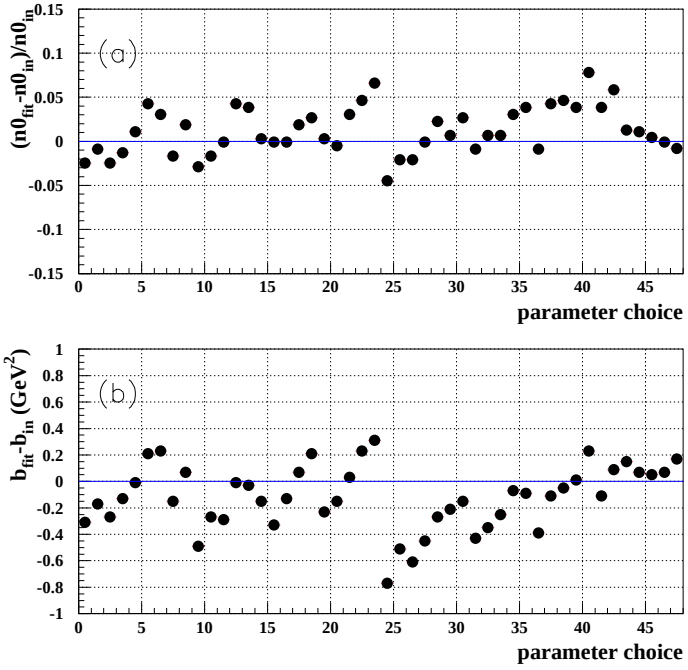

Figure B.4: Reproducibility of t distribution in Monte Carlo data. Deviation of fitting parameters from the inputs (a) intercept n_0, (b) slope b for 1.573< E_γ <1.773

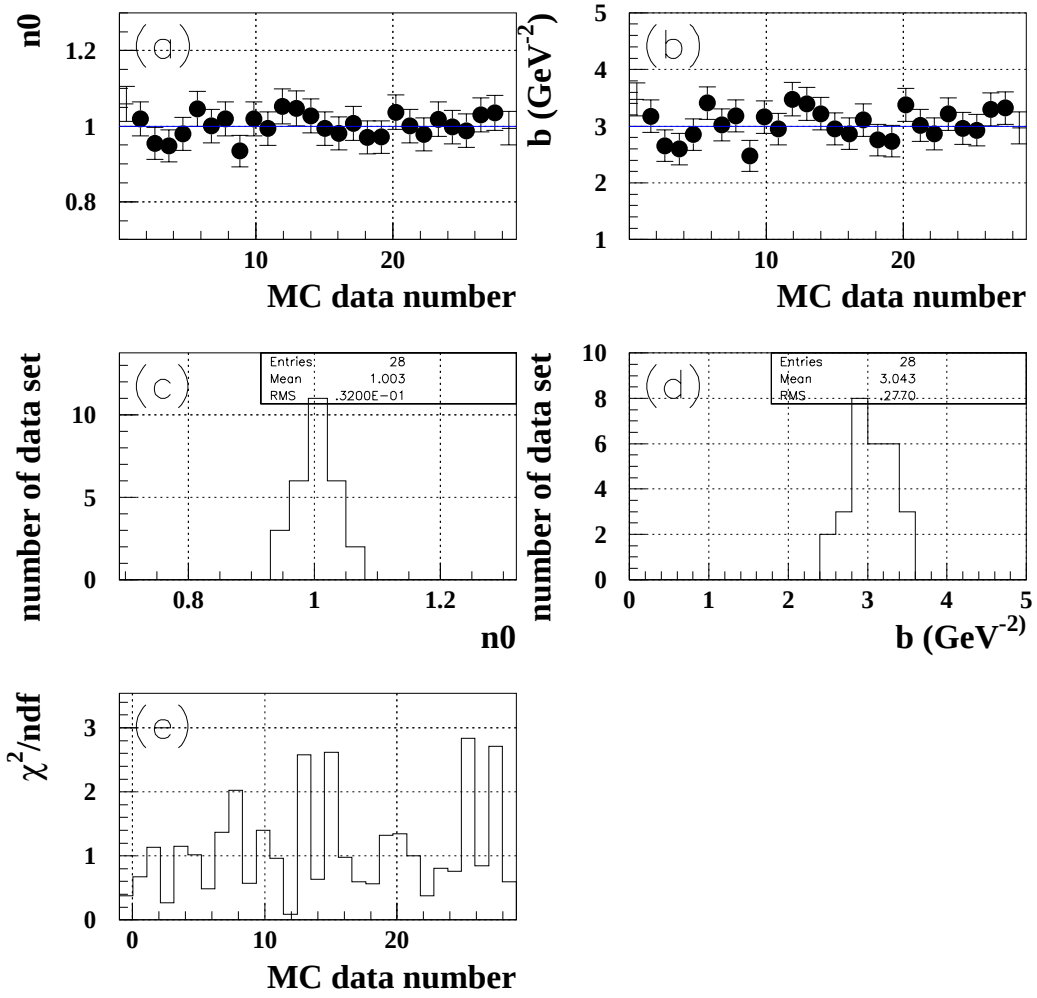

Figure B.5: Reproducibility of t distribution in Monte Carlo data with low statistics.

B.2 Energy dependence of the acceptance

The acceptance depends on photon energy, i.e. the acceptance increase with energy for K^+K^- mode and it decrease with energy for $K^{\pm}p$ modes. In order to measure the energy dependence of the cross section, the energy dependence of the acceptance must be calculated correctly. Fig. B.6 show the acceptance as a function of E_γ for different reconstruction modes (KKp,K^+K^-,K^-p and K^+p). Each points corresponds to the acceptance for $(E_\gamma - 0.05) < E_\gamma < (E_\gamma + 0.05)$ GeV. The open square indicates the acceptance for the most forward angle ($-0.1 < \tilde{t} < 0.0$ GeV^2), circles and triangles represents the acceptance for $-0.2 < \tilde{t} < -0.1$ GeV^2 and $-0.3 < \tilde{t} < -0.2$ GeV^2, respectively. The energy dependence of the acceptance is found to be smooth, except for a steep change for $K^{\pm}p$ modes near threshold. No strong structure around E_γ= 2 GeV which corresponds to the peak of the bump in the cross section is seen.

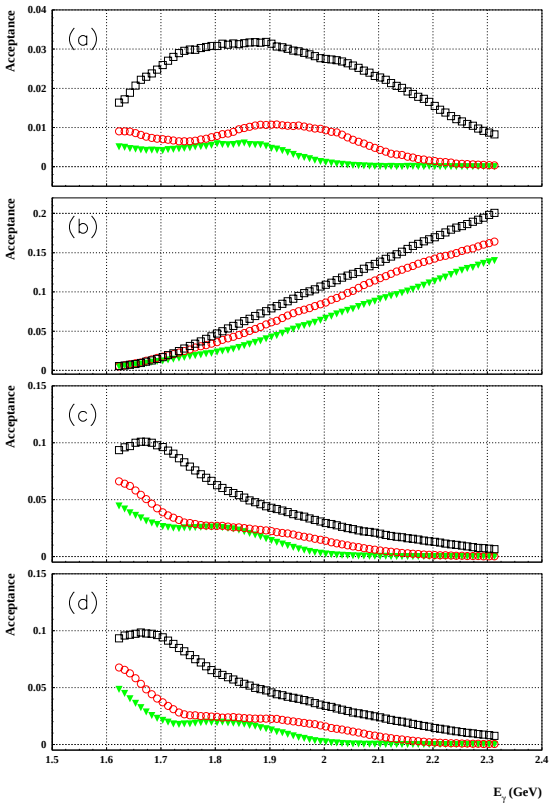

Figure B.6: Acceptance as a function of E_γ for (a) K^+K^-pK mode, (b) K^+K^- mode, (c) K^-p mode, (d) K^+p mode. Error bars for horizontal direction, corresponding to full width of the bin, are 0.05 GeV which are not shown in these plots.

B.3 The acceptance for HZ+VT data

The LEPS spectrometer is wider in horizontal direction than in vertical direction. Therefore, the acceptances for data taken with vertical polarization (VT) and the one with horizontal polarization (HZ) are different and strongly depends on the polarization parts of the spin density matrix elements (ρ^1 and ρ^2). However, the acceptance for a sum of VT + HZ data is almost independent of the polarization effects since there is an approximate cancellation of the polarization effects between VT and HZ data at forward angles where z-axis of the GJ frame is approximately same as the direction of incoming photon in laboratory frame. This can be understood by considering that full angular distribution (Eq. 1.1) has $\cos(2\Phi)$ and $\sin(2\Phi)$ dependences, thus the polarized parts of angular distribution (W^1, W^2) is removed by taking a sum of Eq. 1.1 with $\Phi \sim 0$ degree (HZ) and $\Phi \sim 90$ degree (VT). It results in unpolarized angular distribution (W^0). However, in general, z-axis is different from the beam direction at finite angles, and the beam profiles for VT and HZ polarized beam are different. Thus, it is not trivial to assume the perfect cancellation of the polarization effects in the acceptance for HZ and VT data. We used Monte Carlo simulation to check the acceptance for HZ+VT data.

Table. B.2 shows results of a Monte Carlo test for the acceptance for HZ+VT data. The number of accepted events were checked for four choices (set A-D) of the spin density matrix elements (ρ^1_{1-1} and $\mathrm{Im}\rho^2_{1-1}$) which controls relative ratio of natural and unnatural parity exchange, i.e.

$$\begin{aligned}
\text{Set A} \quad &, \quad \rho^1_{1-1} = -\mathrm{Im}\rho^2_{1-1} = 0.3 \\
\text{Set B} \quad &, \quad \rho^1_{1-1} = -\mathrm{Im}\rho^2_{1-1} = 0.5 \\
\text{Set C} \quad &, \quad \rho^1_{1-1} = -\mathrm{Im}\rho^2_{1-1} = -0.5 \\
\text{Set D} \quad &, \quad \rho^1_{1-1} = -\mathrm{Im}\rho^2_{1-1} = 0.0
\end{aligned}$$

In each set of data, total number of generated events was same each other. Therefore, the difference of these numbers are purely due to the different acceptance. The number of events in KK mode and K^-p were checked in two different energy ranges and three different $\tilde{t}$ ranges. It was confirmed that the number of accepted events for HZ+VT sample was independent of assumption of ρ^1_{1-1} and $\mathrm{Im}\rho^2_{1-1}$, while the number of events for un-summed sample (HZ and VT) varies significantly.

Table B.2: Number of accepted events in Monte Carlo simulation

KK mode, $E_\gamma > 2.2\text{GeV}, -0.2 < \tilde{t} < 0.\text{GeV}^2$ (100000 events)

Set	Natural pari. exch.	Unnatural pari. exch.	HZ	VT	HZ+VT	(HZ+VT)/(Set A)
A	80 %	20 %	16822	15673	32495	1.0000
B	100 %	0 %	17129	15209	32338	0.9952 ±0.0055
C	0 %	100 %	15200	17135	32335	0.9951 ±0.0055
D	50%	50 %	16295	16370	32665	1.0052 ±0.0056

KK mode, $E_\gamma > 2.2\text{GeV}, -0.4 < \tilde{t} < -0.2\text{GeV}^2$ (200000 events)

Set	Natural pari. exch.	Unnatural pari. exch.	HZ	VT	HZ+VT	(HZ+VT)/(Set A)
A	80 %	20 %	13616	11111	24727	1.0000
B	100 %	0 %	14341	10432	24773	1.0019 ±0.0064
C	0 %	100 %	10307	14527	24834	1.0043 ±0.0064
D	50%	50 %	12456	12298	24754	1.0011 ±0.0064

KK mode, $E_\gamma > 2.2\text{GeV}, -0.6 < \tilde{t} < -0.4\text{GeV}^2$ (400000 events)

Set	Natural pari. exch.	Unnatural pari. exch.	HZ	VT	HZ+VT	(HZ+VT)/(Set A)
A	80 %	20 %	10213	8383	18596	1.0000
B	100 %	0 %	11024	7800	18824	1.0123 ±0.0074
C	0 %	100 %	7607	10759	18366	0.9876 ±0.0073
D	50%	50 %	9378	9328	18706	1.0059 ±0.0074

KK mode, $E_\gamma < 1.8\text{GeV}, -0.2 < \tilde{t} < 0.\text{GeV}^2$ (400000 events)

Set	Natural pari. exch.	Unnatural pari. exch.	HZ	VT	HZ+VT	(HZ+VT)/(Set A)
A	80 %	20 %	12892	9174	22066	1.0000
B	100 %	0 %	14112	7724	21836	0.9895 ±0.0094
C	0 %	100 %	7889	13989	21878	0.9914 ±0.0094
D	50%	50 %	11051	10917	21968	0.9955 ±0.0094

KK mode, $E_\gamma < 1.8\text{GeV}, -0.4 < \tilde{t} < 0.2\text{GeV}^2$ (1500000 events)

Set	Natural pari. exch.	Unnatural pari. exch.	HZ	VT	HZ+VT	(HZ+VT)/(Set A)
A	80 %	20 %	8370	5147	13517	1.0000
B	100 %	0 %	9463	3872	13335	0.9865 ±0.012
C	0 %	100 %	3759	9354	13113	0.9701 ±0.011
D	50%	50 %	6684	6536	13220	0.9780 ±0.011

$K^- p$ mode, $E_\gamma < 1.8\text{GeV}, -0.2 < \tilde{t} < 0.0\text{GeV}^2$ (400000 events)

Set	Natural pari. exch.	Unnatural pari. exch.	HZ	VT	HZ+VT	(HZ+VT)/(Set A)
A	80 %	20 %	24132	22573	46705	1.00000
B	100 %	0 %	24520	22122	46642	0.99865 ± 0.0065
C	0 %	100 %	22186	24451	46637	0.99854 ± 0.0065
D	50%	50 %	23342	23504	46846	1.00302 ± 0.0066

$K^- p$ mode, $E_\gamma < 1.8\text{GeV}, -0.4 < \tilde{t} < -0.2\text{GeV}^2$ (1500000 events)

Set	Natural pari. exch.	Unnatural pari. exch.	HZ	VT	HZ+VT	(HZ+VT)/(Set A)
A	80 %	20 %	47598	42979	90577	1.00000
B	100 %	0 %	49367	41425	90792	1.00237 ± 0.0047
C	0 %	100 %	41537	49318	90855	1.00307 ± 0.0047
D	50%	50 %	45280	45447	90727	1.00166 ± 0.0047

Appendix C

Supplementary plots and tables for the signal sample

C.1 K^+K^- invariant mass distribution as a function of $\tilde{t}$

Some of $\tilde{t}$ bins at larger angles were not used in the analysis because number of ϕ event was too small, or separation of signal from backgrounds was difficult. In each E_γ and $\tilde{t}$ bin, observed K^+K^- mass distribution in real data were compared with background shape for the non-resonant KKp given by the Monte Carlo simulation to check whether the background shape resembles the distribution of the ϕ signal or not. Plots in Fig. C.1 show the K^+K^- invariant mass distribution as a function of $\tilde{t}$ bin in E1 bin in real data. The ϕ selection cuts, except for the invariant mass cut, were required. The circle mark ($\bigcirc$) indicates that that bin was used in the analysis. The bins with cross mark ($\times$) were not used. For the comparison of the background shape, the invariant mass distribution for non-resonant KKp background given by Monte Carlo are shown in Fig. C.2. Similar plots for different energies are shown in Figs. C.3, C.4 for E2, Figs. C.5, C.6 for E3, Figs. C.7, C.8 for E4, Figs. C.9, C.10 for E5, Figs. C.11, C.12 for E6, Figs. C.13, C.14 for E7, Figs. C.15, C.16 for E8.

Data of all small $\tilde{t}$ bins passed this criteria. But distinction between the ϕ signal and backgrounds was more difficult in lower energies, for example T6-T9 bin of E7 (Figs. C.13) and T5 bin of E8 (Figs. C.15) because available phase space volume for these $\tilde{t}$ bin is too small to see signature of ϕ events, therefore they were rejected.

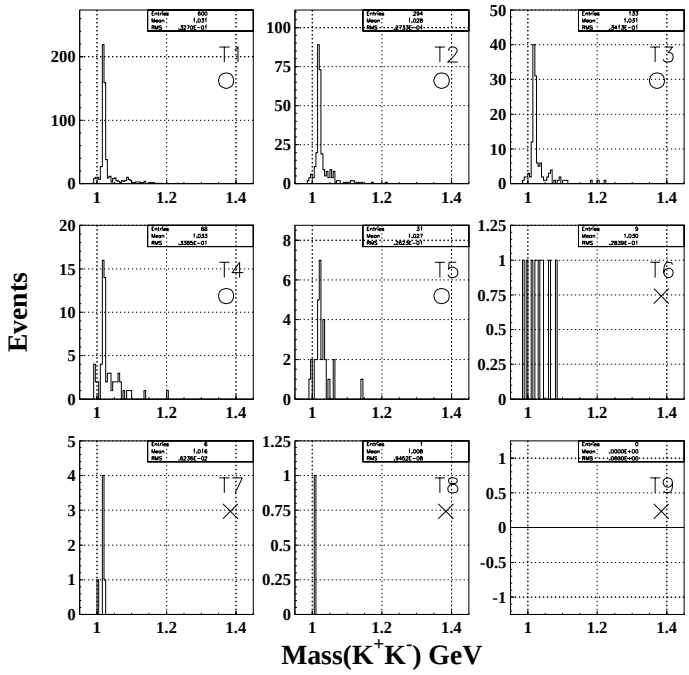

Figure C.1: The K^+K^- mass distribution for E1 bin in real data.

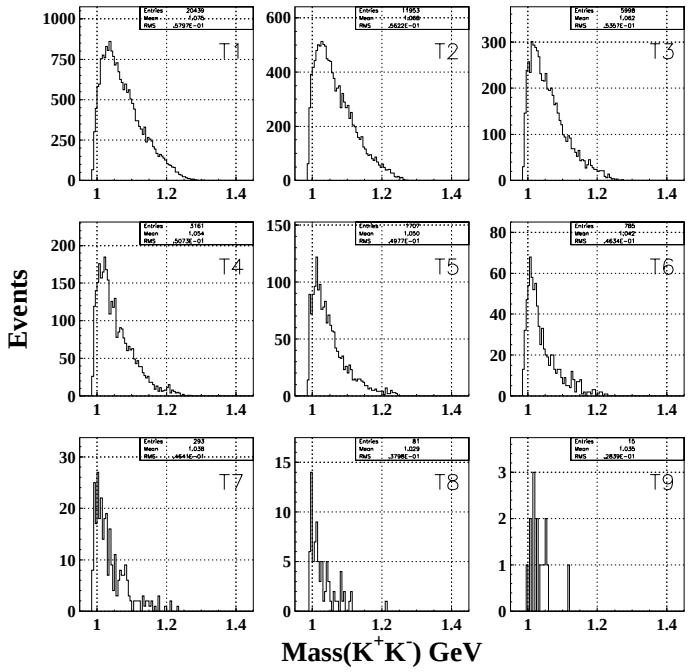

Figure C.2: The K^+K^- mass distribution for non-resonant KKp background for E1 bin in Monte Carlo simulation.

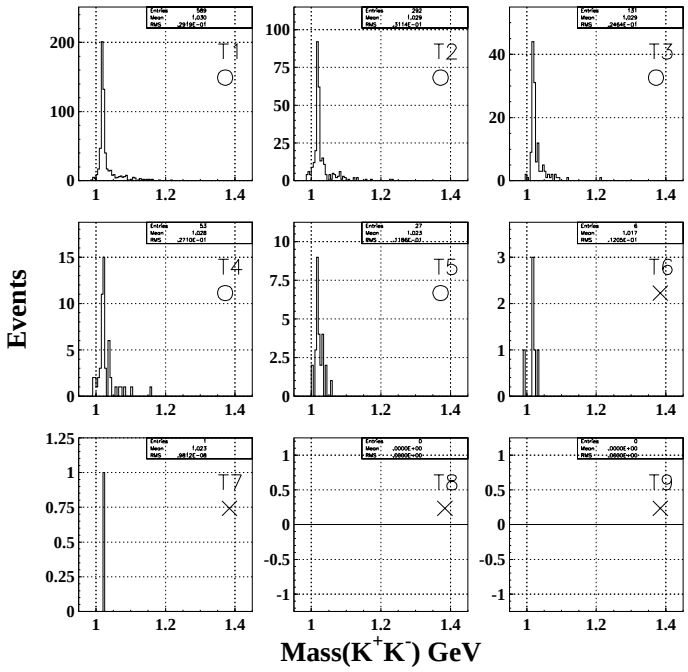

Figure C.3: The K^+K^- mass distribution for E2 bin in real data.

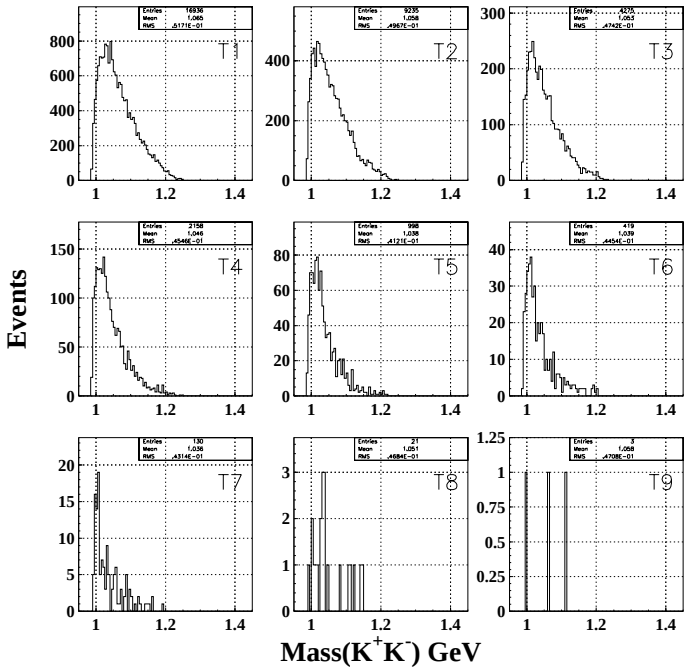

Figure C.4: The K^+K^- mass distribution for non-resonant KKp background for E2 bin in Monte Carlo simulation.

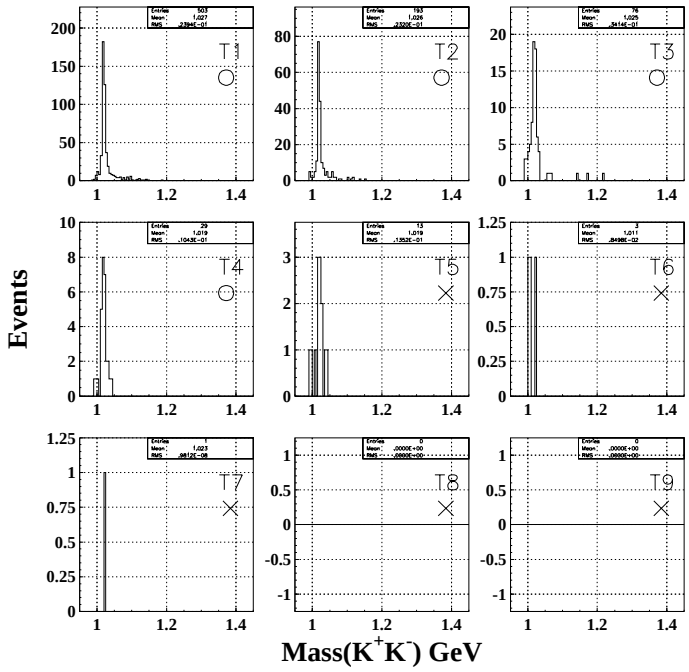

Figure C.5: The K^+K^- mass distribution for E3 bin in real data.

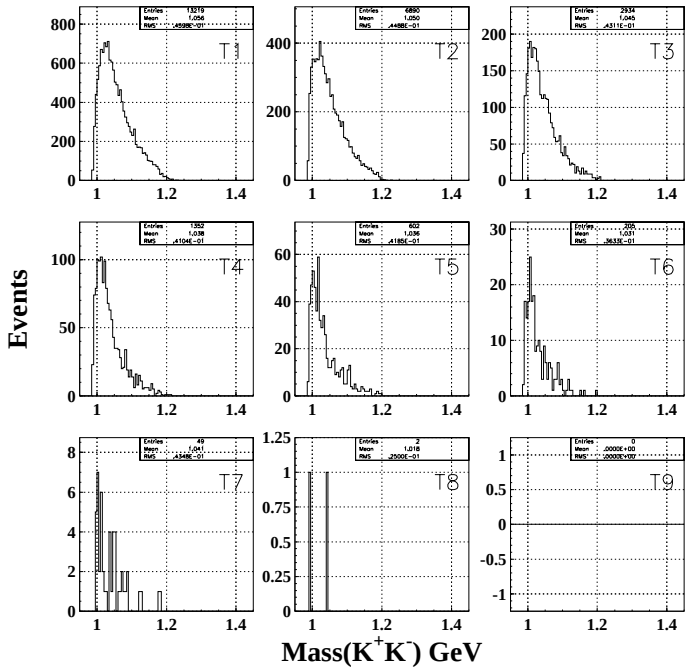

Figure C.6: The K^+K^- mass distribution for non-resonant KKp background for E3 bin in Monte Carlo simulation.

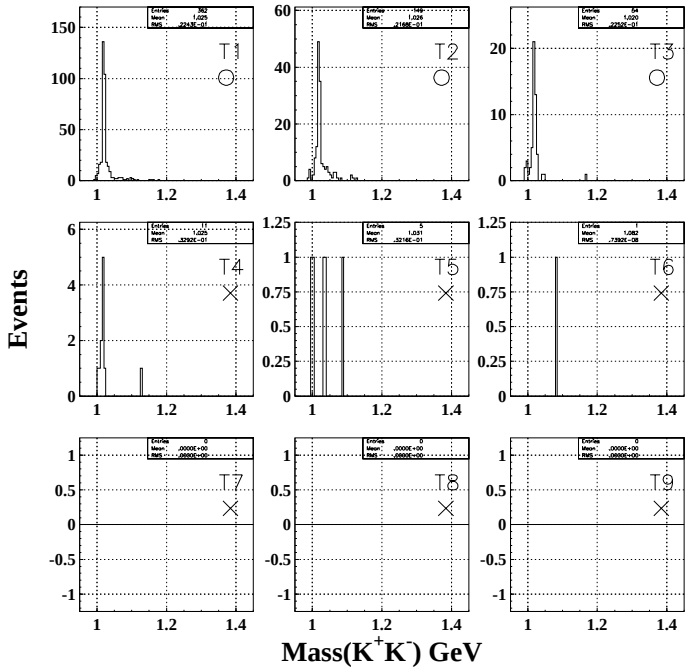

Figure C.7: The K^+K^- mass distribution for E4 bin in real data.

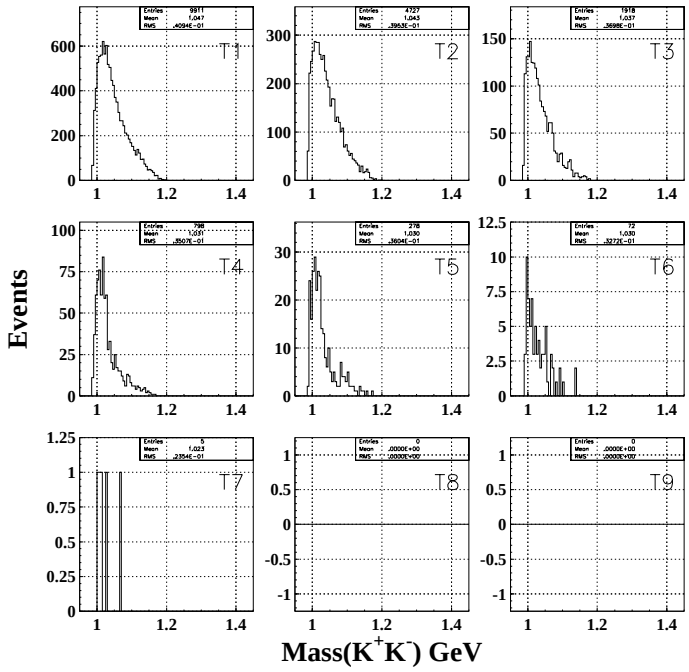

Figure C.8: The K^+K^- mass distribution for non-resonant KKp background for E4 bin in Monte Carlo simulation.

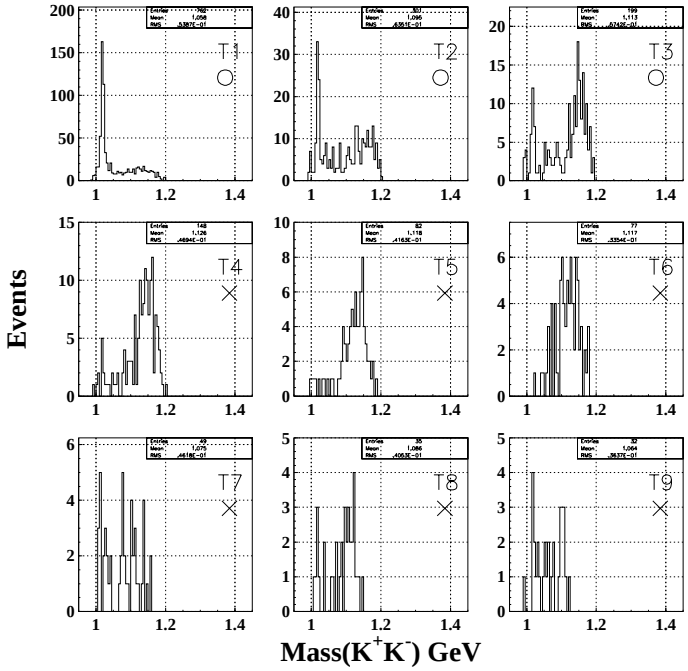

Figure C.9: The K^+K^- mass distribution for E5 bin in real data.

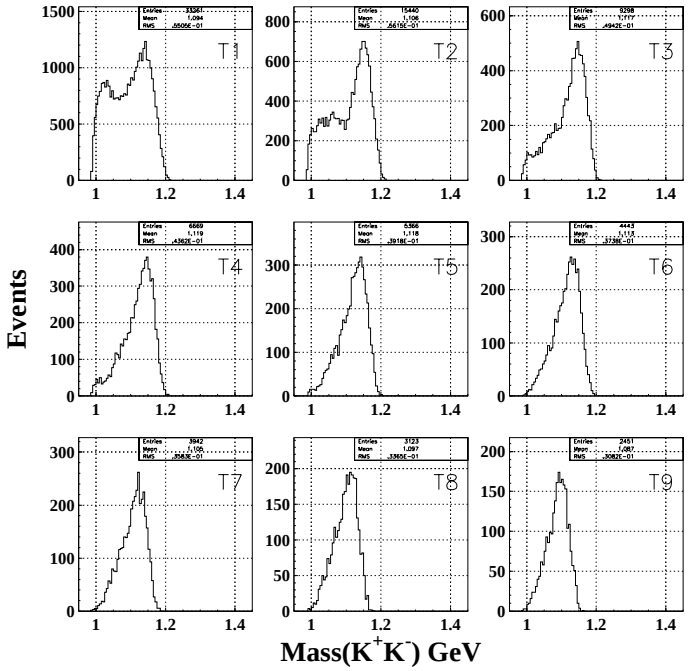

Figure C.10: The K^+K^- mass distribution for non-resonant KKp background for E5 bin in Monte Carlo simulation.

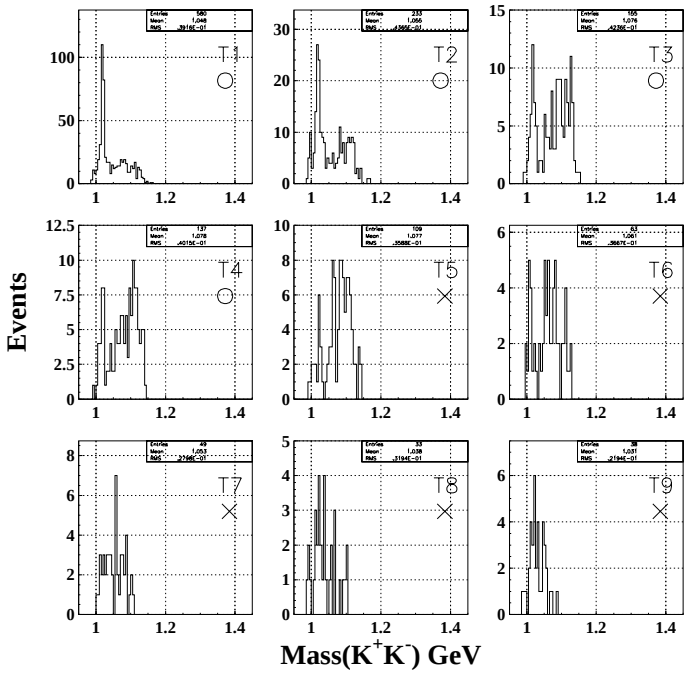

Figure C.11: The K^+K^- mass distribution for E6 bin in real data.

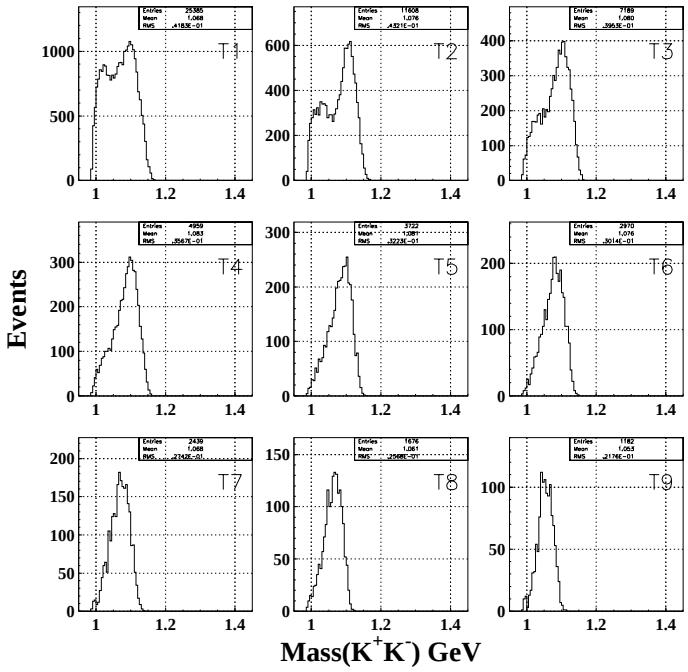

Figure C.12: The K^+K^- mass distribution for non-resonant KKp background for E6 bin in Monte Carlo simulation.

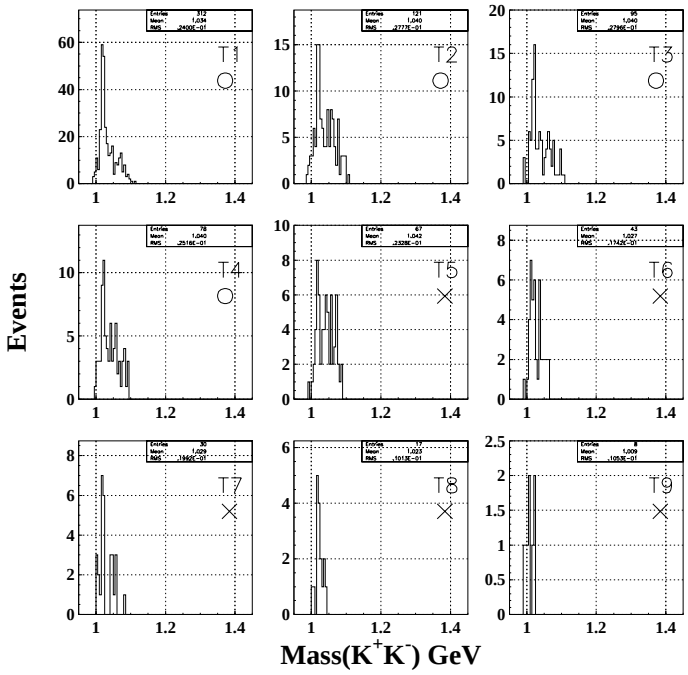

Figure C.13: The K^+K^- mass distribution for E7 bin in real data.

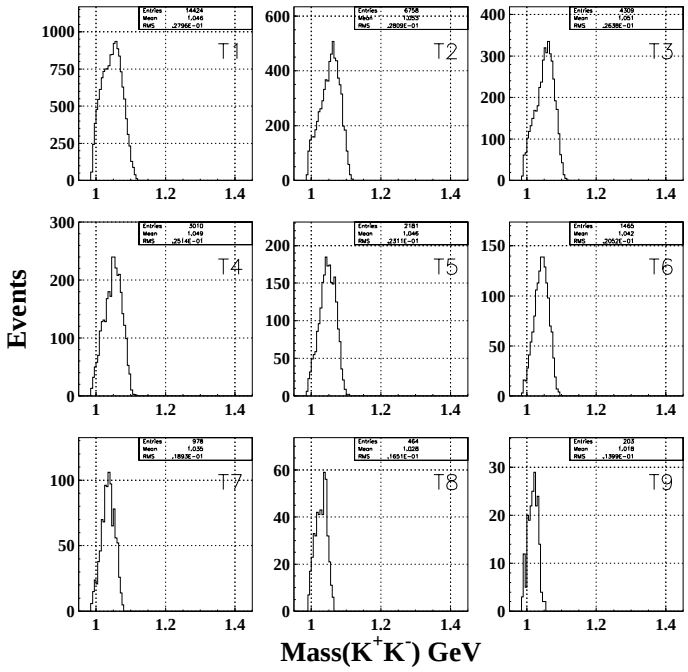

Figure C.14: The K^+K^- mass distribution for non-resonant KKp background for E7 bin in Monte Carlo simulation.

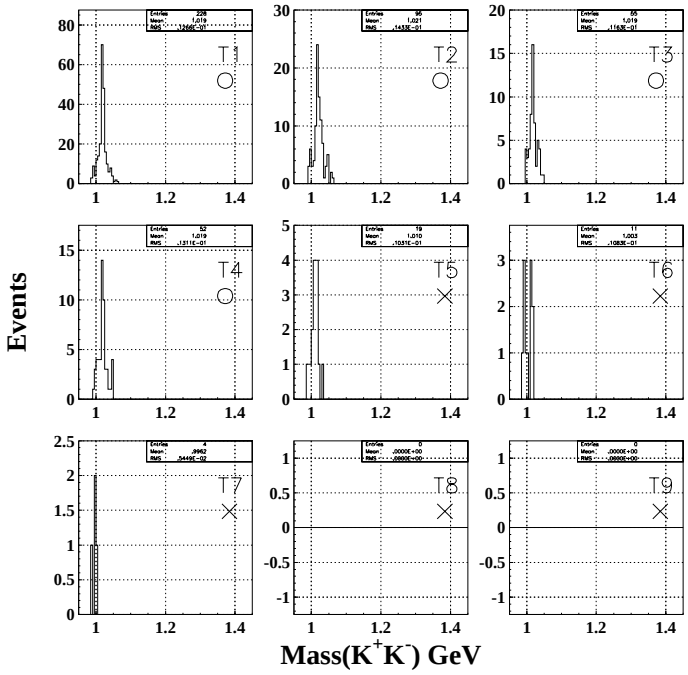

Figure C.15: The K^+K^- mass distribution for E8 bin in real data.

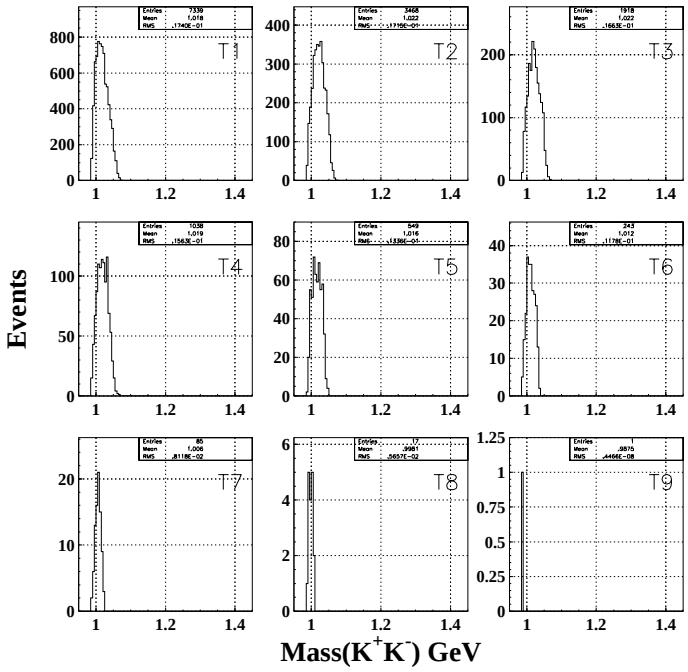

Figure C.16: The K^+K^- mass distribution for non-resonant KKp background for E8 bin in Monte Carlo simulation.

C.2 Number of ϕ events and backgrounds

Table C.1: Number of the ϕ events and the backgrounds

E_γ bin	T bin	N_{signal}	$N_{side,\Lambda excl.}$	$N_{side,\Lambda selec.}$	$N_{signal,BG}$	N_ϕ	S/N
1	5	16	7	2	2.2 ± 1.1	13.8 ± 3.3	6.1
1	4	35	17	9	5.1 ± 1.5	29.9 ± 4.9	5.9
1	3	89	23	9	4.8 ± 1.5	84.2 ± 8.8	17.5
1	2	203	56	17	9.8 ± 1.9	193.2 ± 13.4	19.6
1	1	440	113	21	17.0 ± 2.5	423.0 ± 20.0	24.9
2	5	17	2	3	.6 ± .8	16.4 ± 3.9	28.8
2	4	33	13	1	4.3 ± 1.5	28.7 ± 4.8	6.7
2	3	88	18	8	4.2 ± 1.5	83.9 ± 8.8	20.2
2	2	188	57	16	13.3 ± 2.2	174.7 ± 12.6	13.1
2	1	417	114	22	21.8 ± 2.9	395.2 ± 19.2	18.1
3	4	22	4	0	1.1 ± .9	20.9 ± 4.4	19.4
3	3	50	18	2	6.0 ± 1.8	44.0 ± 6.0	7.4
3	2	139	30	11	11.0 ± 2.5	128.0 ± 10.6	11.6
3	1	371	70	23	18.1 ± 3.0	352.9 ± 18.1	19.5
4	3	43	7	2	2.5 ± 1.9	40.5 ± 5.9	16.1
4	2	107	23	9	10.3 ± 2.8	96.7 ± 9.0	9.4
4	1	278	42	16	13.8 ± 3.2	264.2 ± 15.6	19.2
5	3	26	64	106	6.9 ± .7	19.1 ± 3.7	2.7
5	2	71	97	122	16.7 ± 1.3	54.3 ± 6.4	3.2
5	1	359	250	113	42.9 ± 2.7	316.1 ± 16.5	7.4
6	4	23	31	79	7.2 ± .9	15.8 ± 3.2	2.2
6	3	31	46	75	11.9 ± 1.2	19.1 ± 3.3	1.6
6	2	74	68	73	18.8 ± 1.8	55.2 ± 6.3	2.9
6	1	247	200	95	51.2 ± 3.5	195.8 ± 12.2	3.8
7	4	26	27	16	9.2 ± 1.6	16.8 ± 3.1	1.8
7	3	38	30	16	9.9 ± 1.7	28.1 ± 4.4	2.9
7	2	42	48	20	13.6 ± 2.0	28.4 ± 4.2	2.1
7	1	159	96	25	32.3 ± 3.6	126.7 ± 9.7	3.9
8	4	31	16	0	15.2 ± 4.3	15.8 ± 2.2	1.0
8	3	34	12	0	9.2 ± 3.3	24.8 ± 3.7	2.7
8	2	61	25	0	20.7 ± 4.9	40.3 ± 4.4	1.9
8	1	148	53	3	38.4 ± 6.4	109.6 ± 8.0	2.9

Table C.2: Number of the ϕ events, the backgrounds as a function of angles for ET1 in the VT data

angle	average angle	N_{signal}	$N_{side,\Lambda excl.}$	$N_{side,\Lambda selec.}$	$N_{signal,BG}$	N_{ϕ}	S/N
$\cos\theta$	-0.92	13	6	0	1.9 ± 0.7	11.1 ± 3.7	5.7
	-0.75	40	12	0	2.9 ± 0.8	37.1 ± 6.4	12.9
	-0.58	52	7	0	2.3 ± 0.8	49.7 ± 7.3	21.1
	-0.42	55	16	0	4.5 ± 1.1	50.5 ± 7.6	11.3
	-0.25	60	16	0	3.9 ± 0.9	56.1 ± 7.9	14.3
	-0.08	68	14	4	2.6 ± 0.8	65.4 ± 8.3	25.4
	0.08	78	13	2	3.7 ± 0.9	74.3 ± 8.9	20.1
	0.25	80	9	6	2.3 ± 0.9	77.7 ± 9.1	33.4
	0.42	67	6	4	1.3 ± 0.7	65.7 ± 8.3	52.3
	0.58	40	6	8	3.2 ± 1.0	36.8 ± 6.5	11.6
	0.75	42	3	9	2.0 ± 0.7	40.0 ± 6.6	19.8
	0.92	18	4	5	2.5 ± 0.8	15.5 ± 4.4	6.1
ϕ	15	34	19	4	4.5 ± 0.9	29.5 ± 6.0	6.5
	45	45	13	10	4.5 ± 1.1	40.5 ± 6.9	8.9
	75	54	10	5	3.6 ± 1.1	50.4 ± 7.5	14.0
	105	64	6	0	2.7 ± 1.0	61.3 ± 8.2	22.5
	135	55	6	0	2.0 ± 0.7	53.0 ± 7.5	26.4
	165	44	3	0	0.5 ± 0.3	43.5 ± 6.7	81.2
	195	37	8	0	1.4 ± 0.5	35.6 ± 6.1	25.6
	215	58	7	1	1.5 ± 0.7	56.5 ± 7.7	37.3
	245	57	11	1	4.4 ± 1.2	52.6 ± 7.7	11.8
	275	68	10	3	4.2 ± 1.2	63.8 ± 8.5	15.4
	305	51	6	8	3.1 ± 1.0	47.9 ± 7.3	15.6
	335	46	13	6	2.9 ± 0.7	43.1 ± 6.9	14.9
$\phi - \Phi$	15	60	6	2	4.0 ± 1.4	56.0 ± 8.0	13.9
	45	55	6	3	2.8 ± 0.8	52.2 ± 7.5	18.6
	75	40	11	10	1.7 ± 0.4	38.3 ± 6.4	22.1
	105	44	7	0	1.4 ± 0.4	42.6 ± 6.7	29.8
	135	49	13	1	3.1 ± 0.9	45.9 ± 7.1	14.8
	165	59	5	0	3.3 ± 1.4	55.7 ± 7.9	16.8
	195	73	5	2	3.1 ± 1.4	69.9 ± 8.8	22.3
	215	48	9	2	3.8 ± 1.2	44.2 ± 7.1	11.8
	245	45	27	3	7.7 ± 1.4	37.3 ± 6.9	4.8
	275	33	13	9	4.0 ± 1.0	29.0 ± 5.9	7.3
	305	49	8	3	2.4 ± 0.9	46.6 ± 7.2	19.7
	335	58	2	3	0.7 ± 1.0	57.3 ± 7.9	83.5
$\phi + \Phi$	15	66	4	4	2.4 ± 0.8	63.6 ± 8.3	26.5
	45	51	6	3	1.8 ± 0.7	49.2 ± 7.2	27.6
	75	42	11	2	2.3 ± 0.7	39.7 ± 6.6	17.1
	105	39	12	2	3.3 ± 0.8	35.7 ± 6.4	10.7
	135	55	9	0	2.8 ± 0.9	52.2 ± 7.5	18.5
	165	63	8	2	3.0 ± 1.0	60.0 ± 8.1	19.9
	195	62	13	4	3.7 ± 1.1	58.3 ± 8.0	15.8
	215	40	6	3	2.9 ± 0.9	37.1 ± 6.5	12.9
	245	47	11	6	3.1 ± 0.8	43.9 ± 7.0	14.3
	275	42	10	5	1.9 ± 0.7	40.1 ± 6.6	21.0
	305	56	16	5	4.6 ± 1.1	51.4 ± 7.6	11.3
	335	50	6	2	1.7 ± 0.7	48.3 ± 7.2	28.5
Φ	15	37	9	6	2.2 ± 0.7	34.8 ± 6.2	16.0
	45	59	5	4	2.7 ± 0.8	56.3 ± 7.8	21.1
	75	68	20	1	4.5 ± 1.1	63.5 ± 8.4	14.2
	105	63	14	1	3.5 ± 1.0	59.5 ± 8.1	16.8
	135	52	12	3	3.0 ± 0.9	49.0 ± 7.3	16.1
	165	36	4	1	2.2 ± 0.8	33.8 ± 6.1	15.0
	195	43	9	2	1.9 ± 0.7	41.1 ± 6.6	22.1
	215	37	5	4	2.3 ± 0.7	34.7 ± 6.2	14.9
	245	60	12	3	3.7 ± 1.0	56.3 ± 7.9	15.1
	275	69	10	5	3.0 ± 0.9	66.0 ± 8.4	22.1
	305	60	6	3	1.8 ± 0.7	58.2 ± 7.9	31.7
	335	29	6	5	3.1 ± 0.8	25.9 ± 5.5	8.4

Table C.3: Number of the ϕ events, the backgrounds as a function of angles for ET1 in the HZ data

angle	average angle	N_{signal}	$N_{side,\Lambda excl.}$	$N_{side,\Lambda selec.}$	$N_{signal,BG}$	N_{ϕ}	S/N
$\cos\theta$	-0.92	25	11	0	2.6 ± 0.8	22.4 ± 5.1	8.5
	-0.75	43	8	0	1.3 ± 0.6	41.7 ± 6.6	31.7
	-0.58	44	7	0	2.7 ± 0.8	41.3 ± 6.8	15.5
	-0.42	61	10	0	2.4 ± 0.8	58.6 ± 7.9	24.1
	-0.25	74	17	0	3.8 ± 0.9	70.2 ± 8.7	18.5
	-0.08	62	11	0	1.9 ± 0.7	60.1 ± 8.0	31.3
	0.08	72	14	7	2.4 ± 0.7	69.6 ± 8.6	29.4
	0.25	73	10	7	2.4 ± 0.8	70.6 ± 8.7	29.1
	0.42	68	7	6	2.8 ± 0.9	65.2 ± 8.4	23.4
	0.58	56	7	2	2.2 ± 0.9	53.8 ± 7.6	25.0
	0.75	33	11	6	3.7 ± 1.0	29.3 ± 5.9	7.9
	0.92	24	5	11	2.7 ± 0.8	21.3 ± 5.0	7.7
ϕ	15	34	10	7	2.3 ± 0.7	31.7 ± 5.9	14.0
	45	60	13	9	4.6 ± 1.1	55.4 ± 7.9	12.1
	75	67	10	1	2.8 ± 1.0	64.2 ± 8.4	22.9
	105	55	7	0	3.4 ± 1.1	51.6 ± 7.6	15.1
	135	59	8	0	1.4 ± 0.6	57.6 ± 7.8	41.7
	165	38	9	0	1.4 ± 0.5	36.6 ± 6.2	25.7
	195	46	8	1	1.2 ± 0.5	44.8 ± 6.8	36.7
	215	54	9	0	1.8 ± 0.7	52.2 ± 7.5	29.5
	245	50	7	0	2.5 ± 0.9	47.5 ± 7.2	19.4
	275	64	14	5	4.5 ± 1.3	59.5 ± 8.2	13.2
	305	63	14	8	4.5 ± 1.2	58.5 ± 8.1	13.0
	335	45	9	8	2.5 ± 0.7	42.5 ± 6.8	16.8
$\phi - \Phi$	15	63	16	6	1.7 ± 0.5	61.3 ± 8.0	35.8
	45	55	9	1	2.4 ± 0.8	52.6 ± 7.5	21.9
	75	34	7	4	3.3 ± 1.2	30.7 ± 6.1	9.2
	105	30	2	2	1.3 ± 0.9	28.7 ± 5.7	21.3
	135	51	6	2	2.4 ± 1.0	48.6 ± 7.3	19.9
	165	78	15	8	3.9 ± 1.0	74.1 ± 9.0	18.8
	195	58	14	4	3.5 ± 0.9	54.5 ± 7.8	15.6
	215	46	8	3	2.7 ± 1.0	43.3 ± 6.9	16.0
	245	38	1	0	4.2 ± 1.6	33.8 ± 6.5	8.1
	275	45	10	2	4.3 ± 1.4	40.7 ± 7.0	9.4
	305	51	13	4	3.8 ± 1.0	47.2 ± 7.3	12.5
	335	86	17	3	1.7 ± 0.4	84.3 ± 9.3	49.9
$\phi + \Phi$	15	52	12	0	1.8 ± 0.7	50.2 ± 7.3	27.4
	45	50	9	4	2.5 ± 0.8	47.5 ± 7.2	19.2
	75	57	6	2	2.6 ± 0.9	54.4 ± 7.7	21.2
	105	49	12	3	3.8 ± 1.1	45.2 ± 7.2	11.8
	135	61	7	7	2.1 ± 0.8	58.9 ± 7.9	28.6
	165	58	16	2	3.2 ± 0.8	54.8 ± 7.7	17.1
	195	53	8	3	2.3 ± 0.7	50.7 ± 7.4	21.9
	215	39	12	4	3.2 ± 0.9	35.8 ± 6.4	11.3
	245	62	8	4	2.1 ± 0.8	59.9 ± 8.0	28.0
	275	57	11	3	3.4 ± 1.0	53.6 ± 7.7	15.8
	305	50	7	5	2.1 ± 0.7	47.9 ± 7.2	23.2
	335	47	10	2	1.8 ± 0.6	45.2 ± 6.9	25.7
Φ	15	76	18	3	3.4 ± 1.0	72.6 ± 8.9	21.2
	45	49	13	2	3.9 ± 0.9	45.1 ± 7.1	11.7
	75	41	6	0	1.1 ± 0.6	39.9 ± 6.5	37.1
	105	40	7	2	1.7 ± 0.6	38.3 ± 6.4	22.7
	135	40	6	4	2.3 ± 0.7	37.7 ± 6.4	16.5
	165	59	8	4	2.3 ± 0.8	56.7 ± 7.8	25.1
	195	58	8	12	2.5 ± 0.8	55.5 ± 7.7	22.4
	215	45	10	3	2.4 ± 0.8	42.6 ± 6.8	17.5
	245	59	8	1	1.3 ± 0.6	57.7 ± 7.8	44.2
	275	31	12	0	2.8 ± 0.8	28.2 ± 5.7	9.9
	305	64	6	4	2.8 ± 0.8	61.2 ± 8.1	21.7
	335	73	16	4	4.2 ± 1.1	68.8 ± 8.7	16.2

Table C.4: Number of the ϕ events, the backgrounds as a function of angles for ET2 in the VT data

angle	average angle	N_{signal}	$N_{side,\Lambda excl.}$	$N_{side,\Lambda selec.}$	$N_{signal,BG}$	N_{ϕ}	S/N
$\cos\theta$	-0.92	13	4	0	1.3 ± 0.6	11.7 ± 3.7	8.6
	-0.75	26	2	0	0.5 ± 0.5	25.5 ± 5.2	51.1
	-0.58	34	5	0	2.4 ± 1.0	31.6 ± 6.0	13.4
	-0.42	40	5	0	1.9 ± 0.9	38.1 ± 6.5	19.7
	-0.25	47	5	4	2.4 ± 0.9	44.6 ± 7.0	19.0
	-0.08	42	4	5	2.4 ± 0.8	39.6 ± 6.6	16.4
	0.08	59	4	2	0.8 ± 0.6	58.2 ± 7.8	70.3
	0.25	45	5	1	2.4 ± 0.9	42.6 ± 6.9	17.9
	0.42	50	5	2	1.7 ± 0.9	48.3 ± 7.2	28.4
	0.58	42	1	2	1.6 ± 1.1	40.4 ± 6.7	24.5
	0.75	26	5	5	7.1 ± 2.4	18.9 ± 5.7	2.7
	0.92	12	6	0	1.7 ± 1.2	10.3 ± 3.7	6.1
ϕ	15	31	6	1	2.3 ± 0.9	28.7 ± 5.7	12.4
	45	39	2	4	3.3 ± 1.3	35.7 ± 6.5	10.7
	75	59	3	3	3.3 ± 1.3	55.7 ± 7.9	17.1
	105	44	4	1	1.6 ± 0.9	42.4 ± 6.8	25.8
	135	26	3	0	1.8 ± 0.8	24.2 ± 5.2	13.5
	165	22	3	0	1.1 ± 0.5	20.9 ± 4.8	19.9
	195	19	3	0	0.6 ± 0.4	18.4 ± 4.4	31.1
	215	36	6	0	2.1 ± 0.9	33.9 ± 6.1	16.0
	245	40	3	1	1.7 ± 0.9	38.3 ± 6.5	23.0
	275	46	6	5	4.1 ± 1.3	41.9 ± 7.0	10.1
	305	45	1	4	1.7 ± 1.0	43.3 ± 6.9	25.2
	335	29	11	2	2.9 ± 1.1	26.1 ± 5.6	8.9
$\phi - \Phi$	15	32	1	0	0.7 ± 0.8	31.3 ± 5.8	45.2
	45	37	2	1	0.5 ± 0.6	36.5 ± 6.2	78.7
	75	27	3	3	0.9 ± 0.4	26.1 ± 5.2	29.9
	105	28	5	1	1.0 ± 0.4	27.0 ± 5.3	27.2
	135	37	2	0	0.3 ± 0.5	36.7 ± 6.2	108.6
	165	43	2	0	2.6 ± 1.8	40.4 ± 6.9	15.5
	195	43	2	1	2.6 ± 1.8	40.4 ± 7.0	15.5
	215	46	5	0	2.2 ± 1.0	43.8 ± 7.0	19.6
	245	28	12	5	7.2 ± 1.8	20.8 ± 5.7	2.9
	275	26	8	6	7.4 ± 1.7	18.6 ± 5.4	2.5
	305	41	5	3	7.4 ± 2.4	33.6 ± 7.0	4.6
	335	48	4	1	4.1 ± 2.0	43.9 ± 7.4	10.8
$\phi + \Phi$	15	43	7	2	3.0 ± 1.1	40.0 ± 6.7	13.5
	45	43	5	0	1.2 ± 0.7	41.8 ± 6.7	35.4
	75	33	7	1	3.3 ± 1.0	29.7 ± 5.9	8.9
	105	22	5	0	1.7 ± 0.7	20.3 ± 4.8	11.7
	135	32	4	2	2.0 ± 0.9	30.0 ± 5.8	14.7
	165	40	2	3	3.9 ± 1.3	36.1 ± 6.5	9.2
	195	46	4	2	1.4 ± 0.9	44.6 ± 6.9	32.4
	215	36	2	0	0.6 ± 0.5	35.4 ± 6.1	59.4
	245	34	2	3	1.7 ± 0.9	32.3 ± 6.0	19.1
	275	23	4	3	2.4 ± 0.9	20.6 ± 4.9	8.6
	305	40	6	1	1.7 ± 0.8	38.3 ± 6.4	22.2
	335	44	3	4	3.5 ± 1.2	40.5 ± 6.8	11.6
Φ	15	15	1	2	1.2 ± 0.6	13.8 ± 4.0	11.9
	45	20	4	4	4.6 ± 1.3	15.4 ± 4.7	3.4
	75	52	7	1	2.8 ± 1.1	49.2 ± 7.4	17.8
	105	70	6	0	2.0 ± 1.0	68.0 ± 8.5	34.0
	135	33	3	4	2.3 ± 0.9	30.7 ± 5.9	13.5
	165	18	4	0	1.7 ± 0.8	16.3 ± 4.4	9.6
	195	17	4	1	1.1 ± 0.6	15.9 ± 4.2	14.8
	215	28	5	1	2.2 ± 0.8	25.8 ± 5.4	11.8
	245	56	5	1	1.7 ± 0.9	54.3 ± 7.6	32.8
	275	51	4	3	2.9 ± 1.2	48.1 ± 7.3	16.5
	305	43	4	2	1.7 ± 0.9	41.3 ± 6.7	24.3
	335	33	4	2	2.5 ± 0.9	30.5 ± 5.9	12.3

Table C.5: Number of the ϕ events, the backgrounds as a function of angles for ET2 in the HZ data

angle	average angle	N_{signal}	$N_{side,\Lambda excl.}$	$N_{side,\Lambda selec.}$	$N_{signal,BG}$	N_{ϕ}	S/N
$\cos\theta$	-0.92	12	3	0	0.9 ± 0.5	11.1 ± 3.5	13.0
	-0.75	25	2	0	0.8 ± 0.6	24.2 ± 5.1	30.0
	-0.58	46	4	0	2.8 ± 1.1	43.2 ± 7.0	15.4
	-0.42	35	6	2	1.8 ± 0.9	33.2 ± 6.1	17.9
	-0.25	50	4	4	1.4 ± 0.8	48.6 ± 7.2	35.4
	-0.08	48	5	5	2.3 ± 0.8	45.7 ± 7.1	19.5
	0.08	52	6	5	2.6 ± 0.9	49.4 ± 7.3	19.0
	0.25	51	3	1	0.9 ± 0.7	50.1 ± 7.3	53.3
	0.42	53	3	2	2.2 ± 1.0	50.8 ± 7.5	23.1
	0.58	33	6	2	2.9 ± 1.3	30.1 ± 6.0	10.2
	0.75	43	7	5	6.4 ± 2.2	36.6 ± 7.0	5.7
	0.92	11	2	6	9.2 ± 3.3	1.8 ± 4.7	0.2
ϕ	15	31	11	3	3.6 ± 1.3	27.4 ± 5.8	7.6
	45	49	3	4	3.2 ± 1.3	45.8 ± 7.2	14.5
	75	38	5	2	3.7 ± 1.3	34.3 ± 6.4	9.3
	105	46	1	4	2.3 ± 1.0	43.7 ± 7.0	18.9
	135	34	2	0	0.4 ± 0.5	33.6 ± 5.9	79.6
	165	23	3	0	0.6 ± 0.4	22.4 ± 4.9	35.8
	195	22	3	1	1.4 ± 0.6	20.6 ± 4.8	14.3
	215	35	8	2	3.4 ± 1.1	31.6 ± 6.1	9.2
	245	55	4	4	3.8 ± 1.2	51.2 ± 7.6	13.6
	275	46	1	3	1.2 ± 0.9	44.8 ± 7.0	36.4
	305	50	6	4	2.9 ± 1.2	47.1 ± 7.3	16.5
	335	30	4	5	3.2 ± 1.3	26.8 ± 5.7	8.5
$\phi - \Phi$	15	47	12	9	3.4 ± 0.7	43.6 ± 6.9	13.0
	45	46	7	5	4.9 ± 1.5	41.1 ± 7.0	8.4
	75	29	0	3	5.5 ± 2.7	23.5 ± 6.1	4.2
	105	24	2	0	2.6 ± 1.2	21.4 ± 5.2	8.4
	135	34	2	0	0.2 ± 0.5	33.8 ± 6.0	146.3
	165	53	3	1	1.9 ± 1.1	51.1 ± 7.5	26.3
	195	45	8	3	3.7 ± 1.3	41.3 ± 6.9	11.1
	215	35	1	0	1.5 ± 0.9	33.5 ± 6.1	22.6
	245	30	2	1	2.5 ± 1.7	27.5 ± 5.9	10.9
	275	29	0	0	0.3 ± 0.6	28.7 ± 5.5	98.8
	305	34	6	3	3.6 ± 1.3	30.4 ± 6.0	8.5
	335	53	8	7	2.1 ± 0.6	50.9 ± 7.3	23.7
$\phi + \Phi$	15	35	5	0	1.4 ± 0.6	33.6 ± 6.0	23.2
	45	37	5	7	4.7 ± 1.5	32.3 ± 6.3	6.9
	75	44	5	4	3.5 ± 1.2	40.5 ± 6.8	11.6
	105	31	3	4	3.3 ± 1.2	27.7 ± 5.8	8.5
	135	28	3	2	1.2 ± 0.7	26.8 ± 5.4	22.6
	165	36	4	1	1.7 ± 0.8	34.3 ± 6.1	19.7
	195	33	3	1	1.1 ± 0.7	31.9 ± 5.9	28.9
	215	37	8	0	2.6 ± 0.8	34.4 ± 6.2	13.0
	245	45	2	3	3.3 ± 1.2	41.7 ± 6.9	12.6
	275	50	5	4	3.9 ± 1.3	46.1 ± 7.3	12.0
	305	48	4	5	4.4 ± 1.5	43.6 ± 7.2	9.8
	335	35	4	1	1.1 ± 0.7	33.9 ± 6.0	30.0
Φ	15	49	8	4	5.6 ± 1.4	43.4 ± 7.2	7.8
	45	45	7	2	2.6 ± 1.0	42.4 ± 6.9	16.1
	75	29	1	2	1.7 ± 0.8	27.3 ± 5.5	15.6
	105	25	0	0	0.3 ± 0.4	24.7 ± 5.1	87.5
	135	36	1	3	2.0 ± 0.9	34.0 ± 6.1	17.0
	165	60	5	5	4.3 ± 1.4	55.7 ± 8.0	13.0
	195	44	8	3	4.2 ± 1.3	39.8 ± 6.9	9.5
	215	38	4	2	1.3 ± 0.8	36.7 ± 6.3	28.1
	245	29	2	1	0.5 ± 0.5	28.5 ± 5.5	57.8
	275	19	2	2	1.9 ± 0.8	17.1 ± 4.5	8.8
	305	38	5	3	2.6 ± 1.1	35.4 ± 6.3	13.7
	335	47	8	5	5.0 ± 1.5	42.0 ± 7.1	8.4

Appendix D

Various checks on the forward angle cross section

D.1 Energy dependence of $d\sigma/dt$ at the most forward $\tilde{t}$ bin

The measurement of the energy dependence of the differential cross section at $\tilde{t} = 0$ GeV^2 was described in Section 4.1. The data showed a non-monotonical behavior as shown in Fig. 4.6, i.e. cross section increases with energy upto $E_\gamma \sim 2.0$ GeV and then start decrease with energy. The measured cross section was obtained from the fit to the $\tilde{t}$ distribution by the exponential function. Since the acceptance of the LEPS spectrometer is maximum at the most forward angle, there are enough number of signals at the most forward angle to measure the energy dependence of cross section with high accuracy. Fig. D.1 shows energy dependence of the differential cross section at $\tilde{t} = 0$ and at $-0.1 < \tilde{t} < 0.0$ GeV^2. Non-monotonical energy dependence is present in data points at $-0.1 < \tilde{t} < 0.0$ GeV^2 which were obtained without fit. This indicates that possibilities of an incorrect fitting procedure or mismeasurements of cross section at large angular bins, which could introduce the non-monotonical behavior, are ruled out as a source of non-monotonical energy dependence.

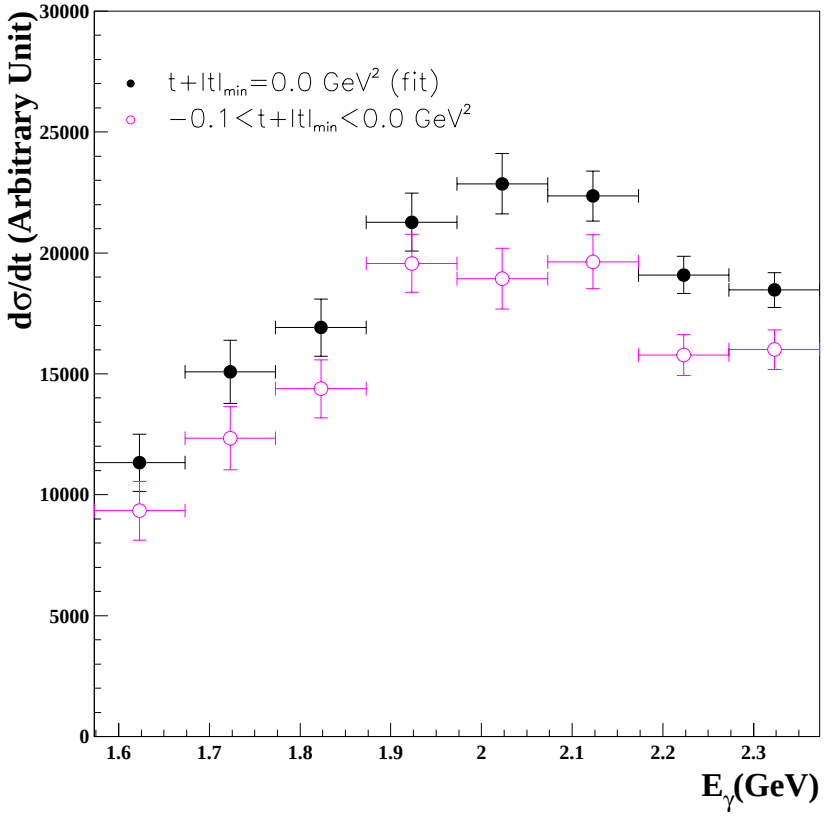

Figure D.1: Energy dependence of the differential cross section. Closed circle indicates the differential cross section at $\tilde{t} = 0$ which was obtained by the fit by Eq. 4.1. Open circle indicates the differential cross section at forward $\tilde{t}$ bin (-0.1< $\tilde{t}$ <0.0 GeV^2).

D.2 Comparison of the cross section between KK and Kp modes

There are kinematical regions where both KK and Kp modes have a non-zero acceptance. For example, , the acceptance for KK mode is decrease with energy as shown in Fig. B.6 , but even at lower energy, the acceptance at forward angles is still large enough to identify the reaction, where the acceptance of Kp mode is high. In such regions, the differential cross section can be measured from two independent sample (KK mode and Kp mode). Measurements by KK mode and Kp mode were used to check a consistency of data. The same analysis was applied to the sub-sample where ϕ signals were unambiguously identified in KK and Kp modes separately. Fig. D.2 shows $\tilde{t}$ distributions measured by KK and Kp modes. There is a good consistency between KK and Kp mode within statistical error bar. This implies the correctness of acceptance calculation and background subtraction.

The energy dependence of the cross section at the most forward angular bin was checked by KK mode and Kp mode separately as shown in Fig. D.3. The non-monotonical energy dependence was observed in measurement by both KK and Kp modes. Note that only KK mode was used in the analysis described in Section 4.1 and Appendix D.1.

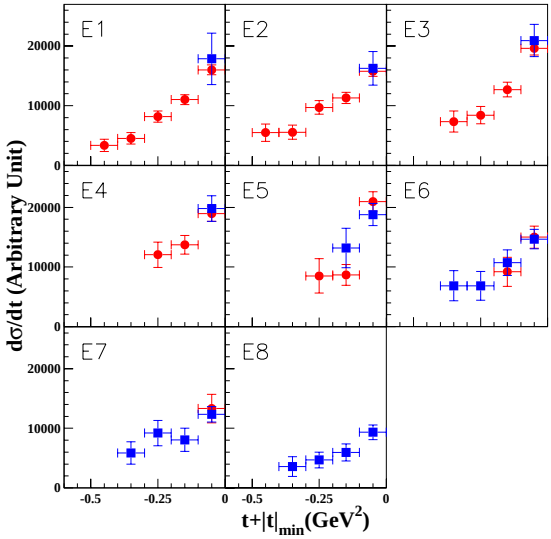

Figure D.2: Differential cross section as a function of energy. Closed circle indicates the measurement by KK reconstructed event (KKp mode + K^+K^- mode). Closed square indicates the measurement by Kp reconstructed event (K^+p mode + K^-p mode).

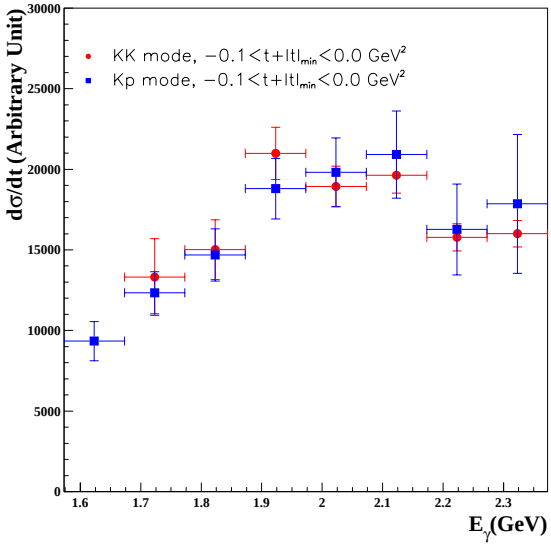

Figure D.3: Energy dependence of the differential cross section. Closed circle indicates the measurement by KK reconstructed event (KKp mode + K^+K^- mode). Closed square indicates the measurement by Kp reconstructed event (K^+p mode + K^-p mode).

D.3 Differential cross section with smaller bin-size

The energy dependence of the differential cross section is presented in Section 4.1 with 100 MeV interval of the photon energy. We examined the same analysis with 50 MeV interval for highest energy sample with 2.173< E_γ <2.373 GeV since there are enough number of counts around the highest energy where the acceptance is maximum. The E1 and E2 bin were divided into two sub-samples, i.e;

$$E1\text{-}1, 2.323 < E_\gamma < 2.373\text{GeV}$$
$$E1\text{-}2, 2.273 < E_\gamma < 2.323\text{GeV}$$
$$E2\text{-}1, 2.223 < E_\gamma < 2.273\text{GeV}$$
$$E2\text{-}2, 2.173 < E_\gamma < 2.223\text{GeV}.$$

The KK reconstruct mode was used in this analysis since there is almost no Kp reconstructed events in these kinematical region. Fig. D.4 shows $\tilde{t}$ distribution for the sub-samples. All sub-samples shows similar trend. Fits to the distribution was performed with similar manner as discussed in Section 4.1. Two choices of parameterization for the fit were examined, i.e. (1) slope b as a free parameter and (2) fixed slope parameter. The average slope $b = 3.198$ GeV^{-2} was used for latter case. All fits succeed to describe the measured $\tilde{t}$ distribution. The slope parameter for sub-samples from fit (1) was shown in Fig. D.5. No significant fine structure was seen. The energy dependence of the differential cross section at $\tilde{t} = 0$ GeV^2 is shown in Fig. D.6. The fluctuation of the data points for sub-samples compared with original data points (100 MeV interval) is consistent with statistical error. No hidden fine structure was appeared when the energy interval was changed from 100 MeV to 50 MeV. The data points for sub-samples show global decrease of the cross section with energy in 2.173< E_γ <2.373 GeV.

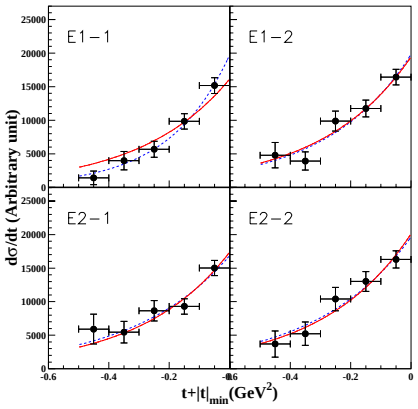

Figure D.4: $\tilde{t}$ distribution for E1-1, E1-2, E2-1 and E2-2 bin. Dotted line indicates a fit to the distribution with free slope parameter. Solid line indicates a fit with fixed slope parameter $b = 3.198$ GeV^{-2}.

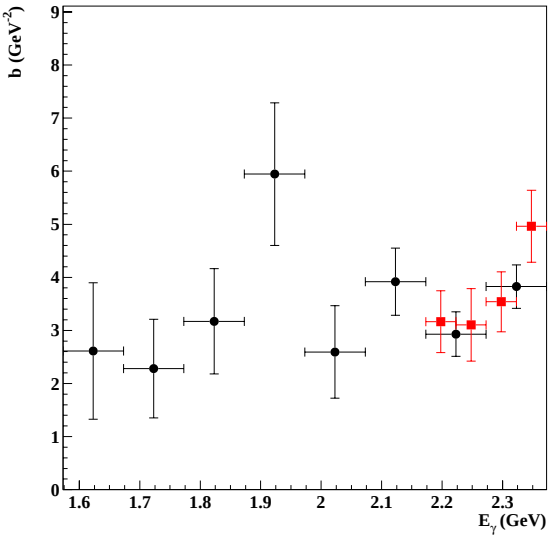

Figure D.5: Energy dependence of the slope parameter for $\tilde{t}$ distribution. Closed circle indicates the differential cross section at $\tilde{t} = 0$ with 100 MeV interval (Section 4.1). Closed square indicates the same analysis with 50 MeV interval. Solid line represents the average slope for all data points.

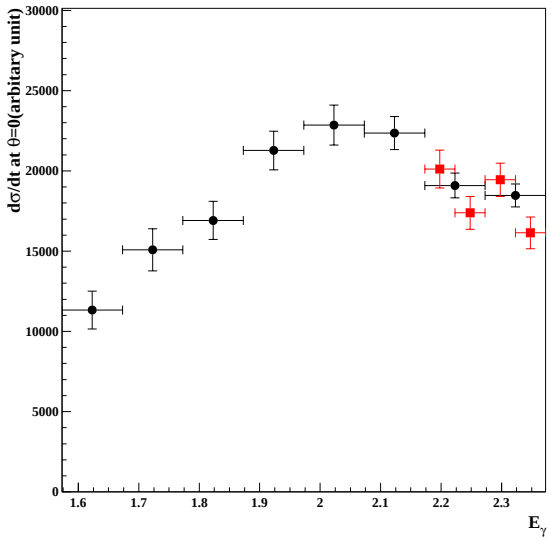

Figure D.6: Energy dependence of the differential cross section. Closed circle indicates the differential cross section at $\tilde{t} = 0$ with 100 MeV (Section 4.1). Closed square indicates the same analysis with 50 MeV interval.

Appendix E

Tables of cross sections and decay angular distributions

Table E.1: Differential cross sections

E_γ(GeV)	$\tilde{t}$(GeV^2)	$d\sigma/dt$ (A.U.)	b (sys. err) (GeV^{-2})	n_0 (sys. err) (A.U.)
2.273∼2.373	-0.1∼ 0.0	1.6007 ± 0.0817×10^4		
	-0.2∼-0.1	1.1014 ± 0.0840×10^4		
	-0.3∼-0.2	0.8172 ± 0.0954×10^4		
	-0.4∼-0.3	0.4529 ± 0.0949×10^4		
	-0.5∼-0.4	0.3343 ± 0.1035×10^4	3.581 ± 0.414 (0.010)	1.85 ± 0.07 (0.05)×10^4
2.173∼2.273	-0.1∼ 0.0	1.5771 ± 0.0843×10^4		
	-0.2∼-0.1	1.1299 ± 0.0923×10^4		
	-0.3∼-0.2	0.9711 ± 0.1135×10^4		
	-0.4∼-0.3	0.5553 ± 0.1181×10^4		
	-0.5∼-0.4	0.5469 ± 0.1461×10^4	2.697 ± 0.427 (0.119)	1.91 ± 0.08 (0.04)×10^4
2.073∼2.173	-0.1∼ 0.0	1.9636 ± 0.1116×10^4		
	-0.2∼-0.1	1.2705 ± 0.1229×10^4		
	-0.3∼-0.2	0.8414 ± 0.1438×10^4		
	-0.4∼-0.3	0.7339 ± 0.1765×10^4	3.830 ± 0.647 (0.220)	2.24 ± 0.10 (0.07)×10^4
1.973∼2.073	-0.1∼ 0.0	1.8937 ± 0.1258×10^4		
	-0.2∼-0.1	1.3717 ± 0.1572×10^4		
	-0.3∼-0.2	1.2054 ± 0.2132×10^4	2.757 ± 0.896 (0.128)	2.29 ± 0.12 (0.03)×10^4
1.873∼1.973	-0.1∼ 0.0	1.9566 ± 0.1199×10^4		
	-0.2∼-0.1	0.9398 ± 0.1488×10^4		
	-0.3∼-0.2	0.9000 ± 0.2444×10^4	6.037 ± 1.352 (0.390)	2.13 ± 0.12 (0.05)×10^4
1.773∼1.873	-0.1∼ 0.0	1.4381 ± 0.1199×10^4		
	-0.2∼-0.1	0.9807 ± 0.1579×10^4		
	-0.3∼-0.2	0.6444 ± 0.1940×10^4		
	-0.4∼-0.3	0.7695 ± 0.2393×10^4	3.233 ± 0.984 (1.199)	1.69 ± 0.12 (0.07)×10^4
1.673∼1.773	-0.1∼ 0.0	1.2334 ± 0.1302×10^4		
	-0.2∼-0.1	0.8062 ± 0.1950×10^4		
	-0.3∼-0.2	0.9201 ± 0.2128×10^4		
	-0.4∼-0.3	0.5856 ± 0.1887×10^4	2.109 ± 0.886 (1.333)	1.51 ± 0.13 (0.25)×10^4
1.573∼1.673	-0.1∼ 0.0	0.9338 ± 0.1221×10^4		
	-0.2∼-0.1	0.5957 ± 0.1430×10^4		
	-0.3∼-0.2	0.4688 ± 0.1326×10^4		
	-0.4∼-0.3	0.3576 ± 0.1644×10^4	2.216 ± 1.230 (0.061)	1.13 ± 0.12 (0.07)×10^4

Table E.2: Decay angular distributions

Angle	Average angle	W ($1.973 < E_\gamma < 2.173$) (sys.err)	W ($1.973 < E_\gamma < 2.173$) (sys.err)
$\cos\theta$	-0.92	0.184 ± 0.041 (0.000)	0.202 ± 0.038 (0.000)
	-0.75	0.353 ± 0.052 (0.000)	0.401 ± 0.047 (0.000)
	-0.58	0.525 ± 0.065 (0.000)	0.454 ± 0.050 (0.000)
	-0.42	0.508 ± 0.064 (0.005)	0.544 ± 0.055 (0.000)
	-0.25	0.678 ± 0.074 (0.006)	0.628 ± 0.059 (0.000)
	-0.08	0.623 ± 0.071 (0.019)	0.615 ± 0.057 (0.000)
	0.08	0.787 ± 0.079 (0.024)	0.719 ± 0.062 (0.004)
	0.25	0.654 ± 0.071 (0.021)	0.741 ± 0.063 (0.001)
	0.42	0.697 ± 0.073 (0.015)	0.658 ± 0.060 (0.010)
	0.58	0.491 ± 0.063 (0.031)	0.465 ± 0.052 (0.012)
	0.75	0.401 ± 0.066 (0.119)	0.356 ± 0.046 (0.012)
	0.92	0.099 ± 0.049 (0.046)	0.218 ± 0.040 (0.004)
		$2\pi W$ ($1.973 < E_\gamma < 2.173$) (sys.err)	$2\pi W$ ($1.973 < E_\gamma < 2.173$) (sys.err)
ϕ	15	0.925 ± 0.135 (0.194)	0.719 ± 0.099 (0.008)
	45	1.100 ± 0.132 (0.115)	0.921 ± 0.101 (0.010)
	75	1.242 ± 0.141 (0.033)	1.062 ± 0.105 (0.004)
	105	1.168 ± 0.133 (0.025)	1.046 ± 0.104 (0.000)
	135	0.807 ± 0.111 (0.013)	1.094 ± 0.107 (0.000)
	165	0.726 ± 0.115 (0.005)	0.981 ± 0.112 (0.000)
	195	0.661 ± 0.111 (0.002)	0.958 ± 0.110 (0.001)
	215	0.903 ± 0.120 (0.041)	1.055 ± 0.105 (0.001)
	245	1.200 ± 0.135 (0.015)	0.927 ± 0.098 (0.001)
	275	1.164 ± 0.133 (0.006)	1.161 ± 0.111 (0.006)
	305	1.239 ± 0.138 (0.095)	1.049 ± 0.108 (0.000)
	335	0.865 ± 0.131 (0.139)	1.027 ± 0.116 (0.042)
$\phi - \Phi$	15	1.049 ± 0.128 (0.075)	1.219 ± 0.115 (0.013)
	45	1.141 ± 0.138 (0.015)	1.114 ± 0.114 (0.015)
	75	0.728 ± 0.104 (0.039)	0.705 ± 0.089 (0.011)
	105	0.659 ± 0.099 (0.027)	0.712 ± 0.088 (0.001)
	135	1.063 ± 0.131 (0.039)	0.974 ± 0.106 (0.013)
	165	1.354 ± 0.150 (0.007)	1.337 ± 0.123 (0.007)
	195	1.180 ± 0.141 (0.031)	1.260 ± 0.118 (0.005)
	215	1.189 ± 0.145 (0.094)	0.912 ± 0.104 (0.003)
	245	0.659 ± 0.116 (0.001)	0.675 ± 0.095 (0.009)
	275	0.652 ± 0.112 (0.121)	0.702 ± 0.093 (0.001)
	305	0.983 ± 0.137 (0.059)	0.985 ± 0.107 (0.007)
	335	1.342 ± 0.142 (0.023)	1.405 ± 0.121 (0.006)
$\phi + \Phi$	15	1.060 ± 0.130 (0.026)	1.191 ± 0.116 (0.003)
	45	1.072 ± 0.134 (0.044)	0.972 ± 0.103 (0.004)
	75	1.010 ± 0.132 (0.094)	0.980 ± 0.106 (0.010)
	105	0.694 ± 0.109 (0.015)	0.826 ± 0.099 (0.009)
	135	0.813 ± 0.114 (0.065)	1.127 ± 0.112 (0.014)
	165	0.996 ± 0.127 (0.125)	1.126 ± 0.110 (0.006)
	195	1.086 ± 0.129 (0.025)	1.091 ± 0.109 (0.014)
	215	1.023 ± 0.128 (0.005)	0.723 ± 0.090 (0.010)
	245	1.057 ± 0.131 (0.025)	1.036 ± 0.107 (0.005)
	275	0.937 ± 0.124 (0.009)	0.936 ± 0.102 (0.013)
	305	1.178 ± 0.139 (0.026)	1.019 ± 0.108 (0.006)
	335	1.074 ± 0.132 (0.092)	0.974 ± 0.104 (0.002)
Φ	15	0.818 ± 0.118 (0.047)	1.132 ± 0.115 (0.016)
	45	0.933 ± 0.134 (0.009)	1.073 ± 0.112 (0.005)
	75	1.003 ± 0.121 (0.000)	0.977 ± 0.101 (0.009)
	105	1.219 ± 0.131 (0.011)	0.892 ± 0.094 (0.008)
	135	1.043 ± 0.138 (0.002)	0.916 ± 0.103 (0.003)
	165	1.032 ± 0.131 (0.035)	0.978 ± 0.107 (0.013)
	195	0.794 ± 0.115 (0.085)	1.031 ± 0.110 (0.007)
	215	0.995 ± 0.132 (0.032)	0.827 ± 0.099 (0.008)
	245	1.062 ± 0.121 (0.004)	1.058 ± 0.103 (0.009)
	275	0.856 ± 0.113 (0.060)	0.883 ± 0.096 (0.010)
	305	1.196 ± 0.145 (0.011)	1.248 ± 0.119 (0.018)
	335	1.050 ± 0.135 (0.060)	0.985 ± 0.108 (0.004)

Bibliography

[1] T. H. Bauer, R. D. Spital, D. R. Yennie, and F. M. Pipkin, Rev. Mod. Phys. **50**, 261 (1978).

[2] J. J. Sakurai, Annals Phys. **11**, 1 (1960).

[3] T. Regge, Nuovo Cim. **14**, 951 (1959).

[4] J. B. D. Collins, Cambridge University Press (1977).

[5] A. Donnachie, H. G. Dosch, P. V. Landshoff, and O. Nachtmann, Cambridge University Press (2002).

[6] M. A. Pichowsky and T. S. H. Lee, Phys. Rev. **D56**, 1644 (1997), `nucl-th/9612049`.

[7] J. Ballam et al., Phys. Rev. **D7**, 3150 (1973).

[8] W. Struczinski et al. (Aachen-Hamburg-Heidelberg-Munich), Nucl. Phys. **B108**, 45 (1976).

[9] R. M. Egloff et al., Phys. Rev. Lett. **43**, 657 (1979).

[10] D. Aston et al., Nucl. Phys. **B209**, 56 (1982).

[11] W. D. Shambroom et al., Phys. Rev. **D26**, 1 (1982).

[12] M. Derrick et al. (ZEUS), Z. Phys. **C69**, 39 (1995), `hep-ex/9507011`.

[13] D. P. Barber et al., Zeit. Phys. **C12**, 1 (1982).

[14] M. Derrick et al. (ZEUS), Phys. Lett. **B377**, 259 (1996), `hep-ex/9601009`.

[15] M. Derrick et al. (ZEUS), Phys. Lett. **B380**, 220 (1996), `hep-ex/9604008`.

[16] T. Nakano and H. Toki (1997), given at 5th Tamura Symposium: International Workshop on Exciting Physics with New Accelerators Facilities (EXPAF 97), Aioi, Japan, 11-13 Mar 1997.

[17] A. I. Titov, T. S. H. Lee, H. Toki, and O. Streltsova, Phys. Rev. **C60**, 035205 (1999).

[18] A. I. Titov and T. S. H. Lee, Phys. Rev. **C67**, 065205 (2003), `nucl-th/0305002`.

[19] J. M. Laget, Phys. Lett. **B489**, 313 (2000), `hep-ph/0003213`.

[20] A. I. Titov, Y. Oh, and S. N. Yang, Phys. Rev. Lett. **79**, 1634 (1997), nucl-th/9702015.

[21] R. A. Williams, Phys. Rev. **C57**, 223 (1998).

[22] H. J. Besch et al., Nucl. Phys. **B70**, 257 (1974).

[23] K. Schilling, P. Seyboth, and G. E. Wolf, Nucl. Phys. **B15**, 397 (1970).

[24] H. J. Halpern et al., Phys. Rev. Lett. **29**, 1425 (1972).

[25] H. J. Behrend et al., Nucl. Phys. **B144**, 22 (1978).

[26] E. Anciant et al. (CLAS), Phys. Rev. Lett. **85**, 4682 (2000), hep-ex/0006022.

[27] J. Barth et al., Eur. Phys. J. **A17**, 269 (2003).

[28] K. McCormick et al. (CLAS) (2003), hep-ex/0311024.

[29] R. H. Milburn, Phys. Rev. Lett. **10**, 75 (1963).

[30] F. R. Arutyunian and V. A. Tumanian, Phys. Lett. **4**, 176 (1963).

[31] A. M. Sandorfi, J. LeVine, C. E. Thorn, G. Giordano, and G. Matone, IEEE Trans. Nucl. Sci. **30**, 3083 (1983).

[32] H. Ohgaki et al., IEEE Trans. Nucl. Sci. **38**, 386 (1991).

[33] J. P. Bocquet et al., Nucl. Phys. **A622**, 124c (1997).

[34] J. K. Ahn et al. (1999), prepared for 12th Symposium on Accelerator Science and Technology (SAST'99), Wako, Japan, 27-29 Oct 1999.

[35] T. Matsumura (LEPS), Master thesis of Yamagata University (in Japanease) (2000).

[36] http://www.spring 8.or.jp.

[37] T. Nakano et al., Nucl. Phys. **A684**, 71 (2001).

[38] T. Nakano et al. (LEPS), Phys. Rev. Lett. **91**, 012002 (2003), hep-ex/0301020.

[39] R. G. T. Zegers et al. (LEPS), Phys. Rev. Lett. **91**, 092001 (2003), nucl-ex/0302005.

[40] J. K. Ahn (LEPS), Nucl. Phys. **A721**, 715 (2003).

[41] T. Hotta (LEPS), Nucl. Phys. **A721**, 751 (2003).

[42] T. Ishikawa (LEPS), LEPS technical note **17** (2003).

[43] T. Matsumura (LEPS), Doctor thesis of Osaka university (2004).

[44] N. Muramatsu et al. (LEPS), LEPS technical note **14** (2002).

[45] K. Tsumaki, SPring-8 annual report p. 132 (1998).

[46] T. Mibe (LEPS), Master thesis (in Japanease) (2000).

[47] H. Kohri (LEPS), RCNP annual report (2001).

[48] V. Fild Ltd., *OPERA-3D TOSCA*, URL `http://www.vectorfields.co.uk`.

[49] M. Sumihama (LEPS), Doctor thesis of Osaka university (2003).

[50] Y. Sugaya et al., IEEE Trans. Nucl. Sci. **48**, 1282 (2001).

[51] N. Muramatsu et al. (LEPS), LEPS technical note **1** (2002).

[52] W. Chang et al. (LEPS), LEPS technical note **2** (2002).

[53] R. Brun et al., *GEANT 3.21* (1984).

[54] K. Hagiwara et al. (Particle Data Group), Phys. Rev. **D66**, 010001 (2002).

[55] K. Lukashin et al. (CLAS), Phys. Rev. **C63**, 065205 (2001), `hep-ex/0101030`.

[56] O. S. A. G. Frodesen and H. Tofte, *Probability and statistics in particle physics* (1979).

[57] A. Boyarski et al., Phys. Lett. **B34**, 547 (1971).

[58] D. P. Barber et al., Zeit. Phys. **C7**, 17 (1980).

[59] S. P. Barrow et al. (Clas), Phys. Rev. **C64**, 044601 (2001), `hep-ex/0105029`.

[60] A. I. Titov, private communications.

[61] A. Hosaka, private communications.

[62] S. J. Brodsky, E. Chudakov, P. Hoyer, and J. M. Laget, Phys. Lett. **B498**, 23 (2001), `hep-ph/0010343`.

[63] E. Martynov, E. Predazzi, and A. Prokudin, Eur. Phys. J. **C26**, 271 (2002), `hep-ph/0112242`.

[64] D. J. Tedeschi (CLAS), p. 367 (2001), in Proccedings of International Symposium, Electromagnetic interactions in nuclear and hadron physics, Osaka 2001 (Workd Scientific, 2002).

[65] C. Berger, N. Mistry, L. Roberts, R. Talman, and P. Walstrom, Phys. Lett. **B39**, 659 (1972).

[66] H. Kohri et al. (LEPS), LEPS technical note **15** (2003).